Spring 5-15-2015

Light Controlling at Subwavelength Scales in Nanophotonic Systems: Physics and Applications

Yuecheng Shen
Washington University in St. Louis

Washington University in St. Louis

School of Engineering and Applied Science

Department of Electrical and Systems Engineering

Dissertation Examination Committee:
Jung-Tsung Shen, Chair
ShiNung Ching
Eric Henriksen
Srikanth Singamaneni
Lihong Wang

Light Controlling at Subwavelength Scales in Nanophotonic Systems:

Physics and Applications

by

Yuecheng Shen

A dissertation presented to the Graduate School of Arts and Sciences
of Washington University in partial fulfillment of the
requirements for the degree of

Doctor of Philosophy

May 2015
Saint Louis, Missouri

Contents

List of Figures

List of Tables

Acknowledgments

First of all, I would like to thank my research advisor Dr. Jung-Tsung Shen. He is one of the smartest and most knowledgeable people I have ever seen in my life. During the past five years, his patience, encouragement, and guidance have been critically important for me. My sincere thanks would also go to all my previous and current lab mates for many profound suggestions, which benefits me a lot and helps me to proceed. I would also like to express my deepest thanks to my parents for their love and encouragement throughout my life. I would never have so many opportunities without them. Finally, I would like to fully express my gratitude to my wife Ting. Her love and devotion are truly inspirational.

Yuecheng Shen

Washington University in Saint Louis
May 2015

ABSTRACT OF THE DISSERTATION

Light Controlling at Subwavelength Scales in Nanophotonic Systems:

Physics and Applications

by

Yuecheng Shen

Doctor of Philosophy in Electrical Engineering

Washington University in St. Louis, May 2015

Professor Jung-Tsung Shen, Chair

The capability of controlling light at scales that are much smaller than the operating wavelength enables new optical functionalities, and opens up a wide range of applications. Such a capability is out of the realm of conventional optical approaches. This dissertation aims to explore the light-matter interactions at nanometer scale, and to investigate the novel scientific and industrial applications. In particular, we will explain how to detect nanoparticles using an ultra-sensitive nano-sensor; we will also describe a photonic diode which generates a unidirectional flow of single photons; Moreover, in an one-dimensional waveguide QED system where the fermionic degree of freedom is present, we will show that strong photon-photon interactions can be generated through scattering means, leading to photonic bunching and anti-bunching with various applications. Finally, we will introduce a mechanism to achieve super-resolution to discern fine features that are orders of magnitude smaller than the illuminating wavelength. These research projects incorporate recent advances in quantum nanophotonics, nanotechnologies, imaging reconstruction techniques, and rigorous numerical simulations.

Chapter 1

Introduction

There has been an increasingly interest in nano-photonic systems in recent decades, in which light is confined at subwavelength scale. This interest stems partly from the recent advent of the experimental capability and fabrication techniques. For example, by tapering a commercial optical fiber, people are able to generate subwavelength diameter optical fibers. Due to the extremely thin diameter, when light is propagating along this fiber a significant amount of light penetrates into the surround medium, enabling applications such as nano-sensors [1] and fiber couplers [2]. Moreover, those subwavelength diameter optical fibers are demonstrated with small loss less than 0.1 dB/mm from the visible to near-infrared spectral range, and are also very flexible to be twisted or bended into different shape for different functionalities [3]. Another kind of important components to confine light to nanometer scale is the quantum dot. The Quantum dots, being called "artificial atom", are nanocrystals typically made of semiconductor materials. They usually maintain very small sizes ranging from hundreds of nanometers to several nanometers, but can exhibit prominent quantum mechanical properties with broad applications in quantum computing [4] and in vivo imaging for live cells [5]. Subwavelenth periodic nanostructures also play important role in nanophotonic systems. By precisely designing their patterns, these artificially engineered materials can exhibit superior macroscopic optical properties that have not yet been found in nature. For example, materials with negative refractive index [6] and ultrahigh refractive index [7] can

be generated using Subwavelenth periodic nanostructures. Nowadays, people are capable of making those periodic nanostructures with various shapes using electron beam lithography. With these in mind, controlling light at subwavelength scales in nanophotonic systems has become a flourishing and active research field, which potentially enables new optical phenomenon with superior performances and new functionalities in photonic devices.

In Chapter 2, we consider an interesting nanophotnic system, which consists of a whispering-gallery-mode (WGM) resonator side-coupled to a tapered single-moded optical fiber. This WGM resonator is known to support a pair of degenerate clockwise (CW) and counter-clockwise (CCW) propagating modes [8]. When a nanoparticle is adsorbed onto the surface of the resonator, it strongly interacts with CW and CCW propagating modes in the resonator. Such an interaction breaks the mode degeneracy in the resonator and causes mode splitting. The two main advantages in this sensing mechanism are: (i) the quality factor of the WGM resonator can be extremely high 10^8, which significantly intensifies the field strength and leads to strong light-matter interactions; (ii) the mode splitting in the transmission spectrum are distinct to be measured. Thus, the system exhibits very high sensitivity that is able to detect label-free single nanoparticles with sizes down to tens of nanometers. In particular, we perform a complete and coherent description for the sensing mechanisms for two most common and important types of nanoparticles, i.e., plasmonic particles and Rayleigh scatterers, and provide criteria for extracting information from the measurable transmission spectra [9]. Rigorous numerical simulations are also performed to verify the analytic results [10]. We also consider the accurate determination of the number particles in large particle flux in a statistical manner [11].

Another application in nanophotonic system is designing a single-photon optical diode [12], which is described in Chapter 3. Such an optical diode is accomplished by coupling a quantum dot to a single-polarization single-mode (SPSM) waveguide, and it can achieve

optical isolation down to single-photon levels. The time reversal symmetry in this setup is broken due to the existence of a local external magnetic field.

Strong photon-photon interactions can also be generated in nanophotonic systems. In Chapter 4, we investigate the problem of arbitrary photonic Fock states scattering in a nanophotonic system which consists of an one-dimensional waveguide coupled to a two-level atom [13]. The fermioinc degree of freedom of the two-level atom induces effective photon-photon interactions. Therefore, after scattering, the originally uncorrelated photons become strongly correlated. By computing their correlation functions, it can be shown that the transmitted photons are always bunched together while the reflected photons are always anti-bunched, leading to various possible applications in quantum information processing.

In Chapter 5, we attack one of the most important problems in optics, which is to achieve deep subwavelengh resolution in optical imaging. Specially, we design a nano-torches lens (CNT-lens)to achieve 40 nm lateral resolution [14]. The key enabling feature is to create an array of correlated nano-torches in the subwavlength scale. By properly designing the parameters of those correlated nanotorches, the CNT-lens can focus light to a deep subwavelength spot with significantly enhanced intensity, which overcomes the low transmissivity of optical signals in other near field imaging approaches. Photonic nanojet is another approach to focus light to a subwavelength spot. It has been demonstrated as a highly focused optical beam with a subwavelength waist on the shadow side of the sphere [15]. For all possible applications, it is desired that the nanojets extend as far as possible in the forward direction to push the operating range away from the near field range. In Chapter 6, we show that a simple two-layer microsphere can generate ultralong nanojet with extensions of 22 wavelength [16], by using conventionally available optical materials. This capability will greatly facilitate successful applications of nanojets.

Chapter 2

Nanoparticle Sensing

2.1 Introduction

In this Chapter, we start by describing a nanoparticle sensing mechanism in nanophotonic systems. Nanoparticle sensing and monitoring have become increasingly important in many fields. For example, atmospheric nanoparticles have crucial effects on climate change [17] and human health [18]. Nanoparticles also appear as pathogens in bioterrorism [19] and as contaminants in manufacturing processes. In nanomedicine, metallic nanoparticles have also been used as cancer-fighting agent [20]. Thus, in many practical situations, especially in the low-particle-flux or low-particle concentration regimes, it is desired to have a sensing mechanism that can detect label-free single nanoparticles. Nonetheless, the scattering cross section of a nanoparticle, which describes the likelihood of light or other radiation being scattered by a particle, is extremely small under the illumination of visible light. According to the Rayleigh theory, the scattering cross section for a nanoparticle approaches to zero, with an asymptotic behaviors proportional to the fourth power of the diameter over wavelength. Owing to the extremely small scattering cross section, nanoparticles are in general very difficult to be detected using optical methods. To bypass this fundamental difficulty and increase the detection limit, instead of measuring the scattering cross section directly,

one possibility is to exploit the phase coherence between the probing- and scattered-light signals by coupling nanoparticles to optical waveguides and resonators [21]. Very recently, the system consisting of high quality-factor whispering-gallery-mode (WGM) resonators and tapered fibers has been proposed theoretically [22, 23, 24] and demonstrated experimentally to achieve single-particle resolution [22, 25, 26]. Despite these accomplishments, critical questions remain in such a detecting scheme, such as the determination from the transmission spectrum of the number of the particles adsorbed and their angular positions. In the following, we will investigate the theoretical aspects of nanoparticle sensing using WGM resonators and address these issues.

2.2 Schematics of the System and Underlying Physics

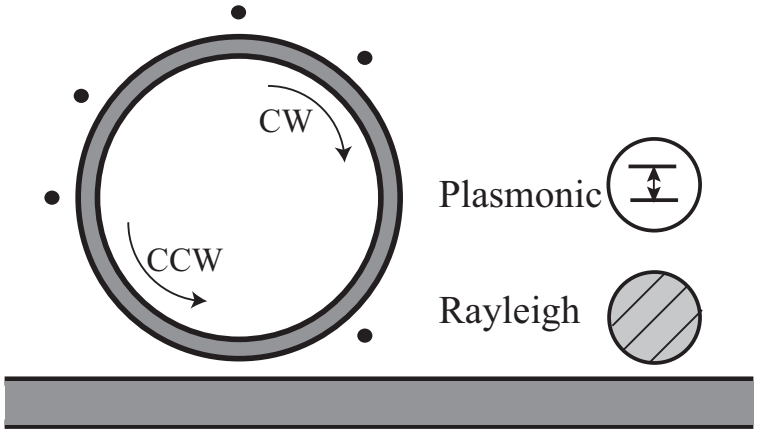

Figure 2.1: Schematic representation of the detecting system. The system consists of a WGM resonator side-coupled to a tapered single-moded optical fiber. The black dots denote nanoparticles which can be either plasmonic or Rayleigh-type, as shown on the right.

The system of interest is depicted schematically in Fig. 2.1, which consists of a WGM resonator side-coupled to a tapered single-moded optical fiber. The nanoparticles are adsorbed onto the surface of the resonator and sensed by an evanescent field coupling due to the guided WGM in the resonator. Based upon the nature of the scattering, two types of nanoparticles are of particular interest: (i) a plasmonic particle, such as a metallic particle or an

on-resonant molecule that has a sharp resonance peak in the frequency range of interest; and (ii) a Rayleigh-type particle, such as a polystyrene particle or an off-resonant molecule, that does not have a distinct resonance peak in the frequency range of interest. In a typical experimental setup, a weak coherent laser beam is coupled into the fiber; after propagating around the WGM resonator and interacting with the adsorbed particles, the transmitted signal in the fiber is measured. The transmission spectrum contains the information of photon-nanoparticle interactions which characterizes the scattering nature of the particles. Here, we start by explaining the physics of this system. An ideal WGM resonator supports a pair of degenerate counter-clockwise (CCW) and clockwise (CW) propagating modes [27]. An adsorbed nanoparticle on the surface backscatters CCW mode into CW mode, and vice versa. Thus, the nanoparticle effectively acts as a localized surface imperfection that breaks the mode degeneracy and induces mode splitting [28]. For a single Rayleigh particle, the mode splitting gives rise to two dips in the transmission spectrum; while for a single plasmonic particle, the mode splitting results in three dips in the spectrum, due to the additional resonance [21]. When more than one particle is adsorbed, multiple scatterings between particles occur. These coherent inter-particle scattering processes depend on the relative angular positions of the particles, and give rise to an interference term in the transmission amplitude that modifies the spectral separation between the transmission dips.

2.3 The Model and Theoretical Description

With this physical understanding, we now discuss in more details of each case. For brevity, unless noted otherwise, all particles are assumed to be identical; the formalism can be straightforwardly generalized to the case for non-identical particles.

2.3.1 Plasmonic Particle

For plasmonic particles, the Hamiltonian is given by:

$$\begin{aligned} H/\hbar = & \int dx c_R^\dagger(x) \left(\omega_0 - i v_g \frac{\partial}{\partial x}\right) c_R(x) + \int dx c_L^\dagger(x) \left(\omega_0 + i v_g \frac{\partial}{\partial x}\right) c_L(x) \\ & + \left(\omega_c - i\frac{1}{\tau_c}\right) a^\dagger a + \left(\omega_c - i\frac{1}{\tau_c}\right) b^\dagger b + \sum_j \left[\left(\Omega_e - i\frac{1}{\tau_q}\right) a_{ej}^\dagger a_{ej} + \Omega_g a_{gj}^\dagger a_{gj}\right] \\ & + \int dx\, \delta(x) \left[V_a c_R^\dagger(x) a + V_a^* a^\dagger c_R(x)\right] + \int dx\, \delta(x) \left[V_b c_L^\dagger(x) b + V_b^* b^\dagger c_L(x)\right] \\ & + \left(h b^\dagger a + h^* a^\dagger b\right) + \sum_j \left[(g_{bj} b \sigma_{+j} + g_{bj}^* b^\dagger \sigma_{-j}) + (g_{aj} a \sigma_{+j} + g_{aj}^* a^\dagger \sigma_{-j})\right]. \end{aligned} \tag{2.1}$$

$c_{R/L}^\dagger(x)$ is a bosonic operator creating a right (R) or left (L) moving photon at position x along the fiber. ω_0 is the reference frequency where the waveguide dispersion relation is linearized and v_g is the group velocity [29]. $a^\dagger$ and $b^\dagger$ denote the creation operator for the CCW and CW modes of the WGM resonator, respectively; ω_c is the resonant frequency of the WGM resonator. $1/\tau_c$ is the intrinsic dissipation rate of each WGM, and $1/\tau_q$ is the intrinsic dissipation rate of each particle. $\hbar\Omega_e$ is the excitation energy of the particle, while $\hbar\Omega_g$ is the ground state energy. $\Omega \equiv \Omega_e - \Omega_g$ is the resonant frequency of the plasmonic particle. h is the intermode scattering strength between CCW and CW modes due to the surface imperfection. σ_{+j} and σ_{-j} are the excitation and deexcitation operator of the j-th nanoparticle, respectively. $V_{a/b}$ is the waveguide-resonator coupling strength. g_{aj} and g_{bj} denote the resonator-particle coupling strength between the j-th particle and CCW, or CW mode, respectively.

The experiments are typically carried out such that the mean photon number in the system is much smaller than one [30]. The scattering events thus are dominantly one-photon processes.

The general form of a 1-photon and n-particle quantum state is:

$$|\Phi(t)\rangle = \left\{ \int dx \left[\phi_R(x,t) c_R^\dagger(x) + \phi_L(x,t) c_L^\dagger(x) \right] + e_a(t) a^\dagger + e_b(t) b^\dagger + \sum_{j=1}^{n} e_{qj}(t) \sigma_{+j} \right\} |G\rangle, \tag{2.2}$$

where $\phi_R(x,t)$, $\phi_L(x,t)$ are the photonic wave functions in the waveguide; $e_a(t)$ and $e_b(t)$ are the excitation amplitudes of a and b WGM, respectively; $e_{qj}(t)$ is the excitation amplitude of the j-th particle. $|G\rangle = |0;0,0;-,-,...,-\rangle$ denotes the vacuum state (zero photon in the fiber and WGM resonator, and all the plasmonic particles are in the ground state $|-\rangle$). By applying the time-dependent Schrödinger equation $i\hbar\partial/\partial t|\Phi(t)\rangle = H|\Phi(t)\rangle$, one obtains the following set of equations of motion:

$$-iv_g \frac{\partial}{\partial x}\phi_R(x,t) + \delta(x) V_a e_a(t) + (\omega_0 + n\Omega_g)\phi_R(x,t) = i\frac{\partial}{\partial t}\phi_R(x,t), \tag{2.3a}$$

$$+iv_g \frac{\partial}{\partial x}\phi_L(x,t) + \delta(x) V_b e_b(t) + (\omega_0 + n\Omega_g)\phi_L(x,t) = i\frac{\partial}{\partial t}\phi_L(x,t), \tag{2.3b}$$

$$\left(\omega_c + n\Omega_g - i\frac{1}{\tau_c}\right) e_a(t) + V_a^* \phi_R(0,t) + \sum_j g_{aj}^* e_{qj}(t) + h^* e_b(t) = i\frac{\partial}{\partial t} e_a(t), \tag{2.3c}$$

$$\left(\omega_c + n\Omega_g - i\frac{1}{\tau_c}\right) e_b(t) + V_b^* \phi_L(0,t) + \sum_j g_{bj}^* e_{qj}(t) + h e_a(t) = i\frac{\partial}{\partial t} e_b(t), \tag{2.3d}$$

$$\left((n-1)\Omega_g + \Omega_e - i\frac{1}{\tau_q}\right) e_{qj}(t) + g_{aj} e_a(t) + g_{bj} e_b(t) = i\frac{\partial}{\partial t} e_{qj}(t). \tag{2.3e}$$

For a given initial state, the full spatiotemporal dynamics of the system can be obtained by numerically solving the above set of equations. Here, we derive the steady state solution to find the energy eigenstates of the system. For a steady state, one has $|\Phi(t)\rangle = e^{-i\epsilon t}|\epsilon^+\rangle$, where $\epsilon = \omega + n\Omega_g$ is the initial energy of the system divided by $\hbar$ and $\omega = \omega_0 + v_g k$ is the frequency of the incoming photon (k is the wave vector of the photon). Thus, $\phi(x,t) = \phi(x)e^{-i\epsilon t}$, and simliar expressions for other terms. To compute the transport properities of the photon, one takes $\phi_R(x) = e^{ikx}[\theta(-x) + t\theta(x)]$, and $\phi_L(x) = re^{-ikx}\theta(-x)$, where t and r are transmission and reflection amplitude, respectively. The set of equations, Eqs. (2.3), can

be solved straightforwardly [29] and yield the solution for the transmission amplitude $t(\omega)$:

$$t = \frac{\Delta\tilde{\omega}_c\left(\Delta\tilde{\omega}_c\Delta\tilde{\omega}_q - G_+^2\right) + \Delta\tilde{\omega}_q\Gamma^2 - I_1 - |h|^2\Delta\tilde{\omega}_q + iG_-^2\Gamma + I_2/\Delta\tilde{\omega}_q}{(\Delta\tilde{\omega}_c + i\Gamma)\left[\Delta\tilde{\omega}_q\left(\Delta\tilde{\omega}_c + i\Gamma\right) - G_+^2\right] - I_1 - |h|^2\Delta\tilde{\omega}_q + I_2/\Delta\tilde{\omega}_q}, \tag{2.4}$$

where $\Delta\tilde{\omega}_c = \omega - \omega_c + i(1/\tau_c)$, $\Delta\tilde{\omega}_q = \omega - \Omega_c + i(1/\tau_q)$, $G_+^2 = \sum_j(|g_{aj}|^2 + |g_{bj}|^2) = 2ng^2$, $G_-^2 = \sum_j(|g_{aj}|^2 - |g_{bj}|^2) = 0$, $\Gamma = V^2/2v_g$ is the coupling strength between the resonator and fiber, and

$$I_1 = \sum_j(g_{aj}^* g_{bj} h + g_{aj} g_{bj}^* h^*) = 2g^2|h|\sum_j \cos(2m\theta_j - \theta_h), \tag{2.5a}$$

$$I_2 = \sum_{j,k}\left[|g_{aj}|^2|g_{bk}|^2 - (g_{aj}^* g_{bj})(g_{ak} g_{bk}^*)\right] = 2g^4\left(\frac{n(n-1)}{2} - \sum_{j<k}\cos 2m(\theta_j - \theta_k)\right). \tag{2.5b}$$

In the equalities above, $g_{aj} = g_a e^{im\theta_j}$ and $g_{bj} = g_b e^{-im\theta_j}$ are employed with m being the order of the WGM; also, $g_a = g_b \equiv g$ is used for induced dipole moment. θ_j is the angular position of the j-th particle. The $\theta = 0$ axis is chosen to point perpendicular to the fiber direction and bisects the resonator so that $V_a = V_b \equiv V$ can be taken as real numbers [29]. The interference term I_2 involves the relative angular positions and is due to multiple scattering between particles.

2.3.2 Rayleigh Scatterer

For a Rayleigh scatterer, the interaction between the particle and the photon is given by $H_I = -\vec{d}\cdot\vec{E}$, where $\vec{d} = \alpha\vec{E}$ is the induced dipole moment of the particle, and the polarizability $\bar{\alpha} = 4\pi\epsilon_0 a^3(\epsilon_{\text{particle}} - \epsilon_{\text{medium}})/(\epsilon_{\text{particle}} + 2\epsilon_{\text{medium}}) \equiv \bar{\alpha}_1 + i\bar{\alpha}_2$. $\epsilon_{\text{particle}}$ is the complex effective permittivity for the spherical particle and ϵ_{medium} is the permittivity for its surrounding environment. The electrical field profile of the WGM is expanded as $\vec{E} = (a + b^\dagger)\vec{\phi}_m + (a^\dagger + b)\vec{\phi}_m^*$ [29], where $\vec{\phi}_m = \vec{E}_0 e^{im\theta}$ is the m-th order WGM, $\vec{E}_0$ is the radial part of the electrical field. $E_0 = |\vec{E}_0|$ denotes the magnitude of the field. Using these expressions, H_I

now becomes

$$H_I = -2n\bar{\alpha}E_0^2(a^\dagger a + b^\dagger b) - 2\left(\sum_j e^{2im\theta_j}\bar{\alpha}E_0^2\right)b^\dagger a - 2\left(\sum_k e^{-2im\theta_k}\bar{\alpha}E_0^2\right)a^\dagger b, \tag{2.6}$$

where the last two terms indicate that all the particles collectively backscatter the WGMs into each other, effectively acting as an inter-mode coupling. Thus, the Hamiltonian for the Rayleigh case can be written as:

$$\begin{aligned} H/\hbar = &\int dx c_R^\dagger(x)\left(\omega_0 - iv_g\frac{\partial}{\partial x}\right)c_R(x) + \int dx c_L^\dagger(x)\left(\omega_0 + iv_g\frac{\partial}{\partial x}\right)c_L(x) \\ &+ (\Omega_c - i\gamma)\,a^\dagger a + (\Omega_c - i\gamma)\,b^\dagger b \\ &+ \int dx\,\delta(x)\left[V_a c_R^\dagger(x)a + V_a^* a^\dagger c_R(x)\right] + \int dx\,\delta(x)\left[V_b c_L^\dagger(x)b + V_b^* b^\dagger c_L(x)\right] \\ &+ \left(h - 2\alpha E_0^2\sum_j e^{2im\theta_j}\right)b^\dagger a + \left(h^* - 2\alpha E_0^2\sum_k e^{-2im\theta_k}\right)a^\dagger b, \end{aligned} \tag{2.7}$$

where $\Omega_c = \omega_c - 2n\alpha_1 E_0^2$ and $\gamma = \frac{1}{\tau_c} + 2n\alpha_2 E_0^2$ (here $\alpha \equiv \bar{\alpha}/\hbar$). In contrast to the plasmonic case, the notable feature here is that both the WGM resonator frequency ω_c and damping rate $1/\tau_c$ are renormalized. Specifically, both terms are shifted by an amount proportional to the number of the particles n. The renormalization predicts a red-shift of the resonance frequency when the dielectric function of the particle is larger than that of the ambient surrounding medium ($\mathrm{Re}[\epsilon_{\mathrm{particle}}] > \mathrm{Re}[\epsilon_{\mathrm{medium}}]$, i.e., $\alpha_1 > 0$), and a blue-shift when the dielectric function of the particle becomes smaller ($\mathrm{Re}[\epsilon_{\mathrm{particle}}] < \mathrm{Re}[\epsilon_{\mathrm{medium}}]$, i.e., $\alpha_1 < 0$). The latter case describes the situation wherein the nanoparticles are embedded in an aqueous solution with a higher refractive index. Moreover, for dissipative materials, α_2 is positive and thus the damping rate increases, in accord with physical intuition. On the other hand, when there is a gain in the particle (e.g., due to external pumping and the nonlinearity in the particle), $\alpha_2 \leq 0$, the damping rate can be decreased. The transmission amplitude can

be computed straightforwardly to yield

$$t(\omega) = \frac{(\omega - \Omega_c + i\gamma)^2 - (h - 2\alpha E_0^2 \sum_j e^{2im\theta_j})(h^* - 2\alpha E_0^2 \sum_k e^{-2im\theta_k}) + \Gamma^2}{(\omega - \Omega_c + i\gamma + i\Gamma)^2 - (h - 2\alpha E_0^2 \sum_j e^{2im\theta_j})(h^* - 2\alpha E_0^2 \sum_k e^{-2im\theta_k})}. \tag{2.8}$$

The term in the amplitude that is proportional to $\sum_{j,k} e^{2im(\theta_j - \theta_k)}$ is the interference term.

The two amplitudes, Eq. (2.4) and Eq. (2.8) contain all of the information but, in general, are very complicated. With the advent of micro-fabrication techniques, resonators can be fabricated with an extremely high quality-factor. Thus, in the following, we will take the intermode scattering strength h to be 0, which simplifies the expression.

2.4 Analytic Results

2.4.1 Transmission Spectra

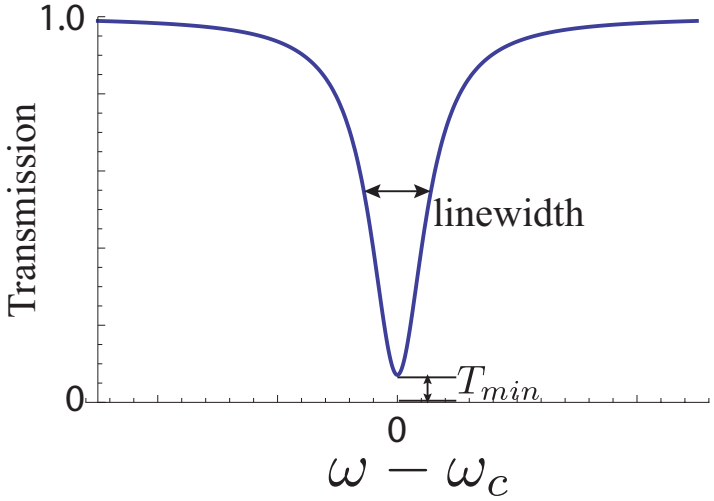

Figure 2.2: Schematic representation of the transmission spectrum for the null case (i.e., no particle is adsorbed). $T_{min} = (1/\tau_c - \Gamma)^2/(1/\tau_c + \Gamma)^2$. The full linewidth at half minimum is $2(1/\tau_c + \Gamma)$.

We now investigate the evolution of the transmission spectra $T(\omega) = |t(\omega)|^2$ as the number of the adsorbed particles increases. To begin with, Fig. 2.2 plots a typical transmission

spectrum for the null case, i.e., the bare system of the resonator and fiber with no particles adsorbed. For this case, $t = (\omega - \omega_c + i/\tau_c - i\Gamma)/(\omega - \omega_c + i/\tau_c + i\Gamma)$, and the relevant parameters of the setup $1/\tau_c$, Γ, and ω_c can be extracted from a simple fitting scheme (e.g. the method of least squares).

Next, we plot the transmission spectra when successive single particles are progressively adsorbed. The paramters to plot the transmission spectra are chosen as follows: for Rayleigh scatterers, $1/\tau_c = 0.76$ MHz, $\Gamma = 0.44$ MHz, $\alpha_1 E_0^2 = 6$ MHz, $\alpha_2 E_0^2 = 0.16$ MHz; for plasmonic particles, $1/\tau_c = 0.76$ GHz, $\Gamma = 0.44$ GHz, $g = 6$ GHz, $1/\tau_q = 0.16$ GHz [31]. We note here that the quantitative behaviors of the transmission spectra remains the same for a wide range of parameters.

For the Rayleigh case (left panel of Fig. 2.3), one of the notable features is that all spectra exhibit only two dips, as the presence of the particles breaks the degeneracy of the two WGMs by acting as a surface imperfection. We also note that the spectrum is asymmetric with respect to ω_c when α_2 is nonzero, and both dips have different linewidths and heights: when α_2 is not zero, such that α is complex, the effective intermode scattering strength in $b^\dagger a$ and $a^\dagger b$ in Eq. (2.7) are not complex conjugate to each other, which results in the asymmetry of the two dips. Moreover, it can be shown that the spectral separation of the two dips is always $\mathrm{Re}[2\sqrt{I_3}]$, where $I_3 = 4\alpha^2 E_0^4 \left(n + 2\sum_{j<k} \cos 2m(\theta_j - \theta_k)\right)$ is the interference term; the shift of the center of the spectrum (defined as the average of the location of the two dips) from ω_c is given by $-2n\alpha_1 E_0^2$, which is a direct result of the renormalization of the center frequency. By measuring the shift in one particle-case, $\alpha_1 E_0^2$ can be determined. Consequently, the number of the particle adsorbed for any cases can be determined by measuring the corresponding spectral shift and divided by $2\alpha_1 E_0^2$.

For identical plasmonic particles (right panel of Fig. 2.3), the spectrum is always symmetric with respect to the WGM resonance frequency ω_c, when the particles are on resonance ($\Omega = \omega_c$). For a fixed number of particles, the number of the dips depends on the value of

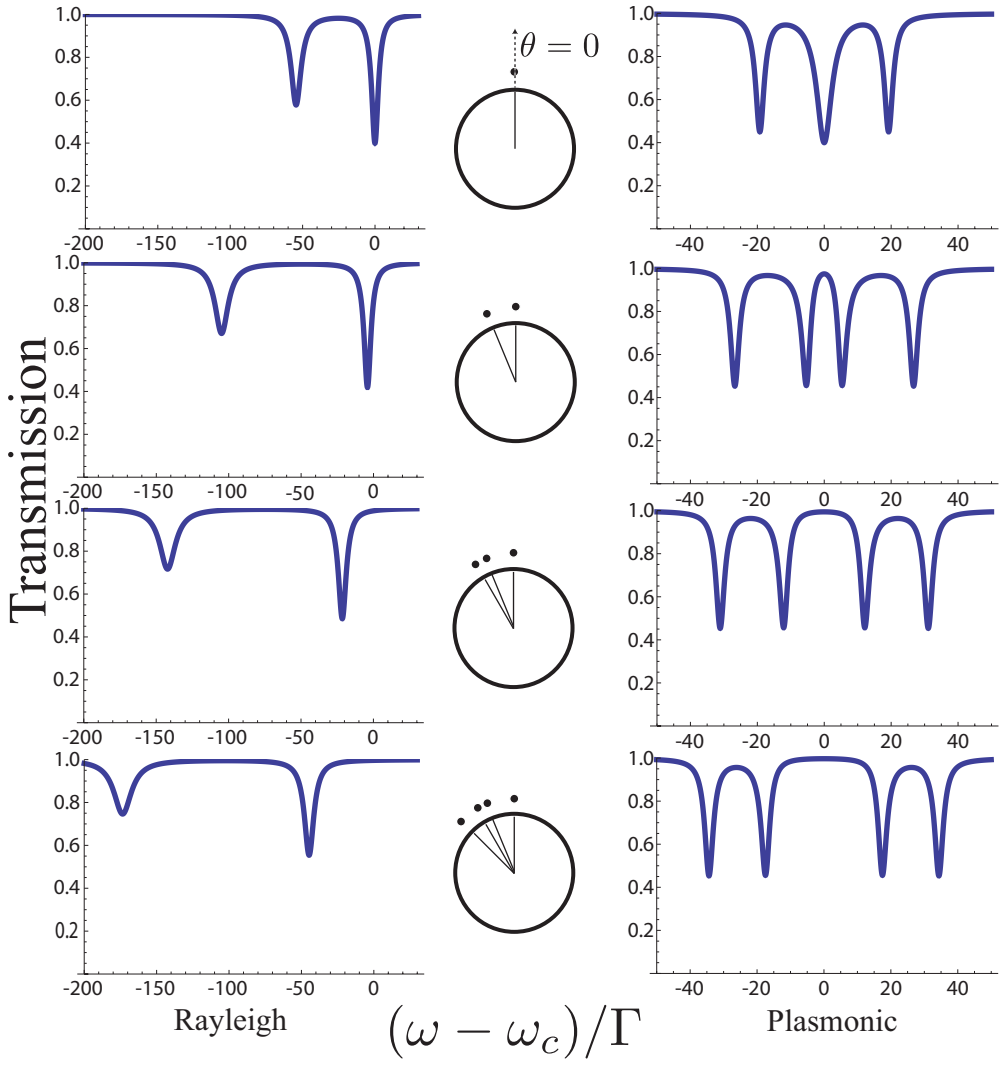

Figure 2.3: Transmission spectra for different number of adsorbed nanoparticles. Left: Rayleigh; Right: plasmonic. The angular positions of the particles are $\theta = 0$, $\pi/8$, $\pi/6$, $\pi/4$. $m = 17$ and $h = 0$ for both cases. For Rayleigh scatterers, $1/\tau_c = 0.76$ MHz, $\Gamma = 0.44$ MHz, $\alpha_1 E_0^2 = 6$ MHz, $\alpha_2 E_0^2 = 0.16$ MHz. For plasmonic particles, $1/\tau_c = 0.76$ GHz, $\Gamma = 0.44$ GHz, $g = 6$ GHz, $1/\tau_q = 0.16$ GHz. All parameters are given in angular frequency.

the interference term I_2. Specifically, when all cosine terms $\cos 2m(\theta_j - \theta_k)$ for $j < k$ become 1, I_2 reaches its minimum 0, the spectrum has three dips for any number of particles. Also, for the special case of two particles, when $\cos 2m(\theta_1 - \theta_2) = -1$ (which is only possible for the two-particle case), the spectrum has only two dips. Normally, $0 < I_2$, and the spectrum has four dips for any number (≥ 2) of particles, as shown in the right panel of Fig. 2.3. Here, we summarize the evolution of the structure of the dips: usually there are four dips; as each cosine term approaches 1, the two middle dips merge; and as each cosine term approaches -1, the two dips on each side of $\omega = \omega_c$ merge giving the spectrum two dips. In contrast to the Rayleigh-type case, the number of the particles adsorbed, however, cannot directly be determined by measuring the spectral shift and requires a numerical fitting from the transmission spectrum. Also, from the one particle case, τ_q, g_a, and g_b can be extracted. Consequently, further information such as the relative angular positions and the number of particles can be obtained by numerically fitting with Eq. (2.4) for any number of particles.

2.4.2 Matrix Reprsentation

The exact locations and number of the dips in the transmission spectrum are of particular interest, as they exhibit eigen-frequencies of the subsystem consisting of the resonator and the particles. Here, we describe a direct yet simple matrix method to derive these eigen-frequencies: The matrix essentially represents the Hamiltonian of the subsystem, with the diagonal terms being the unperturbed frequencies of the WGMs and nanoparticles, while the non-diagonal terms describing the couplings between the components. The eigenvalues of this matrix thus indicate the number and positions of dips in the transmission spectrum.

As a concrete example, we describe the case of Rayleigh scatterer adsorbed to the resonator. There are only two bases: CCW and CW, so the matrix takes the following form:

$$\begin{pmatrix} \omega_c - 2n\alpha E_0^2 & -2\alpha E_0^2 \sum_j e^{2im\theta_j} \\ -2\alpha E_0^2 \sum_k e^{-2im\theta_k} & \omega_c - 2n\alpha E_0^2 \end{pmatrix} \tag{2.9}$$

The two eigenvalues of the matrix are $\omega = \omega_c - 2n\alpha E_0^2 \pm 2\alpha E_0^2 \sqrt{\sum_{j,k} e^{2im(\theta_j - \theta_k)}}$. The real part of the eigenvalues gives exact locations of the two transmission dips. Moreover, the spectral separation of two dips is given by $\mathrm{Re}[2\sqrt{I_3}]$, which is the same as using the full Hamiltonian.

As a second example, we describe the case of two identical plasmonic particles adsorbed. The bases for the matrix are chosen as CCW ($|1,0;-,-\rangle$), CW ($|0,1;-,-\rangle$), $|0,0;+,-\rangle$ and $|0,0;-,+\rangle$, respectively. Using these bases, the matrix is given by:

$$\begin{pmatrix} \omega_c & 0 & g_a e^{im\theta_1} & g_a e^{im\theta_2} \\ 0 & \omega_c & g_b e^{-im\theta_1} & g_b e^{-im\theta_2} \\ g_a^* e^{-im\theta_1} & g_b^* e^{im\theta_1} & \omega_c & 0 \\ g_a^* e^{-im\theta_2} & g_b^* e^{im\theta_2} & 0 & \omega_c \end{pmatrix} \tag{2.10}$$

Here, $\theta = \theta_1 - \theta_2$ is the relative angular position of the two particles. For brevity, we assume that all the particles are on resonance with WGMs. The four eigenvalues of the matrix in Eq. (2.10) are $\omega = \omega_c \pm 2g|\cos m\theta/2|$, $\omega_c \pm 2g|\sin m\theta/2|$ ($g \equiv |g_a| = |g_b|$). Fig. 2.4 plots the four eigenvalues as a function of $m\theta$. From the plot, it is clear that when $m\theta = 0$, $\pi/4$, and $\pi/2$, there are 3, 4 and 2 nondegenerate eigenvalues, respectively. The numerical values and the number of nondegenerate eigenvalues are in complete agreement with the transmission spectrum. In particular, when $m\theta = \pi/8$, which corresponds to the two-particle case in Fig. 2.3, the eigenvalues give the exact the locations of the dips (note the frequency in Fig. 2.3 is normalized by Γ).

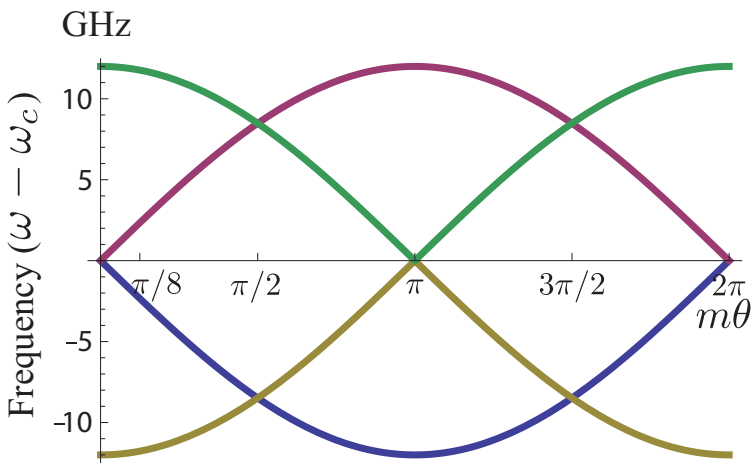

Figure 2.4: Eigenvalues as a function of $m\theta$ (m is the order of WGM) for the two-plasmonic particle case. $g = 6$ GHz.

The matrix method also provides a simple explanation that the transmission spectrum for the plasmonic case has at most four dips, when n (≥ 2) identical particles are adsorbed. When n identical plasmonic particles are adsorbed onto the WGM resonator, the dimension of the Hamiltonian matrix is $n + 2$, and is given by:

$$\begin{pmatrix} \omega_c & 0 & g_a e^{im\theta_1} & \cdots & g_a e^{im\theta_n} \\ 0 & \omega_c & g_b e^{im\theta_1} & \cdots & g_b e^{im\theta_n} \\ g_a^* e^{-im\theta_1} & g_b^* e^{-im\theta_1} & \Omega & 0 & 0 \\ \vdots & \vdots & 0 & \ddots & 0 \\ g_a^* e^{-im\theta_n} & g_b^* e^{-im\theta_n} & 0 & 0 & \Omega \end{pmatrix}, \tag{2.11}$$

where Ω is the excitation frequency of the particles. A direct computation reveals that there are $n-2$ degenerate eigenstates with eigenvalue Ω; moreover, these eigenstates do not involve the CCW and CW states but are only linear superposition of the particle states. Thus, these eigenstates are decoupled from the resonator and cannot be probed by the probing beam in the fiber; consequently, the transmission at the dark state resonant frequency Ω is always 100%, regardless of the particle dissipations. These states are properly named as the "dark states". Evidently, the maximum number of dips in the transmission spectrum

is $(n+2)-(n-2)=4$. For the case of four identical particles ($n=4$), which could be dissipative, the two dark states are given by $(0,0,\sin(\theta_2-\theta_3),\sin(\theta_3-\theta_1),\sin(\theta_1-\theta_2),0)$ and $(0,0,\sin(\theta_2-\theta_4),\sin(\theta_4-\theta_1),0,\sin(\theta_1-\theta_2))$, respectively. Thus the dark states are robust against the dissipations. These results can be generalized to the case when there are several species of plasmonic particles with different excitation frequencies. For example, when M species of particles are adsorbed, with excitation frequency Ω_i, and number n_i $(i=1,\cdots,M)$, the number of dark states is given by $D\equiv\sum_{i=1}^{M}d(n_i)$, where $d(n_i)=n_i-2$ if $n_i\geq 2$, and 0 if $n_i<2$. Consequently, the maximum number of transmission dips is $(2+\sum_{i=1}^{M}n_i)-D$. Although the simple matrix method gives directly the number and positions of the transmission dips, these sharp eigenfrequencies however are broadened by the intrinsic dissipation of the particles, as well as by the resonator-fiber coupling Γ. To obtain the linewidth of each transmission dip, as well as the numerical value of the transmission, one must employ the full theory presented above. It can be further shown that the dissipations and Γ do not affect the locations of the dips. We note that the matrix method could also deal with the case of higher power of the probing light, by employing bases with multiple plasmonic excitations. The dimension of the Hamiltonian matrix is accordingly enlarged, which gives rise to a more complicated transmission spectrum.

Here we describe possible schemes to reveal the signatures of the dark states. As the dark states are eigenstates formed by identical and independent plasmonic scatterers, the dark states can be transmuted into detectable bright states by alleviating either of these two requirements. For example, by imposing a spatially varying magnetic field, each plasmonic particle would experience different amount of transition frequency shift so as the particles become non-identical; additional transmission dips will thus emerge in the transmission spectrum, which provides the information about the number of particles. Alternatively, when two plasmonic particles are in close proximity to each other so a direct scattering of photons between the particles becomes possible, additional transmission dips will also emerge in the transmission spectrum. Mathematically, both approaches modify the lower-right diagonal

block of the Hamiltonian matrix of Eq. (5.2) so that in the former case, the identical Ω's are shifted to different values; while in the latter case, off-diagonal terms become non-zero due to the direct coupling. In both cases, all eigenstates couple to the WGMs and can be detected by the probing light.

2.5 Numerical Simulations

In this Section, we perform a rigorous numerical investigation to confirm the theoretical predictions for the Rayleigh scatterers. The primary predictions from Eq. (2.8) are: (i) The central spectral shift $S(N) \equiv |\Omega_c - \omega_c|$ is exactly proportional to the number of particles adsorbed, regardless of the imaginary part of the complex polarizability α. For positive (negative) α_1, the spectrum is red(blue)-shifted. (ii) The characteristics (e.g., width, location, and spectral separation) of the two transmission dips crucially depend on the parameters of the system, such as the angular positions and the dissipations of the particles; Ω_c however remains to be the center of the two transmission dips, and can be determined by the average location of the two dips.

2.5.1 Computation Geometry

We simulate the system in two dimensions using a full-vectorial finite element solver [32]. The computational geometry consists of a WGM resonator placed in the $x - y$ plane, with an inner and an outer radius of 14.0 μm and 15.0 μm, respectively. The resonator is coupled to a 1.0 μm-wide tapered fiber, with an edge to edge distance of 1.3 μm. Both the resonator and the fiber are made of silica with a refractive index 1.45. The background is vacuum or air (refractive index = 1). The nanoparticles are polystyrene particles with a radius $a = 30$ nm, and a refractive index 1.57. For two-dimensional structures uniform in the

z-direction, the eigenmodes can be decomposed into TM and TE polarizations. In TM mode, the only nonzero electric component is E_z, while in TE mode, the only nonzero magnetic component is H_z. When no particle is adsorbed, the numerical results show that the resonator exhibits an extremely high quality factor Q larger than 10^6 for both TM (WGM order $m = 82$) and TE ($m = 80$) modes at 1.5 μm wavelength of the coupling light. The system is operated in the under-coupling regime to get a sufficiently high quality factor. The resonant frequencies between the TM and TE modes differ by 0.63 THz, which corresponds to 4.7 nm. We note here that only the real part of the polarizability α_1 is specified via the refractive index, i.e., no intrinsic dissipation or gain is assumed. The radiation loss to free space gives rise to an imaginary part of the polarizability, which is automatically included in the numerical simulations. Likewise, it is also not necessary to specify the radiation dissipation rate γ_c of each WGM, which is automatically included in the numerical simulations. We also note that very efficient fiber-taper coupling to a high-Q resonator has been experimentally demonstrated [33].

The theoretical analysis presented in previous sections applies to both two- and three-dimensional geometry. Here, we investigate the more viable two-dimensional case that allows a quantitatively accurate check. Such a two-dimensional investigation is also relevant to the three-dimensional scenario. The WGMs can always be classified into modes symmetric (S) or antisymmetric (N) to a plane of symmetry [34]. These modes on the symmetry plane are exactly the TE and TM modes, respectively, when the wave vector of the modes does not have a component in the direction perpendicular to the symmetry plane. Moreover, in practice, the electromagnetic fields for these modes are in fact well confined and concentrated to the symmetry plane (or equatorial plane), thus these two WGMs exhibit quasi-TE and quasi-TM field structures [35, 34], which could be described by an appropriate two-dimensional structure.

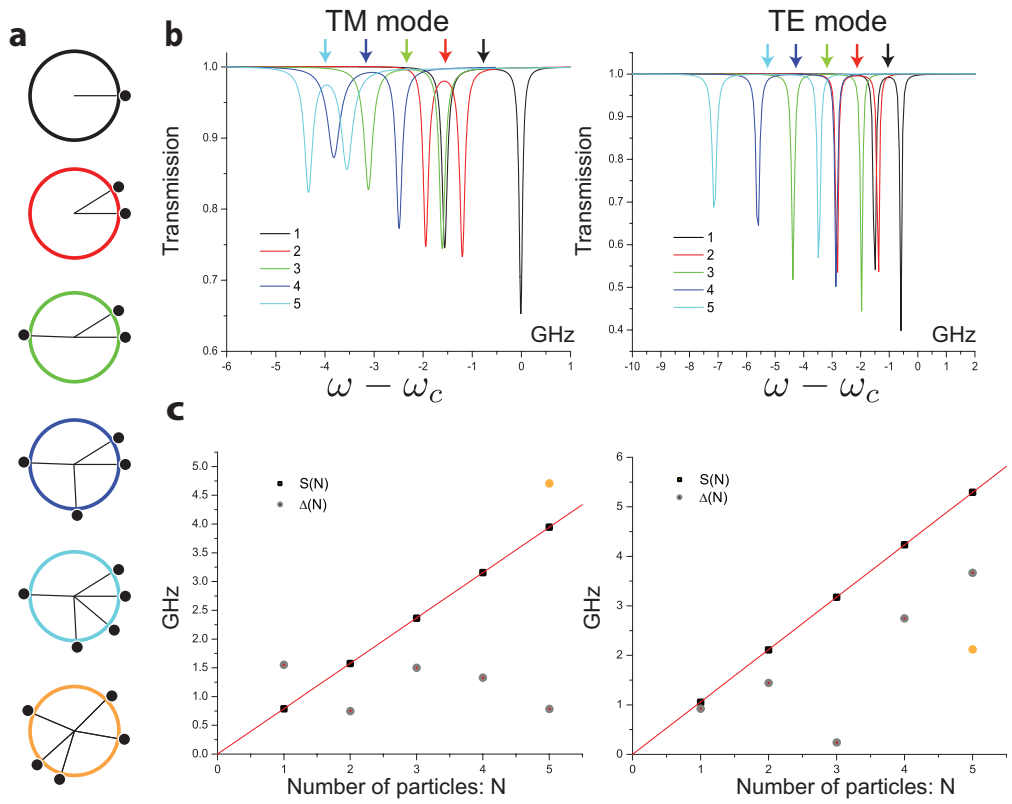

Figure 2.5: (a) Angular positions of five consecutive particles (radius $a = 30\,\text{nm}$, index $n = 1.57$) adsorbed onto the resonator. The last two configurations both have five adsorbed particles but with different angular positions. (b) Transmission spectra versus number of adsorbed particles N. The center of each spectrum is indicated by arrows of the same color. (c) Central spectral shift $S(N)$ (black square) and frequency splitting $\Delta(N)$ (grey dot) versus N. The brown dot indicates the value for the last 5-particle configuration in (a). Least square fitting yields: TM mode: $S(N) = 0.7887N\,\text{GHz}$, and TE mode: $S(N) = 1.058N\,\text{GHz}$.

2.5.2 Numerical Results

Having introduced the computational geometry, we now explore the transmission spectra with different number of adsorbed particles. To ensure the convergency of the solutions, finer meshes (i.e., more finite elements) are employed until all transmission spectra converge and stabilize. We first consider the TM mode case, wherein the proximity effect does not exist (as the electric field is in the z-direction), and thus provide a direct check for the theoretical prediction. Fig. 2.5b left panel plots the transmission spectra due to the adsorption of consecutive particles. Numerically, we have observed that the widths of the two transmission

dips become broadened as the number of particles N increases. We have also observed that Ω_c is red-shifted by an amount $S(N)$ which is precisely proportional to N, as indicated by the arrow. Also plotted is the frequency separation $\Delta(N)$ between the two transmission dips, which is not proportional to N, as it also depends on the angular positions of the particles. Ω_c however remains the same for the same number of adsorbed particles, regardless of their angular positions. For example, the last two five-particle cases in Fig. 2.5a have the same Ω_c but different Δ. Next, we investigate the TE mode case. The transmission spectra are plotted in Fig. 2.5b (right panel). Again, the two transmission dips are broadened and the center of each spectrum Ω_c is red-shifted by an amount $S(N)$ which is precisely proportional to N (Fig. 2.5c right panel). As a result of the linearity, the number of adsorbed particles N can be accurately determined by measuring the central spectral shift $S(N)$ and divided by the slope, which can be determined from either a linear fitting or from a controlled single-particle measurement. The oscillations in $\Delta(N)$ in both cases are due to the dependence on the angular positions. All these phenomena are in well agreement with the numerical results.

2.5.3 Proximity Effect

When two particles are in proximity, in addition to the external electric field, each particle experiences an additional field contribution from the nearby particle's dipole field. Accordingly, the induced dipole moment of each particle is slightly modified, which in turn induces a small change for the central spectral shift $S(N)$. To quantify the proximity effect between two particles with an edge to edge separation d, we numerically compute the spectral shift $S(2')$. Here the number of particles is primed to indicate that the proximity effect is included. When two particles are well separated ($d \gg a$), the proximity effect diminishes and one expects that $S(2')$ approaches $S(2)$ $(= 2S(1))$. Fig. 2.6 plots the ratio of $S(2')/2S(1)$. Numerically we observed that the ratio is essentially 1, when d is larger than $4a$. Moreover, the ratio decreases monotonically as d decreases, but always remain close to 1. When two

particles touches ($d = 0$), the deviation is $\simeq 1.8\%$. We conclude that the proximity effect remains small throughout the entire range of d, and the number of particles can be determined within $\simeq 1.8\%$ deviation in general cases.

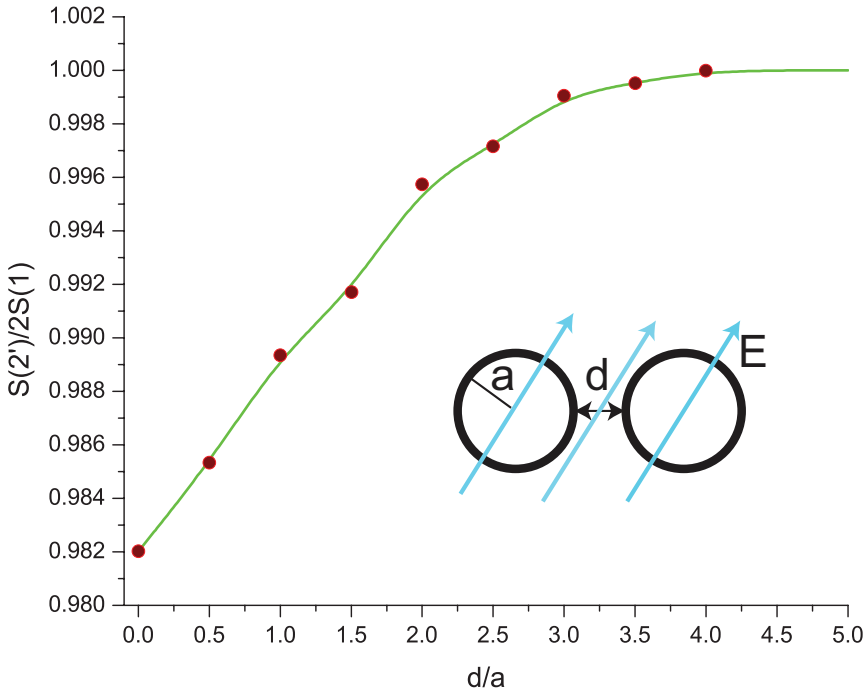

Figure 2.6: $S(2')/2S(1)$ as a function of d/a. $S(2')$ is the central spectral shift including the proximity effect. $S(1)$ is the central spectral shift due to single particle. The direction of the electric field of the WGM resonator is denoted by the light blue arrows.

To gain a deeper physical understanding about the proximity effect, here we provide a heuristic description. We first note that for the geometry of interest in practical situations, the Rayleigh particles are essentially point dipoles. For two particles in proximity ($d \simeq 0$), by decomposing the external electric field into a direction parallel ($E_{\parallel}$) or perpendicular ($E_{\perp}$) to the axis connecting the centers of the two particles, it is straightforward to show that the effective electric field experienced by each particle increases for the parallel case (i.e., the dipole field contribution $\Delta E_{\parallel} > 0$), while it decreases for the perpendicular case (i.e., the dipole field contribution $\Delta E_{\perp} < 0$) [36]. Therefore, the contributions from parallel and perpendicular components to the induced secondary spectral shift have opposite signs and tend to partially cancel each other. Specializing to the WGM resonator considered here

for TE mode with cylindrical coordinates (ρ, θ, z), $E_{\parallel}$ is in the $\hat{\theta}$-direction, and $E_{\perp}$ is in the $\hat{\rho}$-direction. By solving the mode analytically [37] (which was also checked numerically), we found that $E_\rho \simeq 1.6E_\theta$ and $E_z = 0$ at the surface of the WGM resonator (the direction of the electric field is indicated by the light blue arrows in Fig. 2.6). Thus, the induced secondary spectral shift from both cases partly cancel each other, yielding an extremely small secondary spectral shift. We note that the ratio $S(2')/2S(1)$ when $d \simeq 0$ can be either larger or smaller than 1, relying on the precise values of E_ρ and E_θ, which in turns depend on the characteristics of the system such as the dimensions and the materials. For the case considered here, $S(2')/2S(1) < 1$ when $d \simeq 0$.

For three-dimensional geometry, the contributions from the parallel and the perpendicular electric field also tend to cancel each other, so the proximity effect remains small. In particular, when two particles are close to each other, the proximity effect gives rise to a red-shift for E_θ and blue-shift for E_z and E_ρ. As an example, for a three-dimensional WGM resonator with $E_z \simeq E_\rho \simeq E_\theta$, all contributions cancel each other and the net induced additional spectral shift is essentially negligible. The proximity effect has also been studied in Ref. [] for the special case of a transverse field, which yields similar results.

2.6 Statistical Analysis

In many practical real-world applications, a particle flux that is several orders of magnitude larger. For example, in arc welding, the concentration of metal oxide is $\sim 10^6$ cm^{-3} [38]; a large concentration of particles also exists in the ambient atmosphere [39], combustion [40], or on-road aerosol due to traffic exhaust emissions [41]. In this Section, we show that a statistical theory emerge in the large particle-flux regime, which enables accurate determination of the number of nanoparticles adsorbed onto the resonator by measuring the transmission spectra; the number of particles is accurately determined by the spectral shift of the center of the

transmission spectrum, which is experimentally measurable and remarkably independent of the intrinsic dissipation of the particles as well as the angular positions of the particles. Specifically, we consider the detection of Rayleigh scatterers, which are nanoparticles that do not have a distinct resonant peak within the frequency range of interest, such as polystyrene and off-resonant molecules.

2.6.1 Transmission Spectra and Gedanken Experiments

By following the procedures presented above (describing N identical particles), the transmission spectrum for N non-identical particles adsorbed onto the resonator is given by:

$$t(\omega) = \frac{(\omega - \Omega_c + i\gamma)^2 + \Gamma^2 - |h|^2 - I}{(\omega - \Omega_c + i\gamma + i\Gamma)^2 - |h|^2 - I}, \tag{2.12}$$

where the N Rayleigh particles are characterized by the complex polarizabilities and angular positions $\{\alpha_j, \theta_j\}$, $j = 1, \cdots, N$. Again, ω is the frequency of the probing light. Γ is the tunable resonator-fiber coupling. $\Omega_c = \omega_c - 2Ng\overline{\alpha}_r$ and $\gamma = \gamma_c + 2Ng\overline{\alpha}_i$ are the normalized resonance frequency and intrinsic dissipation rate of the WGM resonator. $g = \epsilon_0|\vec{E}_0|^2/\hbar$, and has the unit of angular frequency per unit volume. $\overline{\alpha}_r$ and $\overline{\alpha}_i$, respectively, are the real and imaginary part of the average polarizability $\overline{\alpha} = \sum_{j=1}^{N} \alpha_j/N$. $I = 2g\sum_j \alpha_j(e^{2im\theta_j}h^* + e^{-2im\theta_j}h) + 4g^2\sum_{j,k}\alpha_j\alpha_k e^{2im(\theta_j-\theta_k)}$; the first term describes the scattering processes between the particles and the surface imperfection h; while the second term describes the inter-particle scattering. For any given $\{\alpha_j, \theta_j\}$, the transmission spectrum $T(\omega) \equiv |t(\omega)|^2$ has a doublet structure and the qualitative features as discussed above. Requiring $dT(\omega)/d\omega = 0$, the two transmission dips are found to be located at $\Omega_c \pm \mathrm{Re}\sqrt{I + |h|^2}$, which indicates that Ω_c is the center of the dips. Ω_c is red-shifted for positive $\overline{\alpha}_r$, and blue-shifted for negative $\overline{\alpha}_r$.

Eq. 2.12 is exact for any given set of $\{\alpha_j, \theta_j\}$ for fixed N. In practice, however, one is interested in the inverse problem: can N be determined from a measured transmission

spectrum $T(\omega)$? We show that a statistical theory emerges at the large N limit. In the statistical theory, N is regarded as an unknown, while $\{\alpha_j\}$ is considered as a set of random variables obeying some given distribution. Our theory indicates that N can be accurately determined, regardless of the values of $\{\theta_j\}$, which in general are unknown. The enabling feature is that the spectral shift of the resonance frequency of the resonator $S(N) = |\Omega_c - \omega_c| = 2Ng\overline{\alpha}_r$ is proportional to N. Notably, $S(N)$ depends only on $\overline{\alpha}_r$ but not the surface imperfection, dissipations, and the angular positions of the particles. $|\vec{E}_0|$ can be determined by either a numerical simulation, or from the measurement of $S(N = 1)$ for the one-particle case.

As a concrete example, we apply the statistical theory to the case when the sizes d of the particles are distributed log-normally: $d \sim \ln\mathcal{N}(\ln d_0, (\ln \sigma_g)^2)$, where d_0 is the geometric mean and σ_g is the geometric standard deviation; i.e., the logarithm of the size of the particles is normally distributed. The empirical values of σ_g ranges from 1.02 to 2.4. Log-normal distribution is skewed to the larger value, and is frequently adopted in modeling the size distribution of real-world particles [42]. We emphasize that the statistical theory described here can be equally applied to other distributions as well. For a spherical particle with diameter d, the polarizability is given by $\alpha(d) = 4\pi(d/2)^3(\epsilon_p - \epsilon_m)/(\epsilon_p + 2\epsilon_m)$. Here, ϵ_p is the permittivity of the particle and ϵ_m is the permittivity of its surrounding medium. From the distribution of d, the distribution of the polarizability $\alpha(d)$ can be computed. We will use $\mu \equiv \mu_r + i\mu_i$ to denote the mean complex polarizability; and σ_r, σ_i to denote the standard deviation of the real and imaginary part of $\{\alpha_j\}$, respectively. μ_r is given by $\mu_r = \int_0^\infty \alpha_r(x)\mathrm{PDF}[\ln\mathcal{N}(\ln d_0, (\ln \sigma_g)^2)]dx$, where PDF stands for the probability density function. According to the central limit theorem, the distribution of $\overline{\alpha}_r$ obeys the normal distribution $\mathcal{N}(\mu_r, (\sigma_r/\sqrt{N})^2)$; thus, the probability that $\overline{\alpha}_r$ is within one standard deviation of the mean is about 68%, and about 95% within two standard deviations. Accordingly, $S(N) = 2gN\overline{\alpha}_r$ has a probability of 68% to fall into $[2Ng\mu_r - 2\sqrt{N}g\sigma_r, 2Ng\mu_r + 2\sqrt{N}g\sigma_r]$. An estimate of the number of the particle N_m is obtained by requiring $S(N) \equiv 2gN_m\mu_r$,

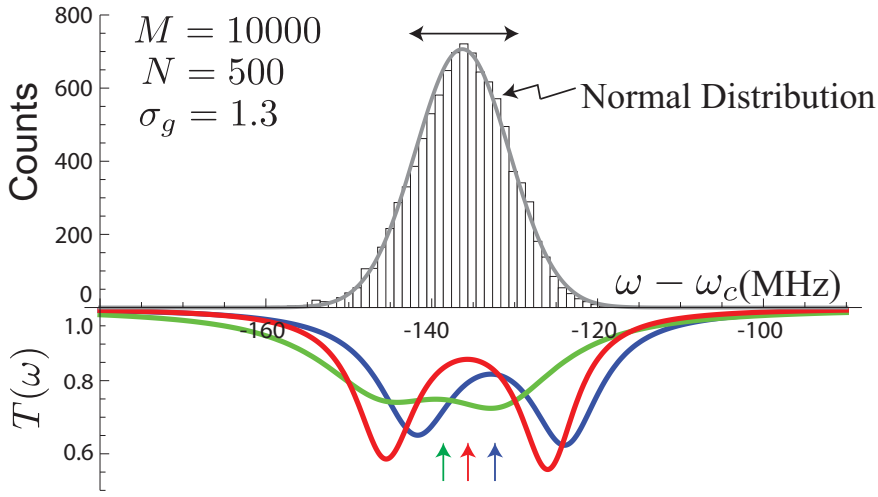

Figure 2.7: Normal distribution of $S(N)$. The fitting gray curve is the distribution $M \times \mathcal{N}(-2Ng\mu_r, (2\sqrt{N}g\sigma_r)^2) = M \times \mathcal{N}(-136.310\,\text{MHz}, (5.647\,\text{MHz})^2)$. The black arrow denotes one standard deviation. Three representative transmission spectra with varying particle dissipations with $\alpha_r(d_0)/\alpha_i(d_0) = 20$ (green), 40 (blue), and 60 (red) are plotted. The small arrow indicates the center of the spectrum.

which yields

$$N_m = \frac{S(N)}{2g\mu_r} \in [N - \sigma_N, N + \sigma_N], \tag{2.13}$$

where $\sigma_N \equiv \sqrt{N}\sigma_r/\mu_r$ is the standard deviation. Consequently, when N or N_m is large, N_m/N approaches 1 and one can substitute N_m for N into σ_N to calculate the error. Eq. 2.13 is the principal result of the statistical theory.

2.6.2 Discussions on Different Geometric Standard Deviation σ_g

To validate the statistical theory, in the following, we present the results of M independent Gedanken experiments. In each experiment, N diameters of the particles d are sampled from a log-normal distribution $\ln\mathcal{N}(\ln d_0, (\ln\sigma_g)^2)$, and their angular positions $\{\theta_j\}$ are randomly distributed in $[0, 2\pi)$. Without losing generality, we assume $d_0 = 20$ nm. We also assume $\Gamma = 1\,\text{MHz}$, $\gamma_c = 1\,\text{MHz}$, $h = 0$, and $g\alpha_r(d_0) = 0.1\,\text{MHz}$. The particle dissipation is equivalently specified by the ratio of $\alpha_r(d_0)/\alpha_i(d_0)$. The conclusion of the statistical theory do not depend on the choice of these numbers.

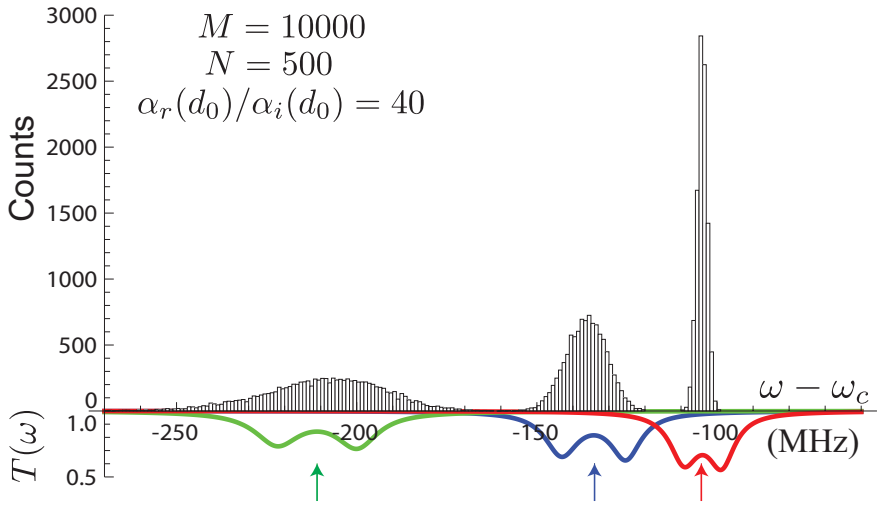

Figure 2.8: Distribution of $S(N)$ for three different geometric standard deviation: $\sigma_g = 1.5$, 1.3, and 1.1 (from left to the right). Three representative transmission spectra for $\sigma_g = 1.5$ (green), 1.3 (blue), and 1.1 (red) are also drawn.

Fig. 2.7 shows the results for the case of $N = 500$ particles and $\sigma_g = 1.3$. The histogram plots the counts versus $S(N)$ for $M = 10000$ experiments. The distribution of $S(N)$ is in well agreement with the statistical predication $M \times \mathcal{N}(2Ng\mu_r, (2\sqrt{N}g\sigma_r)^2)$. Three representative transmission spectra with different particle dissipations and angular positions are also plotted (Fig. 2.7 bottom).

We next investigate the effects of different values of σ_g for fixed N, as shown in Fig. 2.8. Both μ_r and the full width at half maximum (FWHM, which represents the standard deviation) increases as σ_g becomes larger. Again, the results from the Gedanken experiments agree with the statistical theory. For each σ_g, a representative transmission spectrum is also plotted. When σ_g is 2.0, the FWHM of the diameter distribution is 22 nm, and d ranges from 6 nm to 28 nm. Nonetheless, N_m can still be estimated fairly accurately even when σ_g is large. Table. 2.1 tabulates the relative error of N_m when σ_g increases from 1.1 to 2.4; at $\sigma_g = 1.5$, the relative error is 8%, and becomes slightly less than 40% when $\sigma_g = 2.0$.

Table 2.1: $N = 500$, and $d_0 = 20\,\text{nm}$.

σ_g	σ_N	$\frac{\sigma_N}{N} \approx \frac{N_m - N}{N}$	$\mu/\alpha(d_0)$
1.1	7	0.01	1.04
1.3	21	0.04	1.36
1.5	41	0.08	2.10
2.0	193	0.39	8.69
2.4	703	1.41	31.47

2.6.3 Discussions on Different Particle Numbers N

Also, we consider the cases of varying the number of particles N. Fig. 2.9a plots the results for $N = 250$, 500, and 750. For each case, the distribution of the spectral shift *per particle* $S(N)/N$ is plotted. The three histograms are in excellent agreement with the distributions of $\mathcal{N}(-273\text{ KHz}, (16\,\text{KHz})^2)$, $\mathcal{N}(-273\,\text{KHz}, (11\,\text{KHz})^2)$, and $\mathcal{N}(-273\text{ KHz}, (9\,\text{KHz})^2)$, respectively. The standard deviation per particle is suppressed by $\sqrt{N}$. Fig. 2.9b plots one transmission spectrum for each N. When N increases, the two transmission dips are broadened, as the total dissipation is proportional to N.

2.6.4 Applicability of the Statistical Theory

Here, we make a few comments on the applicability of the statistical theory. Our statistical theory assumes that the density coverage of the particles is not very large, i.e., no two nanoparticles are in close proximity to each other, such that the mutual polarization can be neglected. For a WGM resonator with diameter $D = 30\,\mu\text{m}$, approximately $\pi D/d_0 \approx 4700$ particles can be accommodated ($d_0 = 20\,\text{nm}$). In the Gedanken experiments, the covering ratio is roughly $500/4700 \approx 0.1$, which justifies the neglect of the mutual polarization. Our theoretic framework, however, can be extended to a high density scenario by taking into account the mutual polarization.

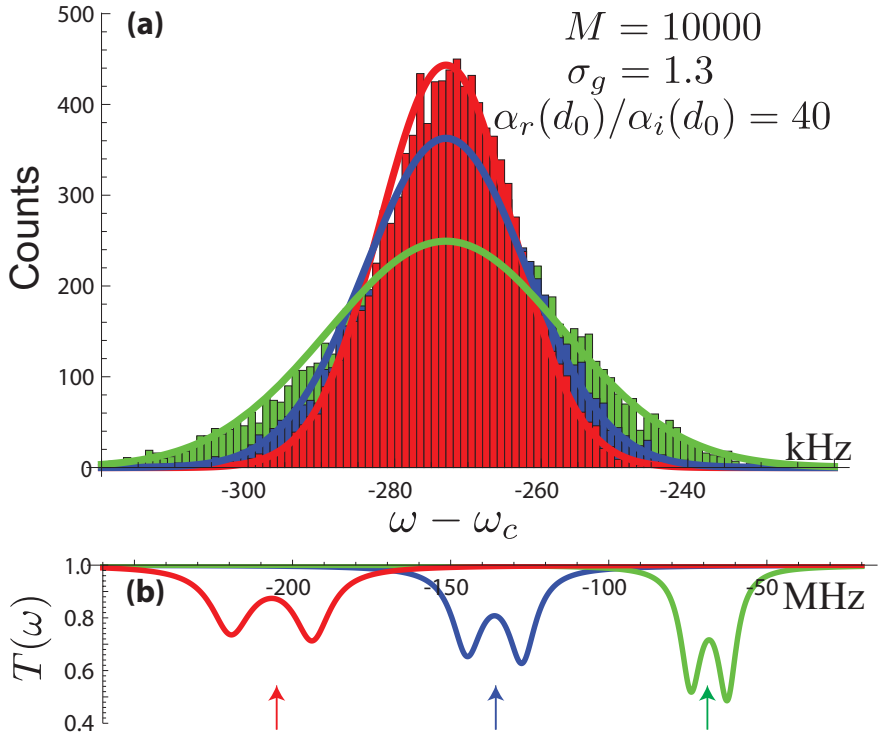

Figure 2.9: (a) The distribution of the spectral shift per particle $S(N)/N$ for $N = 250$ (green), 500 (blue), and 750 (red). The fitting curve is the normal distribution $\mathcal{N}(-2g\mu_r, (2g\sigma_r/\sqrt{N})^2)$. (b) Representative transmission spectrum for each N.

2.7 Summary and Expectation

In this Chapter, we have presented the theory of nanoparticle sensing using WMG resonators for both plasmonic and Rayleigh scatteres. In particular, we describe how to extract critical information, such as the number of particles adsorbed, from the transmission spectrum. Moreover, a rigorous numerical validation for accurate determination of the number of Rayleigh scatterers is also performed. Compared with other sensing techniques such as angle-resolved interferometry and optical coherence tomography, the mechanism described here is more robust, as it does not require detailed information regarding angular positions or shapes of each particle. Finally, we comment on some of the important issues in practical detection. Firstly, we discuss the effects of the presence of the surface imperfections ($h \neq 0$). The sensitivity as well as the accuracy for the estimation of the particle number and locations of the transmission dips degrade with increasing surface imperfection. The surface

imperfection breaks the degeneracy of the two WGMs, and splits the single transmission dip into a doublet in the under-coupling regime [28, 21]. As the adsorbed particles are intrinsically (spatially localized) surface imperfections, such a doublet structure from non-zero h will superimpose upon the induced structures due to the particles in the transmission spectra, and therefore masks the information about the particles. We note that however one could still obtain the information by numerically fitting the transmission spectrum using Eqs. (2.4) or (2.8) for the non-zero h case. Secondly, our formalism is capable of describing the full spatiotemporal dynamics of the system, and applies to other scenarios. For example, when nanoparticles fly by the resonator slowly and closely but do not get adsorbed (which is desired when washing off the adsorbed particles is not practical), the dynamics can be analyzed by the full theory presented here.

Chapter 3

Single-photon Optical Diode

3.1 Introduction

Another interesting application in nanophotonic system is to achieve optical isolation down to single-photon levels. Complete optical isolation is critically important for all optical devices. In view of all practical applications, parasitic reflection between optic devices can have deleterious effects on the operations, especially for those based on interferometry designs. To ensure the proper operations of the optical devices, optical diodes are used to prevented those unwanted feedbacks. The name optical diode is originated from the name of the electronic diode. An electronic diode allows an electric current to pass in one direction with a transmission close to unity, while in the other direction, the transmitted current is almost zero. This unidirectional behavior called rectification can be used to convert alternating current into direct current. By using a similar definition, an optical diode is a spatially nonreciprocal device which allows unidirectional propagation of a signal, acting as an optical isolator at a given wavelength [43]. In an ideal case, its transmission is 100% in the forward direction ($T_f = 1$), while it vanishes for the backward direction ($T_b = 0$), yielding a unitary contrast number $\eta \equiv |(T_f - T_b)/(T_f + T_b)| = 1$. To achieve this optical isolation, various possible solid-state optical diodes have been proposed or demonstrated before, ranging from

standard bulk Faraday rotators (due to small Verdet constant, the Faraday rotators are typically of centimeter size [44, 45]); to thin film devices based on magneto-optic effects in a Mach-Zehnder geometry at centi-meter scale [46]; use of a graded gain medium with a 10 cm long glass capillary filled with ethanol [47]; and approaches that tailor the nonlinear responses which require certain optical power so that the nonlinearity manifests [48, 43]. Recent advances in single-photon sources [49, 50, 51, 52] and Nano scale fabrication make on-chip quantum optics and information processing attainable. Therefore, with the capability of controlling light-matter interactions in ultra-low power regimes and even down to single-photon levels [53, 54], it is desirable to achieve optical signal isolation at the single-photon level within sub-μm chip-scale for integrated nano-photonics. In the following, we show that near complete optical isolation can be achieved at the single-photon level by coupling a quantum impurity to a passive, linear waveguide which has a locally planar, circular polarization. Such a configuration does not rely upon the use of bulk nonlinear materials or quasi-phase matching, and has a sub-μm footprint that can be conveniently implemented in various types of waveguides.

3.2 Configurations

We start by describing the configuration of the single-photon diode. The diode is accomplished by coupling a quantum impurity to a passive, linear waveguide (Fig. 3.1a). The waveguide is a single-polarization single-mode (SPSM) waveguide, with a planar and circular polarization at the location of the impurity at a fixed frequency (the operating frequency). The circularly polarized state reverses its orientation for opposite wave vectors (Fig. 3.1b), due to time-reversal symmetry. We will take the polarization plane as the x-y plane. With an external dc magnetic field B in the z-direction that breaks the time-reversal symmetry, the energy levels of the impurity are Zeeman-split and each level couples to one circularly

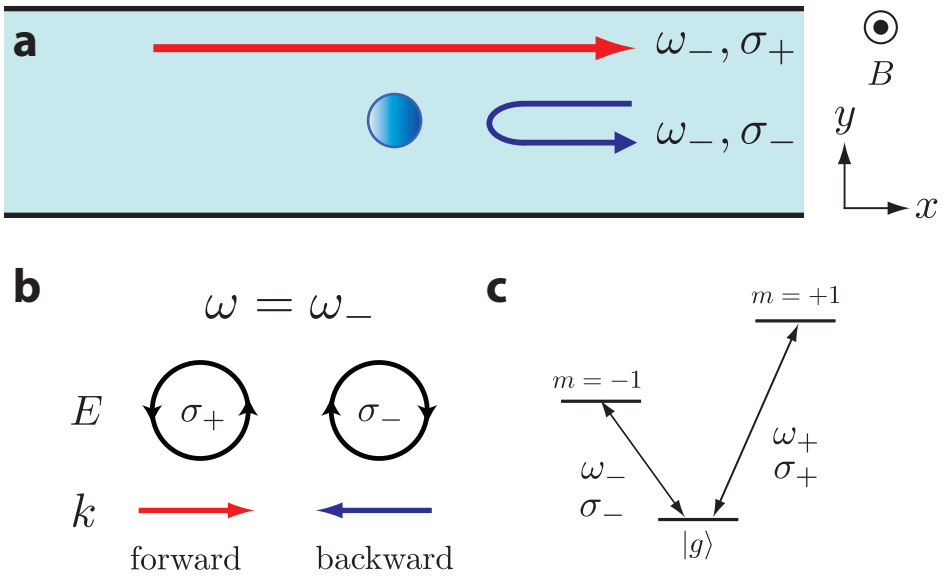

Figure 3.1: Schematics of the single-photon diode. (a) A quantum impurity (blue dot) is coupled to a passive, linear SPSM waveguide. (b) At the operating frequency, the waveguide possesses a locally planar circular polarization. The polarization reverses its orientation for opposite wave vectors. (c) The energy level diagram with the presence of an external magnetic field.

polarized state (Fig. 3.1c). The design strategies and rigorous conditions for SPSM waveguides have been discussed before [55]; numerically, we found that a locally planar circular polarization can be achieved for a variety of waveguides, as will be shown below. The impurity can be a quantum dot [56, 57, 58], or an atom doped in semiconductors [59, 60, 61]. The transition frequencies of different quantum impurities cover a wide range from microwave to far-infrared.

We note that in this configuration the wave vector $\mathbf{k}$ is perpendicular to the magnetic field B, which is the same as in the Voigt (transverse) configuration and is different from the Faraday (longitudinal) configuration [62] wherein $\mathbf{k}$ is parallel to B. Moreover, the wave vector and the polarization lie in the same plane that is perpendicular to the magnetic field. Such a unique configuration is possible only in a confined geometry, such as a waveguide. When coupled to a dipole, the interaction between the dipole and the photon field is given

by

$$
\begin{aligned}
H_I &= -\mathbf{d}\cdot\mathbf{E} \\
&= -\left(\frac{d_x+id_y}{\sqrt{2}}\frac{E_x-iE_y}{\sqrt{2}}+\frac{d_x-id_y}{\sqrt{2}}\frac{E_x+iE_y}{\sqrt{2}}+d_zE_z\right) \\
&\equiv -\left(d_+E_+ + d_-E_- + d_zE_z\right), \qquad (3.1)
\end{aligned}
$$

where the in-plane electric field is decomposed into a linear combination of left- and right-hand circular components as $E_x\hat{\mathbf{x}} + E_y\hat{\mathbf{y}} = E_+\hat{\sigma}_+ + E_-\hat{\sigma}_-$ (here $\hat{\sigma}_\pm = \left(\hat{\mathbf{x}} \pm i\hat{\mathbf{y}}\right)/\sqrt{2}$ corresponds to the left- and right-hand circular polarization unit vectors [63]). In the case of electric or magnetic $\Delta m = \pm 1$ dipole transitions, the impurity interacts only with the circularly polarized photon modes $\sigma_\pm$ (Fig. 3.1). The selection rules state that the $\Delta m = 1$ transition couples to σ_+ polarization and only d_+ has non-zero matrix elements, while the $\Delta m = -1$ transition couples to σ_- polarization and only d_- has non-zero matrix elements. For dipole transition with transition frequency ω_d, the transmission and reflection amplitudes of the photon at frequency ω are given by $t(\omega) = (\omega - \omega_d + i\gamma)/(\omega - \omega_d + i\Gamma + i\gamma)$ and $r(\omega) = i\Gamma/(\omega - \omega_d + i\Gamma + i\gamma)$, where Γ is the external linewidth of the dipole due to waveguide-quantum dot coupling, and γ is the intrinsic dissipation rate of the quantum dot [64, 65]. The transmission and reflection coefficients are given by $T(\omega) = |t(\omega)|^2$ and $R(\omega) = |r(\omega)|^2$.

We now describe the operating scheme for achieving the photonic rectification: For a photon entering from the left (the "forward" direction) with frequency ω_-, since the photon mode is σ_+ polarized at the location of the impurity, the photon couples only to the $m = 1$ atomic state that has a transition frequency ω_+; for a large frequency mismatch ($\omega_+ - \omega_- \gg$ the frequency bandwidth of the pulse), the photon will not interact appreciably with the impurity and has a perfect transmission ($T_f = 1$). On the other hand, when the photon enters from the right (the "backward" direction) with frequency ω_-, since the photon mode is σ_- polarized at the location of the impurity, the photon interacts resonantly with the $m = -1$ atomic

state, giving rise to a zero transmission ($T_b = 0$) [64] and thus yields a unitary contrast. We emphasize that the polarization of the waveguide mode at frequency ω_+ is not important for the operation. Alternatively, the photonic rectification can be achieved at frequency ω_+ when the waveguide is designed to have a locally planar, circular polarization at ω_+. In this case, the forward and backward directions are reversed: photons entering from the right are now perfectly transmitted, while photons incident from the left are completely reflected.

3.3 Waveguide Designing

Having introduced the device configuration and the basics of the operating scheme, we now present designs of SPSM waveguides that possess locally planar circular polarization.

3.3.1 Line Defect Waveguide

The first example is a two-dimensional (uniform in the z-direction) line defect waveguide in silicon (dielectric constant $\epsilon = 13$), formed by removing a row of air columns from an otherwise-perfect triangular lattice of air columns (Fig. 3.2a). Such a system is known for having a broad complete photonic band gap for both transverse electric (TE, electric field in the x-y plane) and transverse magnetic (TM, magnetic field in the x-y plane) modes [35]. In particular, the ratio between the radius of the air hole r and the lattice constant a is 0.48, a 18.6% complete photonic band gap can be obtained [35]. Fig. 3.2b plots the band structure of the line defect waveguide along the $\Gamma - K$ direction, which exhibits a complete band gap extending from 0.42 ($2\pi c/a$) to 0.51 ($2\pi c/a$). In particular, from the frequency range 0.45 ($2\pi c/a$) to 0.47 ($2\pi c/a$), the waveguide is an SPSM waveguide as only TE mode exists.

The line defect waveguide has discrete translational symmetry along the waveguide; the polarization pattern thus is periodic in the x-direction with a periodicity a. To investigate

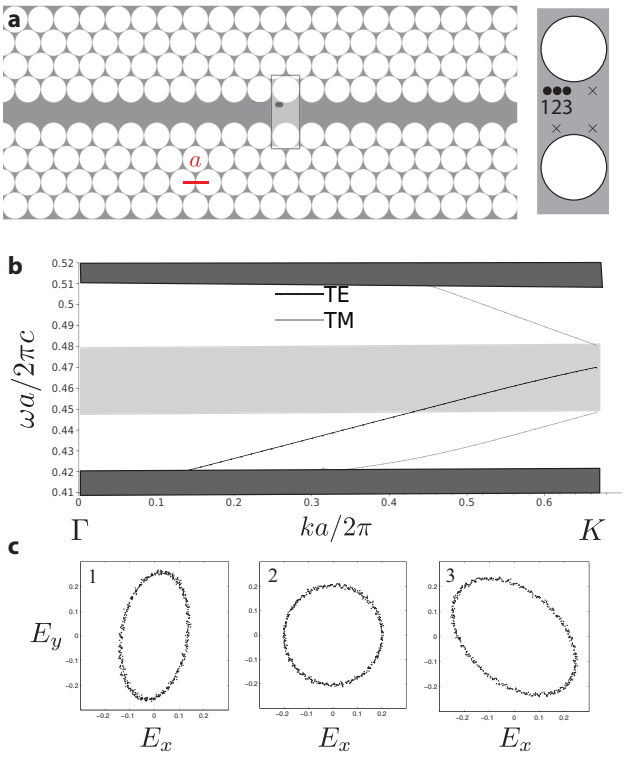

Figure 3.2: Schematics and polarization states of a line defect waveguide. (a) A line defect waveguide in silicon ($\epsilon = 13$) with triangular lattice of air columns. A unit cell (along the x-direction) of the waveguide is shown on the right. (b) The band structure of the waveguide. In the frequency range from 0.45 ($2\pi c/a$) to 0.47 ($2\pi c/a$), only TE mode exists and the waveguide is an SPSM waveguide. (c) The polarizations at three representative points (shown by black dots in (a)) at $\omega = 0.46$ ($2\pi c/a$). The polarization can be expressed in the form $a_x \cos(\omega t + \phi_x)\,\hat{\mathbf{x}} + a_y \cos(\omega t + \phi_y)\,\hat{\mathbf{y}}$. For point 2, the relative deviations for $|\Delta a/a_x|$ and $|\Delta\phi/(\pi/2)|$ are 1.3% and 1.4%, respectively.

the spatial variation of the polarization within a unit cell (Fig. 3.2a right), we scan through a horizontal line which locates at a distance $0.546\,a$ from the center of the closest air hole. Fig. 3.2c plots the polarizations at three representative points within the unit cell which are located at a distance from the left edge of the unit cell $0.15\,a$, $0.23\,a$, and $0.30\,a$, respectively, at frequency $\omega = 0.46\,(2\pi c/a)$. The polarization at point 2 is found numerically to be circular. Moreover, we have numerically confirmed that only four points within the unit cell possess circular polarization: Besides point 2, the other three points (indicated by $\times$ in Fig. 3.2a) are obtained through mirror symmetry with respect to the center of the unit cell.

3.3.2 Holey-cavity Waveguide

Another example is a 2-dimensional Holey-cavity waveguide [66]: a dielectric waveguide perforated with a periodic sequence of twelve air holes (Fig. 3.3a). A resonant cavity mode is introduced by increasing the distance between the two central air holes. The dielectric material is assumed to be Pyrex glass with $\epsilon = 5$. Such a structure has been used as a filter, as the resonant mode gives rise to a transmission peak in the middle of the band gap. Fig. 3.3b plots the transmission spectrum for both TE and TM modes. Within the frequency range from $0.275\,(2\pi c/a)$ to $0.296\,(2\pi c/a)$, only the TE mode exists, and the structure is an SPSM waveguide. At the point in one of the air holes (Fig. 3.3a), the polarization at frequency $0.293\,(2\pi c/a)$ is circular (Fig. 3.3c). The point is located in an air hole so that an impurity can be placed.

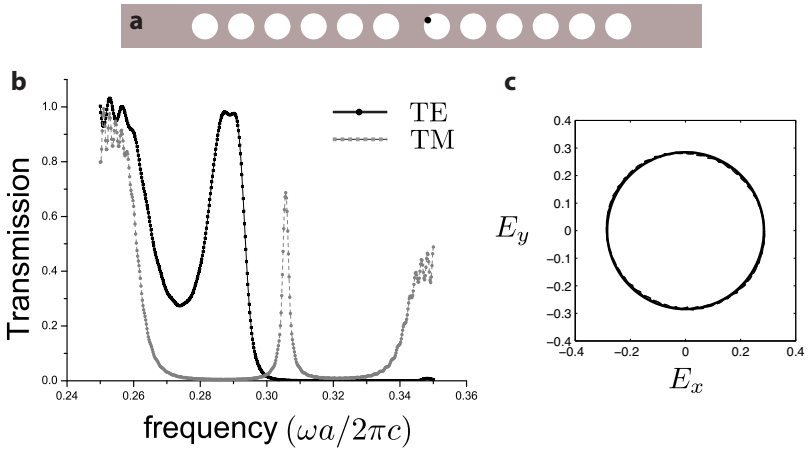

Figure 3.3: Schematics and polarization state of a holey-cavity waveguide. (a) The structure of the holey-cavity waveguide. The width of the waveguide is $1.2a$. The holes have a radius $0.36a$, and are separated by a distance a, except for the two center holes that form the cavity are separated by a distance $1.4a$. (b) The transmission spectra for both TE and TM modes. (c) The circular polarization at the point shown in (a) at frequency $\omega = 0.293\ (2\pi c/a)$. Circular polarization exists at other three points via mirror symmetry.

3.4 Practical Considerations

A practical diode must be able to operate over a finite frequency bandwidth. For a photon pulse with a finite frequency bandwidth, at detuned frequencies $\omega \neq \omega_-$ (the operating frequency), there are two possible predominant degrading factors to the performance of the diode: (1) the polarization becomes elliptic; an elliptic polarization is a linear superposition of both σ_+ and σ_- states, and thus couples to *both* transitions $\Delta m = \pm 1$; and (2) imperfect transmissions in both directions [64] (i.e., $T_f(\omega) \neq 1$ and $T_b(\omega) \neq 0$) at off-resonant frequencies $\omega \neq \omega_-$. Moreover, the intrinsic dissipation of the quantum dot should also be considered. Here we examine these issues and show that complete photonic rectification can still be achieved for a photon pulse.

3.4.1 Dynamics of the Photon Pulse

In general, for an incoming pulse $\phi(x,t)$ propagating in a waveguide with wave form $\phi(x,t) = \int d\omega\, g(\omega) e^{ik(\omega)x - i\omega t}$, the *pulse* transmission T and reflection R are generalizations of above mentioned $T(\omega)$ and $R(\omega)$; in this case, one needs to take into account the Fourier component $g(\omega)$ of the pulse, as well as the waveguide mode polarization. T and R are given by:

$$T = \frac{\int d\omega \left\{u^2(\omega)|g(\omega)t_+(\omega)|^2 + v^2(\omega)|g(\omega)t_-(\omega)|^2\right\}}{\int d\omega |g(\omega)|^2}, \tag{3.2}$$

$$R = \frac{\int d\omega \left\{u^2(\omega)|g(\omega)r_+(\omega)|^2 + v^2(\omega)|g(\omega)r_-(\omega)|^2\right\}}{\int d\omega |g(\omega)|^2}; \tag{3.3}$$

where $t_\pm(\omega)$ and $r_\pm(\omega)$ are the transmission and reflection amplitudes at frequency ω for the $\Delta m = \pm 1$ transitions, respectively (i.e., $\omega_a = \omega_\pm$). $u(\omega)$ and $v(\omega)$ are real numbers which describe the ellipticity of the polarization in the waveguide as a function of frequency: The polarization at frequency ω is decomposed as $u(\omega)\hat{\sigma}_+ + v(\omega)\hat{\sigma}_-$. ($\hat{\sigma}_\pm = (\hat{\mathbf{x}} \pm i\hat{\mathbf{y}})/\sqrt{2}$ corresponds to the left- and right-hand circular polarization unit vectors.) For circular

polarization, $(u, v) = (1, 0)$ or $(0, 1)$; for elliptic polarization, $0 < u, v < 1$. The pulse transmission and reflection are equal to the area ratios of the transmitted and reflected pulses, respectively, to the input pulse. Thus, to compute pulse transmission and reflection numerically, one uses the strategy: (i) compute numerically the polarization throughout the bandwidth, and compute the ellipticity to obtain $u(\omega)$ and $v(\omega)$; (ii) for each frequency within the bandwidth, compute $t_\pm$ and $r_\pm$; and (iii) use Eqs. (3.2) and (3.3) to compute T and R for both forward and backward directions.

Fig. 3.4a plots the polarizations over a frequency range of 10 GHz, assuming the center frequency ω_- corresponds to 1.55 μm wavelength (the lattice constant for the line defect waveguide $a = 0.713\,\mu$m). The polarizations remain essentially circular throughout the entire 10 GHz frequency bandwidth, which corresponds to a pulse with a temporal width $\simeq 0.1$ ns. To investigate the effects of imperfect transmissions at detuned frequencies, we numerically simulated the dynamic process of the propagation of a photon pulse by solving the following set of equations of motion [64]

$$i\partial_t \phi_R(x,t) = -iv_g \partial_x \phi_R(x,t) + V\delta(x) e_a(t), \tag{3.4}$$

$$i\partial_t \phi_L(x,t) = +iv_g \partial_x \phi_L(x,t) + V\delta(x) e_a(t), \tag{3.5}$$

$$i\partial_t e_a(t) = \omega_\pm e_a + V\left(\phi_R(0,t) + \phi_L(0,t)\right), \tag{3.6}$$

where $\phi_R(x,t)$ and $\phi_L(x,t)$ are the wave functions of the right-moving and left-moving photons, respectively; $e_a(t)$ is the quantum dot excitation; V is the waveguide-impurity coupling; v_g is the group velocity of the photon in the waveguide; and $\omega_\pm$ are the transition frequencies for $\Delta m = \pm 1$ transitions. The quantum dot is located at $x = 0$. The above set of the equations of motion already takes into account that the polarizations remain circular throughout the frequency bandwidth of the photon pulse. The general case when the polarization becomes non-circular within the pulse bandwidth can be numerically solved in the same manner and will be presented elsewhere. To solve the equations of motion numerically,

we use the pseudo-spectral method in coordinate space with a non-uniform grid to evolve an initial state specified by $\phi_R(x,0)$, $\phi_L(x,0)$, and $e_a(0)$. The input pulse enters from the left (forward direction) or the right (backward direction); in each case, the quantum dot is initially in the ground state ($e_a(0) = 0$).

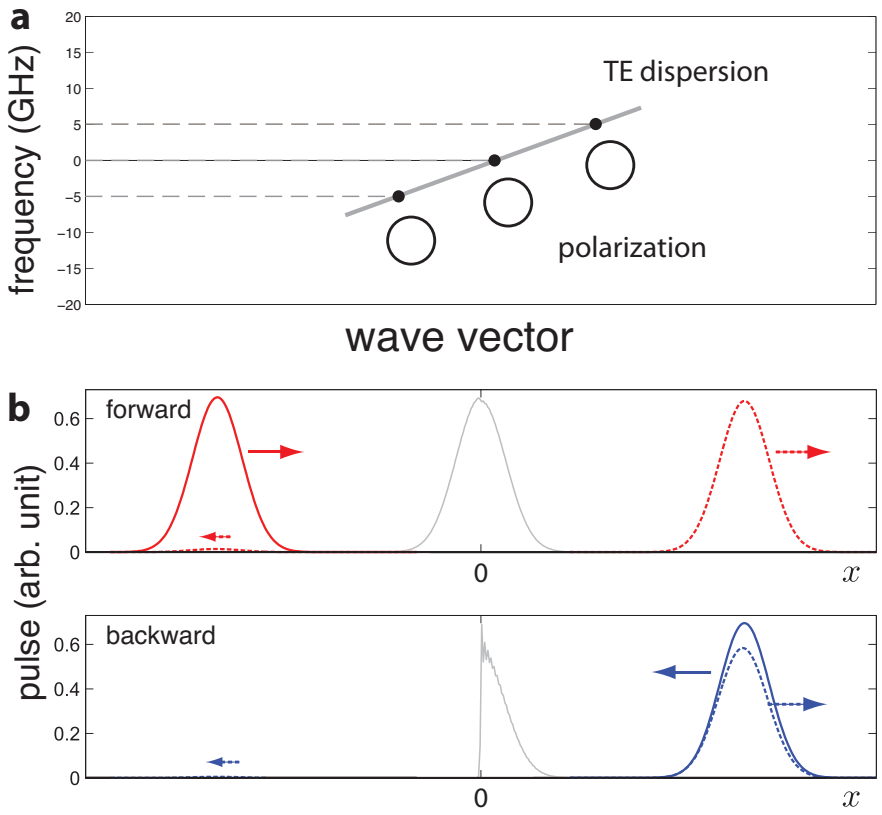

Figure 3.4: Photonic rectification for a pulse with a finite frequency bandwidth. (a) The polarization remains essentially circular throughout a 10 GHz bandwidth, centered at a frequency corresponding to 1.55 μm wavelength. (b) Non-reciprocal pulse propagation in the waveguide at sequential time steps. The transmission in the forward direction is $T_f = 97.6\%$ (upper panel), and is $T_b = 0.7\%$ in the backward direction (lower panel). The input pulse is a 50 ns Gaussian pulse at 1.55 μm wavelength.

The input pulse is a 50 ns Gaussian pulse at 1.55 μm wavelength, which corresponds to a frequency bandwidth $\Delta B = 0.44/(50\times10^{-9}) = 8.8\times10^{-3}$ GHz $\ll$ 10 GHz. (The rectification function is independent of the pulse shape.) The impurity is an InAs quantum dot located at $x = 0$, with experimental values of radiative lifetime $\tau_r = 2.2$ ns and non-radiative lifetime $\tau_{nr} = 24$ ns, respectively, at 180 K [67]. The external linewidth Γ of the quantum dot due to waveguide-quantum dot coupling is given by $\Gamma = 2\pi/\tau_r = 2.86$ GHz; and the intrinsic

dissipation rate of the quantum dot is given by $\gamma = 2\pi/\tau_{nr} = 0.262\,\mathrm{GHz}$. The angular frequency separation is $\Delta\omega = \omega_+ - \omega_- = 20\,\mathrm{GHz}$ ($\omega_- = 1215.26\,\mathrm{THz}$, and $\omega_+ = 1215.28\,\mathrm{THz}$ at $0.108\,\mathrm{Tesla}$). The Zeeman splitting for this frequency separation is calculated using an effective electron mass of $m_e/2.1$ [68]. Both Γ and $\Delta\omega$ are much larger than the pulse bandwidth. The group velocity v_g can be directly read off from the dispersion diagram of the waveguide; for the photonic line defect waveguide as shown in Fig. 3.2b, $v_g = 0.09c$ (c is the speed of light in vacuum); V is obtained from $\Gamma = V^2/v_g$ [64]. Fig. 3.4b plots the non-reciprocal pulse propagation at sequential time steps: The input pulses are indicated by the thick lines, the transmitted and reflected pulses by dash lines; the gray lines show the pulse interacting with the quantum dot. In the forward direction, the transmission is $T_f = 97.6\%$ (defined as the area ratio of the transmitted pulse to the input pulse), and $R_f = 2.0\%$ (defined as the area ratio of the reflected pulse to the input pulse); while in the backward direction, the transmission is $T_b = 0.7\%$ and $R_b = 83.9\%$, yielding a contrast $\eta = 0.986$. Note that in the backward direction, the pulse interacts resonantly with the quantum dot, giving rise to a small time delay $\simeq 1.1$ ns, approximately 2.2% of the pulse width. For the case of larger intrinsic dissipation with $\gamma/\Gamma = 0.25$, in the forward operation, we obtained $T_f = 97\%$ and $R_f = 2\%$; while in the backward direction, we obtained $T_b = 4\%$ and $R_b = 64\%$, yielding a contrast of 0.92. The reflected pulse in the backward direction experiences a time delay of 1.1 ns. The time delay keeps the same in both cases, as in both cases $\gamma \gg 2\pi\Delta B$ (the pulse bandwidth). For the cases where $2\pi\Delta B \gg \gamma$, the time delay of the reflected pulse would be sensitive to the values of γ. The simulation results indicate that the intrinsic dissipation does not seriously impede the performance of the diode, as in the forward direction the off-resonant pulse interacts weakly with the quantum dot, and thus is insensitive to the dissipation; in the backward direction the transmission $T_b \simeq (\frac{\gamma}{\gamma+\Gamma})^2$, and the reflection $R_b \simeq (\frac{\Gamma}{\gamma+\Gamma})^2$ for a resonant scattering process [64]. As a result, the contrast is not susceptible to intrinsic dissipation when $\gamma \ll \Gamma$.

3.4.2 Displacement Inaccuracy

Another practical concern is the experimental limitation in precisely positioning the quantum dot, which has been a major obstacle in achieving deterministic photon-quantum dot coupling [69]. The spatial accuracy of placing the quantum dot by electron-beam lithography is $\sim 25\,\mathrm{nm}$, due to imprecision in the electron-beam registration and writing; comparable accuracy has been reported in other photonic systems [70, 71, 72]. We have numerically evaluated the contrast at several sample points which are spatially away from the ideal point with circular polarization (point 2 in Fig. 3.2a), using Eq. 3.2 (note that in Fig. 3.2a, the distance between point 1 and point 2 is 57 nm when $a = 0.714\,\mu\mathrm{m}$). At the point 30 nm to the right of point 2, $u \simeq 3.5v$, while at the point 30 nm to the left of point 2, $u \simeq 3.6v$; the contrasts at both points are larger than 0.85, close to that in a periodically poled lithium niobate waveguide [43]. The contrast in fact can be accurately expressed as $\sim (u^2-v^2)/(u^2+v^2)$ when $\Gamma \gg \gamma \gg \Delta B$. These results demonstrates the practicality of the proposed device.

3.5 Summary and Expectation

In this Chapter, we design a single-photon optical diode that can operate on the individual photons. Such a realization is accomplished by coupling a quantum impurity to a SPSM waveguide at the position that holds a circular polarization. Specifically, two types of two-dimensional photonic crystal waveguide which holds locally circular polarizations are designed. Numerically, we show that this optical diode yields a contrast number to be 0.986, and its performance is not sensitive to the intrinsic dissipation of the quantum impurity.

Finally, we briefly discuss the full three-dimensional realizations for the single-photon optical diode. To achieve a full three-dimensional device, we note that if the structure has a mirror symmetry plane at $z = 0$, the eigen-modes within the symmetry plane ($z = 0$) are

purely TE and TM polarized [35]; moreover, for thin structures with a mirror symmetry, the modes are essentially TE-like and TM-like, as long as the waveguide thickness is smaller than the wavelength. Alternatively, to emulate the states of the 2-dimensional structures, one can sandwich a 3D photonic structure by perfect magnetic conductors [73, 74] to obtain the TE states equivalent to the model 2-dimensional photonic system. Furthermore, for 3-dimensional waveguides that have continuous translational symmetry along the waveguide direction such as fibers, the polarization would remain unchanged along a line parallel to the axis of the waveguide, a feature that could help alleviate the requirement of precise position of the impurity when the waveguides have only discrete translational symmetry. 3-dimensional SPSM waveguides with continuous translational symmetry have been demonstrated, for example, by employing the stress-induced birefringence in the core region in optical fibers [75], or by using different sizes of air holes in photonic crystal fibers [76], where the mode degeneracy is broken by lifting the rotational symmetry on the cross-section of the waveguide. Through fine-tuning the characteristics such as the stress, or the size and arrangement of air holes, a planar circular polarization may be attained.

Chapter 4

Correlations in Multiphoton Scattering Processes

4.1 Introduction

Applications discussed in the previous Chapters are dominated by the single-photon scattering process. In those nanophotonic systems, the mean photon number is much smaller than one [30] and photon correlations are not being taken into considerations. Nonetheless, in many situations, there has been greatly growing interest in engineering the photon correlations and their applications. This interest stems partly from the advent of the experimental capability of controlled generation of multi-photon Fock states in a solid-state system (the photon number $N \leq 6$ in current experiments [77]). When the photonic wavefunction of the Fock state is not a product state of the wavefunctions of the constituent individual photons, the photons are correlated. We call such states correlated photonic Fock states. Correlated photonic Fock states are potentially useful in many applications. For example, a highly bunched N-photon Fock state, which exhibits an effective wavelength that is N times smaller than that of individual photons [78], could achieve deep subwavelength optical lithography [79, 80] and super resolution in optical imaging [81, 82]. On the other hand,

Fock states which exhibit anti-bunching behavior and sub-Possionian statistics provide ultra quiet photon sources with sub-shot-noise power level and also make possible single-photon sources for quantum information processing [83, 84]. Nonetheless, a comprehensive theoretical description in solid-state quantum electrodynamics (QED) systems on how the photon correlations emerge in photonic Fock states by scattering means has not been presented before. One of the sources of difficulty is the proper treatment of the boundary conditions for an infinite system for the optical fields of interests. Conventionally, periodic or hard-wall boundary condition has been employed to truncate the system size to make the computation region finite. Although computationally convenient, those boundary conditions do not describe the correct physical settings in an infinite physical system. Furthermore, due to the mathematical complexity, the exact solutions of the scattering problems were postulated using the Bethe ansatz [85], instead of being derived directly. Not until very recently, have approaches using open boundary conditions been employed to investigate the 2-photon Fock state scattering problems [86, 87]. These approaches do not assume the Bethe anstaz as *a priori* assumption. However, the direct generalizations of these approaches to describe the N-photon Fock state ($N > 2$) scattering problems are subtle, mainly due to the emergence of multiple photonic threshold bound states [88]. In this study, we provide a detailed investigation for the N-photon Fock state scattering problems in a waveguide QED system which consists of an one-dimensional waveguide coupled to a two-level atom. Such a system provides the simplest realization for the photon-atom interactions in waveguide QED systems. Notably, The fermionic degree of freedom in the atom induces interplay between the photons, which fundamentally changes the photon correlations. Specifically, without relying on any ansatz, we employ the open boundary conditions to solve the N-photon Fock state scattering processes by explicitly constructing a complete set of eigenstates of the system. The constructed eigenstates contain very rich mathematical structures. For instance, for the 3-photon Fock state, there are in total three types of eigenstates with different physical nature: a 3-photon extended state, a 3-photon threshold bound state, and a hybrid state

that is linear superposition of: a 3-photon bound state and a product state of a 2-pbound state and an extended state. For the general case of the N-photon Fock state, we show that the total number of different types of the eigenstates is exactly described by the integer number partition function $Z(N)$; the set of eigenstates in general includes hybrid states of multi-photon extended states and multi-photon threshold bound states, formed by all possible partitions of the photon number N. To construct the scattering matrix, which encodes all the information of the scattering process, it is vital that the set of the in-states and out-states that are obtained from the set of eigenstates are complete. For this purpose, we develop a numerical scheme to check this property. Finally, as a concrete example, we consider the case of the 3-photon Fock state, and compute the third-order correlation function to demonstrate the bunching and anti-bunching behaviors in the scattered photon states. Those nontrivial bunching and anti-bunching behaviors are closely related to the existence of the threshold bound states.

4.2 The Hamiltonian for a Waveguide QED System

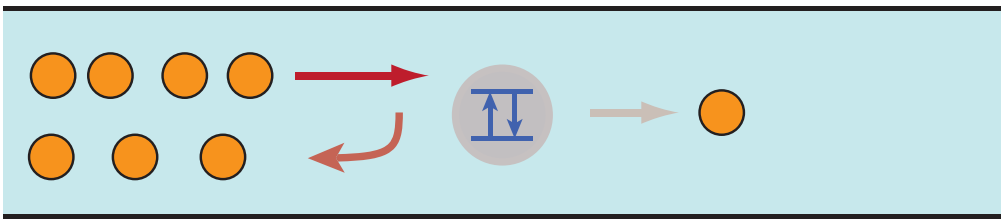

Figure 4.1: Schematics of the described system. An one-dimensional waveguide is coupled to a two-level atom. Multiple photons are incident from the left side and are scattered by the two-level atom. Each photon can be either reflected or transmitted after scattering.

The system of interest is depicted in Fig. 4.1, which consists of an one-dimensional waveguide coupled to a two-level system. The two-level system can be a quantum dot [89, 90], a superconducting qubit [91, 92], a nitrogen vacancy center [93], or an atom [94, 95], and hereafter is referred to as 'an atom'; the one-dimensional waveguide, for example, can be a line-defect waveguide in a photonic crystal [96] or an optical fiber. To have a robust

realization of such a waveguide QED system, it is required to have a sufficiently large β-factor [97, 98], which describes the spontaneous emission efficiency into the waveguide. The Hamiltonian of the entire waveguide QED system is described by

$$\begin{aligned} H/\hbar = &\int dx(-i)vC_R^\dagger(x)\frac{\partial}{\partial x}C_R(x) + \int dx\, ivC_L^\dagger(x)\frac{\partial}{\partial x}C_L(x) \\ &+ \int dx\bar{V}\delta(x)[C_R^\dagger(x)\sigma_- + C_R(x)\sigma_+ + C_L^\dagger(x)\sigma_- + C_L(x)\sigma_+] + \omega_e a_e^\dagger a_e + \omega_g a_g^\dagger a_g. \end{aligned} \tag{4.1}$$

Here, v is the group velocity of the photons in the waveguide. $C_R^\dagger(x)$ and $C_R(x)$ [$C_L^\dagger(x)$ and $C_L(x)$] are the operators that create and annihilate a right (left) moving photon at position x. $a_e^\dagger$ and a_e ($a_g^\dagger$ and a_g) are the creation and annihilation operators of the excited (ground) state of the atom. Thus, $\sigma_+ \equiv a_e^\dagger a_g$ and $\sigma_- \equiv a_g^\dagger a_e$ are the ladder operators that excite and deexcite the atom, respectively. $\hbar\omega_e$ and $\hbar\omega_g$ are the energy levels of the atom in the excited state and the ground state. $\bar{V}$ is the coupling constant between the waveguide and the atom ($\Gamma \equiv 2\bar{V}^2/v$ is the spontaneous emission rate in the waveguide and also characterize the width of the transmission spectrum [64]). Hereafter, the system which is described by such a Hamiltonian is said to be non-chiral, wherein photons can propagate in both directions.

For an N-photon Fock state scattering process in the non-chiral system, a direct attempt to solve for the eigenstates is mathematically complicated, as one has to deal with a plethora of all possible transmitted and reflected states, which involves $2^N N!$ independent parameters to be determined. Instead, to ease the calculation complexity, an efficient strategy is to first solve the n-photon scattering process in the chiral space for $n = 1, 2, \cdots, N$, wherein photons only propagate in one direction. Then, the solutions in the chiral space with different photon numbers n are recombined to construct the solutions in the non-chiral space [87]. To go from the non-chiral Hamiltonian to the chiral ones, we perform the following transformations

$$\begin{aligned} C_e^\dagger(x) &\equiv \frac{1}{\sqrt{2}}[C_R^\dagger(x) + C_L^\dagger(-x)], \\ C_o^\dagger(x) &\equiv \frac{1}{\sqrt{2}}[C_R^\dagger(x) - C_L^\dagger(-x)], \end{aligned} \tag{4.2}$$

to decompose the Hamiltonian into two decoupled even and odd parts ($H = H_e + H_o$):

$$
\begin{aligned}
H_e/\hbar &= \int dx(-i)vC_e^\dagger(x)\frac{\partial}{\partial x}C_e(x) + \int dxV\delta(x)[C_e^\dagger(x)\sigma_- + C_e(x)\sigma_+] + E_e a_e^\dagger a_e + E_g a_g^\dagger a_g, \\
H_o/\hbar &= \int dx(-i)vC_o^\dagger(x)\frac{\partial}{\partial x}C_o(x),
\end{aligned}
\tag{4.3}
$$

where $[H_e, H_o] = 0$. Here, H_o is an interaction-free Hamiltonian, while H_e includes the interaction with an effective coupling strength $V \equiv \sqrt{2}\bar{V}$. The systems described by the Hamiltonians H_e and H_o are referred to as the chiral systems with unidirectional propagation of photons. Mathematically, a complete set of solutions for both chiral systems allows one to solve the scattering problems in the corresponding non-chiral system. Although the chiral systems here described by Eq. 4.3 are for mathematical convenience, there are physical systems which are precisely described by the chiral Hamiltonians, such as the photonic analog of the quantum Hall effect [99, 100]. In those chiral systems, the backscattered modes are completely suppressed. Thus, the chiral systems are anticipated to be robust for structural imperfections and slow light operations. In view of these possibilities, we present the investigations for the chiral systems in the next section.

4.3 The Solutions for the Chiral System

An N-photon eigenstate $|i^+\rangle$ of the chiral system described by H_e is defined in the Hilbert space $\mathcal{H}_e^{\bigotimes N}$, where $\mathcal{H}_e$ is the one-photon Hilbert space. $|i^+\rangle$ has the following general form

$$
\begin{aligned}
|i^+\rangle = &\int\cdots\int dx_1 dx_2\cdots dx_N f(x_1, x_2, \cdots, x_N)\frac{1}{\sqrt{N!}}C_e^\dagger(x_1)C_e^\dagger(x_2)\cdots C_e^\dagger(x_N)|\emptyset, -\rangle \\
&+\int\cdots\int dx_1 dx_2\cdots dx_{N-1} e(x_1, x_2, \cdots, x_{N-1})\frac{1}{\sqrt{(N-1)!}}C_e^\dagger(x_1)C_e^\dagger(x_2)\cdots C_e^\dagger(x_{N-1})\sigma_+|\emptyset, -\rangle,
\end{aligned}
\tag{4.4}
$$

where $|\emptyset, -\rangle$ is the vacuum state with zero photon in the waveguide and the atom in the ground state. The first term corresponds to the situation that the atom is in the ground state and the N photons are in the waveguide described by an N-photon wavefunction $f(x_1, x_2, \cdots, x_N)$. The second term, on the other hand, corresponds to the situation when one of the N photons is absorbed by the atom and the atom is in the excited state. The other $N-1$ photons in the waveguide are described by an $(N-1)$-photon wavefunction $e(x_1, x_2, \cdots, x_{N-1})$. The prefactors $1/\sqrt{N!}$ and $1/\sqrt{(N-1)!}$ are the normalization constants [101]. Due to the bosonic nature of the photons, photonic wavefunctions $f(x_1, x_2, \cdots, x_N)$ and $e(x_1, x_2, \cdots, x_{N-1})$ have the exchange symmetric with respect to the exchange of any two coordinates.

From the Schrödinger equation $H_e|i^+\rangle = E|i^+\rangle$, by equating the coefficients for each basis, we obtain the equations of motion as follows:

$$\left[-iv\frac{\partial}{\partial x_1} - iv\frac{\partial}{\partial x_2} - \cdots - iv\frac{\partial}{\partial x_N} - E/\hbar\right] f(x_1, x_2, \cdots, x_N) + \frac{V}{\sqrt{N}}\left[\delta(x_1)e(x_2, x_3, \cdots, x_N) + \delta(x_2)e(x_1, x_3, \cdots, x_N) + \cdots + \delta(x_N)e(x_1, x_2, \cdots, x_{N-1})\right] = 0, \tag{4.5}$$

$$\left[-iv\frac{\partial}{\partial x_1} - iv\frac{\partial}{\partial x_2} - \cdots - iv\frac{\partial}{\partial x_{N-1}} - (E/\hbar - \Omega)\right] e(x_1, x_2, \cdots, x_{N-1}) + \frac{V}{\sqrt{N}}\left[f(0, x_1, x_2, \cdots, x_{N-1}) + f(x_1, 0, x_2, \cdots, x_{N-1}) + \cdots + f(x_1, x_2, \cdots, x_{N-1}, 0)\right] = 0, \tag{4.6}$$

where $\Omega \equiv \omega_e - \omega_g$ is the transition frequency of the atom. Form Eqs. 4.5 and 4.6, all the possible solutions of $f(x_1, x_2, \cdots, x_N)$ and $e(x_1, x_2, \cdots, x_{N-1})$ can be solved for (see Appendix A), which provide a complete set of eigenstates $\{|i^+\rangle\}$. By using the Lippmann-Schwinger equation [102], the solved set of eigenstates $|i^+\rangle$ can be used to obtain the corresponding in-states

$|\text{in}\rangle$ and out-states $|\text{out}\rangle$:

$$
\begin{aligned}
|\text{in}\rangle &= \int\cdots\int dx_1 dx_2\cdots dx_N f_{\text{in}}(x_1,x_2,\cdots,x_N)\frac{1}{\sqrt{N!}}C_e^\dagger(x_1)C_e^\dagger(x_2)\cdots C_e^\dagger(x_N)|\emptyset,-\rangle,\\
|\text{out}\rangle &= \int\cdots\int dx_1 dx_2\cdots dx_N f_{\text{out}}(x_1,x_2,\cdots,x_N)\frac{1}{\sqrt{N!}}C_e^\dagger(x_1)C_e^\dagger(x_2)\cdots C_e^\dagger(x_N)|\emptyset,-\rangle.
\end{aligned}
\tag{4.7}
$$

The in-state wavefunction $f_{\text{in}}(x_1,x_2,\cdots,x_N)$ is the extension of the eigenstate wavefunction,

$$
f_{\text{in}}(x_1,\cdots,x_N) = f(x_1<0,\cdots,x_N<0). \tag{4.8}
$$

This equation means that the functional form of $f_{\text{in}}(x_1,\cdots,x_N)$ is the same as that of $f(x_1,\cdots,x_N)$ in the restricted region $x_1<0,\cdots,x_N<0$, but is extended in the entire space. Similarly, the out-state wavefunction $f_{\text{out}}(x_1,x_2,\cdots,x_N)$ is the extension of the eigenstate wavefunction:

$$
f_{\text{out}}(x_1,\cdots,x_N) = f(x_1>0,\cdots,x_N>0). \tag{4.9}
$$

Physically, the in-states and the out-states correspond to the states that are long before and after the scattering, respectively. That is to say, for each in-state, there exists a causally related out-state. The in-states and out-states are complete in the in and out spaces. With the full knowledge of the in-states and out-states, one can construct the scattering matrix for any states $\in \mathcal{H}_e^{\bigotimes N}$,

$$
\mathbf{S}_{e^{(N)}} = \sum_{\{|\text{in}\rangle\}} |\text{out}\rangle\langle\text{in}|, \tag{4.10}
$$

which maps a free N-photon Hilbert space of in-states to another free N-photon Hilbert space consisting out-states. The summation is taken over for a complete basis $\{|\text{in}\rangle\}$. Once the scattering matrix is determined, one can calculate the output state of the system for an arbitrary input state when the atom is initially in the ground state.

In the following, we show explicitly the form of the complete set of the in-states for different photon number from $N = 1$ to 4, as well as the general case N.

4.3.1 1-photon Case

For this simplest case, the class of the in-state wavefunctions can be represented by a plane wave,

$$f_{\text{in}}(x) = C_1 e^{ikx}, \tag{4.11}$$

which is characterized by a single real parameter $k = E/(v\hbar) \in \mathbb{R}$. For different k, these waves form a complete set. C_1 is the normalization constant, which can be determined using the normalization condition detailed in appendix B.

4.3.2 2-photon Case

The general form of the class of in-state wavefunctions is

$$f_{\text{in}}(x_1, x_2) = C_2 \left\{ [k_1 - k_2 - i\Gamma \text{sgn}(x_2 - x_1)/v] e^{ik_1 x_1 + ik_2 x_2} + [k_1 - k_2 - i\Gamma \text{sgn}(x_1 - x_2)/v] e^{ik_2 x_1 + ik_1 x_2} \right\}, \tag{4.12}$$

where $\text{sgn}(\cdot)$ is the sign function with $\text{sgn}(x > 0) = 1$ and $\text{sgn}(x < 0) = -1$. $\Gamma = 2\bar{V}^2/v = V^2/v$ is the spontaneous emission rate into the waveguide. k_1 and k_2 are in general two complex numbers subject to the constraint of $k_1 + k_2 = E/(v\hbar) \in \mathbb{R}$, among others. Such a constraint imposes that either both k_1 and k_2 are real (type-1) or their imaginary parts have an opposite sign (type-2). A full analysis shows that in type-2, k_1 and k_2 are in fact complex conjugate to each other (i.e., have the same real part). In general, these two types of in-states exhibit different forms of wavefunctions, thereby requiring different normalization constants (appendix B). Tab. 4.1 summarizes the properties of the two types of in-states.

Table 4.1: 2-photon in-states classifications

Type-1	k_1, k_2 (real numbers)	$(1,1)$
Type-2	$k_1 = k - i\Gamma/(2v)$, $k_2 = k + i\Gamma/(2v)$	(2)

In type-1, both k_1 and k_2 are real, which leads to a 2-photon extended state. In type-2, $k_1 = k - i\Gamma/(2v)$ and $k_2 = k + i\Gamma/(2v)$ so that the wavefunction can be further reduced to

$$f_{\text{in}}(x_1, x_2) = C_2 e^{ik(x_1+x_2)-|x_2-x_1|\Gamma/(2v)}. \tag{4.13}$$

This wavefunction describes a 2-photon bound state, as the wavefunction approaches to zero exponentially when the two photons become afar. It has been shown that these two types of in-states form a complete set in the 2-photon Hilbert space [87]. In the last column of table, we also list all possible partitions of the photon number $N = 2$. The assigning rule is as follows: for unrestricted real number E, if a single variable can specify the values of j k's, a number j is assigned in the column. For the present case, in type-1, k_1 and k_2 need to be independently specified, so this type is assigned $(1,1)$. In type-2, a single variable k can specify the values of both k_1 and k_2 (Γ and v are given constants), thus (2) is assigned in the column.

4.3.3 3-photon Case

The general form of the class of in-state wavefunctions is

$$\begin{aligned}
f_{\text{in}}(x_1,x_2,x_3) = C_3\{&[k_1-k_2-i\Gamma\text{sgn}(x_2-x_1)/v][k_2-k_3-i\Gamma\text{sgn}(x_3-x_2)/v][k_1-k_3-i\Gamma\text{sgn}(x_3-x_1)/v]e^{i(k_1x_1+k_2x_2+k_3x_3)}\\
&+[k_1-k_2-i\Gamma\text{sgn}(x_3-x_1)/v][k_2-k_3-i\Gamma\text{sgn}(x_2-x_3)/v][k_1-k_3-i\Gamma\text{sgn}(x_2-x_1)/v]e^{i(k_1x_1+k_2x_3+k_3x_2)}\\
&+[k_1-k_2-i\Gamma\text{sgn}(x_1-x_2)/v][k_2-k_3-i\Gamma\text{sgn}(x_3-x_1)/v][k_1-k_3-i\Gamma\text{sgn}(x_3-x_2)/v]e^{i(k_1x_2+k_2x_1+k_3x_3)}\\
&+[k_1-k_2-i\Gamma\text{sgn}(x_1-x_3)/v][k_2-k_3-i\Gamma\text{sgn}(x_2-x_1)/v][k_1-k_3-i\Gamma\text{sgn}(x_2-x_3)/v]e^{i(k_1x_3+k_2x_1+k_3x_2)}\\
&+[k_1-k_2-i\Gamma\text{sgn}(x_3-x_2)/v][k_2-k_3-i\Gamma\text{sgn}(x_1-x_3)/v][k_1-k_3-i\Gamma\text{sgn}(x_1-x_2)/v]e^{i(k_1x_2+k_2x_3+k_3x_1)}\\
&+[k_1-k_2-i\Gamma\text{sgn}(x_2-x_3)/v][k_2-k_3-i\Gamma\text{sgn}(x_1-x_2)/v][k_1-k_3-i\Gamma\text{sgn}(x_1-x_3)/v]e^{i(k_1x_3+k_2x_2+k_3x_1)}\},
\end{aligned} \tag{4.14}$$

where k_1, k_2, and k_3 are in general complex numbers subject to the constraint of $k_1+k_2+k_3 = E/(v\hbar)$. In such a 3-photon Hilbert space, there are in total three different types of in-states, illustrated in Tab. 4.2.

Table 4.2: 3-photon in-states classifications

Type-1	k_1, k_2, k_3 (real numbers)	$(1,1,1)$
Type-2	$k_1 = k - i\Gamma/(2v)$, $k_2 = k + i\Gamma/(2v)$, k_3	$(2,1)$
Type-3	$k_1 = k - i\Gamma/v$, $k_2 = k$, $k_3 = k + i\Gamma/v$	(3)

In type-1, k_1, k_2, and k_3 are three independent real numbers, which leads to a 3-photon extended state and is assigned $(1,1,1)$. In type-2, $k_1 = k - i\Gamma/(2v)$ and $k_2 = k + i\Gamma/(2v)$ are complex conjugate to each other, while the third number k_3 is a real number. This type is accordingly assigned $(2,1)$. To gain insights for the mathematical structure of this wavefunction, we focus on a specific region, e.g. $x_1 < x_2 < x_3$, to remove all the sign functions,

$$\begin{aligned} f_{\text{in}}(x_1,x_2,x_3) = C_3\{&[k-k_3-i\Gamma/(2v)]\,[k-k_3-i3\Gamma/(2v)]\,e^{ik(x_1+x_2)+ik_3x_3-(x_2-x_1)\Gamma/(2v)} \\ &+ [k-k_3+i3\Gamma/(2v)]\,[k-k_3-i3\Gamma/(2v)]\,e^{ik(x_1+x_3)+ik_3x_2-(x_3-x_1)\Gamma/(2v)} \\ &+ [k-k_3+i3\Gamma/(2v)]\,[k-k_3+i\Gamma/(2v)]\,e^{ik(x_2+x_3)+ik_3x_1-(x_3-x_2)\Gamma/(2v)}\}. \end{aligned} \tag{4.15}$$

In such a wavefunction, the first term and the third term indicate one 2-photon bound state and one 1-photon extended state. The second term in the wavefunction, however, describes the situation that all three photons are bounded, as the coordinates are in the region of $x_1 < x_2 < x_3$. The wavefunction in the other five regions can be obtained straightforwardly using the exchange symmetry with respect to the coordinates. Finally, in type-3, $k_1 = k - i\Gamma/v$, $k_2 = k$, and $k_3 = k + i\Gamma/v$, and the wavefunction is reduced to

$$f_{\text{in}}(x_1,x_2,x_3) = C_3 e^{ik(x_1+x_2+x_3)-(|x_3-x_1|+|x_2-x_1|+|x_3-x_2|)\Gamma/(2v)}. \tag{4.16}$$

Such a wavefunction describes a 3-photon bound state, as the wavefunction approaches to zero exponentially when any two of the three photons become afar. For all three types of in-states, we develop a computational procedure to check the completeness of these three types of in-states, which is detailed in Appendix C.

4.3.4 4-photon Case

Analogous to the previous case, the complete set of the in-states for $N = 4$ case can be classified into five different types, illustrated in Tab. 4.3.

Table 4.3: 4-photon in-states classifications

Type-1	k_1, k_2, k_3, k_4 (real numbers)	$(1,1,1,1)$
Type-2	$k_1 = k - i\Gamma/(2v)$, $k_2 = k + i\Gamma/(2v)$, k_3 , k_4	$(2,1,1)$
Type-3	$k_1 = k - i\Gamma/(2v)$, $k_2 = k + i\Gamma/(2v)$ $k_3 = k' - i\Gamma/(2v)$, $k_4 = k' + i\Gamma/(2v)$	$(2,2)$
Type-4	$k_1 = k - i\Gamma/v$, $k_2 = k$, $k_3 = k + i\Gamma/v$, k_4	$(3,1)$
Type-5	$k_1 = k - 3i\Gamma/(2v)$, $k_2 = k - i\Gamma/(2v)$, $k_3 = k + i\Gamma/(2v)$, $k_4 = k + 3i\Gamma/(2v)$	(4)

4.3.5 N-photon Case

The general form of the class of in-state wavefunctions is

$$f_{\text{in}}(x_1, x_2, \cdots, x_N) = C_N \sum_{\mathcal{P}\in S_N} \left\{ \prod_{m<n} [k_m - k_n - i\Gamma \text{sgn}(x_{\mathcal{P}_n} - x_{\mathcal{P}_m})/v] \right\} \exp(i \sum_{j=1}^{N} k_j x_{\mathcal{P}_j}), \tag{4.17}$$

where S_N is the symmetric group on an N-element set $\{1, 2, \cdots, N\}$, and the summation $\mathcal{P} \in S_N$ accounts for all the $N!$ permutations of the labels $\{1, 2, \cdots, N\}$. k_1, k_2, $\cdots$, and k_N are in general N complex numbers subject to the constraint of $k_1 + k_2 + \cdots + k_N = E/(v\hbar)$. We note that Eq. 4.17 satisfies the form of Bethe ansatz [103]. In the N-photon Hilbert

space, the total number of the types of the in-states is exactly the partition function $Z(N)$ for an integer number N. The first 10 values of $Z(N)$ is $1, 2, 3, 5, 7, 11, 15, 22, 30, 42, \cdots$. For large values of N, $Z(N)$ increases exponentially with an asymptotic behavior given by [104]

$$Z(N) \sim \frac{1}{4N\sqrt{3}} e^{\pi\sqrt{2N/3}}. \tag{4.18}$$

Tab. 4.4 classifies all types of in-states for N-photon case. We note that all the values of k's in each type are in agreement with that obtained using the Bethe anstaz approach [85].

Table 4.4: N-photon in-states classifications

Type-1	$k_1, \cdots, k_N$ (real numbers)	$(1, 1, \cdots, 1, 1)$
Type-2	$k_1 = k - i\Gamma/(2v)$, $k_2 = k + i\Gamma/(2v)$, $k_3, \cdots, k_N$	$(2, 1, \cdots, 1)$
$\cdots$	$\cdots$	$\cdots$
Type-$Z(N)$	$k_1 = k - i(N-1)\Gamma/(2v)$, $k_2 = k - i(N-3)\Gamma/(2v)$, $\vdots$ $k_{N-1} = k + i(N-3)\Gamma/(2v)$, $k_N = k + i(N-1)\Gamma/(2v)$	(N)

In type-1, all the k_1, k_2, $\cdots$, and k_N are real numbers, which leads to an N-photon extended state and is assigned $(1, 1, \cdots, 1, 1)$. In type-2, $k_1 = k - i\Gamma/(2v)$ and $k_2 = k + i\Gamma/(2v)$ are complex conjugate to each other, while the remaining $N-2$ k's are independent real variables. For simplicity, we focus on a specific region $x_1 < x_2 < \cdots < x_N$ to remove all the sign functions. A direct substitution of the k's into Eq. 4.17 reveals that half of terms in the wavefunction vanish as their coefficients become zero, and only half of terms remain. Among the remaining terms, for coordinates x_l and x_m $(l < m)$ paired with the two complex conjugate $k_1 = k - i\Gamma/(2v)$ and $k_2 = k + i\Gamma/(2v)$, such term would give rise to a form of $e^{-(x_m - x_l)\Gamma/(2v)}$. As $x_1 < x_2 < \cdots < x_N$, the $m-l+1$ photons with coordinates $x_l, \cdots, x_m$ form an $(m-l+1)$-photon bound state. The rest of $(N-m+l-1)$ photons form an $(N-m+l-1)$-photon extended state. The type-$Z(N)$ has N complex k's: $k_j = k + [2j - (N+1)]\Gamma/(2v)$,

$j = 1, 2, \cdots, N$. By substituting them into Eq. 4.17, the wavefunction is reduced to

$$f_{\text{in}}(x_1, x_2, \cdots, x_N) = C_N e^{ik(x_1+x_2+\cdots+x_N)-(\sum_{m<n}|x_m-x_n|)\Gamma/(2v)}, \tag{4.19}$$

which only contains one term, describing an N-photon bound state, as the wavefunction approaches zero exponentially when any two of the N photons become afar.

4.3.6 Out-state Wavefunction

Having introduced all possible in-state wavefunctions, the out-state wavefunctions can be expressed by multiplying an N-photon transmission amplitude to the in-state wavefunctions (see appendix A):

$$f_{\text{out}}(x_1, x_2, \cdots, x_N) = T(k_1, k_2, \cdots, k_N) f_{\text{in}}(x_1, x_2, \cdots, x_N), \tag{4.20}$$

where

$$T(k_1, k_2, \cdots, k_N) = \prod_{k_j} t_{k_j}, \tag{4.21}$$

and

$$t_{k_j} \equiv \frac{k_j - \Omega/v - i\Gamma/(2v)}{k_j - \Omega/v + i\Gamma/(2v)} \tag{4.22}$$

is the single-photon transmission amplitude in the chiral system with absolute value equals to one. With all the in-states and out-states, the scattering matrix for Hamiltonian H_e is formed using the definition in Eq. 4.10. The scattering matrix for Hamiltonian H_o, on the other hand, is simply an identity matrix.

4.4 The Scattering Matrix for Non-chiral System

Having solved the scattering problems for the chiral case, we now compute the scattered photon states for the non-chiral systems, wherein the photons can propagate in both direction. For the non-chiral case, a typical input Fock state $|X_{\rm in}\rangle$ that containing N right-moving photons can be written as

$$\begin{aligned}
|X_{\rm in}\rangle &= \int\cdots\int dx_1dx_2\cdots dx_N h(x_1,x_2,\cdots,x_N)\frac{1}{\sqrt{N!}}C_R^\dagger(x_1)C_R^\dagger(x_2)\cdots C_R^\dagger(x_N)|\emptyset,-\rangle,\\
&= \int\cdots\int dx_1dx_2\cdots dx_N h(x_1,x_2,\cdots,x_N)\frac{1}{\sqrt{N!}}(\frac{1}{\sqrt{2}})^N[C_e^\dagger(x_1)+C_o^\dagger(x_1)]\cdots[C_e^\dagger(x_N)+C_o^\dagger(x_N)]|\emptyset,-\rangle,\\
&= \int\cdots\int dx_1dx_2\cdots dx_N h(x_1,x_2,\cdots,x_N)\frac{1}{\sqrt{N!}}(\frac{1}{\sqrt{2}})^N C_e^\dagger(x_1)\cdots C_e^\dagger(x_N)|\emptyset,-\rangle+\cdots\\
&+ \int\cdots\int dx_1dx_2\cdots dx_N h(x_1,x_2,\cdots,x_N)\frac{1}{\sqrt{N!}}(\frac{1}{\sqrt{2}})^N C_o^\dagger(x_1)\cdots C_o^\dagger(x_N)|\emptyset,-\rangle,
\end{aligned} \tag{4.23}$$

here, $h(x_1,x_2,\cdots,x_N)$ is the N-photon wavefunction. In the second equality, we have used the inverse relation of Eq. 4.2. For an input Fock state that containing N left-moving photons, the process will proceed similarly. In the last equality, the direct expansion gives rise to 2^N terms. Since $C_e^\dagger(x)$ and $C_o^\dagger(x)$ commute, using the exchange symmetry with respect to the coordinates in the wavefunction, these 2^N terms can be grouped into $N+1$ orthogonal terms. Thus, $|X_{\rm in}\rangle$ can be written as a linear superposition of $N+1$ chiral spaces.

$$|X_{\rm in}\rangle = |X_{\rm in}\rangle_{e^{(N)}} + |X_{\rm in}\rangle_{e^{(N-1)}o^{(1)}} + \cdots + |X_{\rm in}\rangle_{o^{(N)}}. \tag{4.24}$$

Here, $|X_{\rm in}\rangle_{e^{(j)}o^{(N-j)}}$ is given by

$$|X_{\rm in}\rangle_{e^{(j)}o^{(N-j)}} = \int\cdots\int dx_1dx_2\cdots dx_N h(x_1,x_2,\cdots,x_N)\frac{1}{\sqrt{N!}}(\frac{1}{\sqrt{2}})^N\frac{N!}{j!(N-j!)}C_e^\dagger(x_1)\cdots C_e^\dagger(x_j)C_o^\dagger(x_{j+1})\cdots C_o^\dagger(x_N)|\emptyset,-\rangle, \tag{4.25}$$

which describes a state in the $e^{(j)}o^{(N-j)}$ space where j photons are in the even mode and $N-j$ photons are in the odd mode. Consequently, the scattering matrix $\mathbf{S}$ in the non-chiral

case can be decomposed accordingly,

$$\mathbf{S} = \sum_{j=0}^{N} \mathbf{S}_{e^{(j)}} \bigotimes \mathbf{S}_{o^{(N-j)}}, \tag{4.26}$$

where $\mathbf{S}_{e^{(j)}}$ and $\mathbf{S}_{o^{(j)}}$ are the scattering matrices for states in $\mathcal{H}_e^{\otimes j}$ and $\mathcal{H}_o^{\otimes j}$, respectively. By applying the scattering matrix onto the input state (Eq. 4.24), one can directly compute the scattered states term by term in each mutually orthogonal subspace,

$$\begin{aligned} |X_{\text{out}}\rangle &\equiv \mathbf{S}|X_{\text{in}}\rangle \\ &= \mathbf{S}_{e^{(N)}}|X_{\text{in}}\rangle_{e^{(N)}} + \mathbf{S}_{e^{(N-1)}} \bigotimes \mathbf{S}_{o^{(1)}}|X_{\text{in}}\rangle_{e^{(N-1)}o^{(1)}} + \cdots + \mathbf{S}_{o^{(N)}}|X_{\text{in}}\rangle_{o^{(N)}} \\ &\equiv |X_{\text{out}}\rangle_{e^{(N)}} + |X_{\text{out}}\rangle_{e^{(N-1)}o^{(1)}} + \cdots + |X_{\text{out}}\rangle_{o^{(N)}}. \end{aligned} \tag{4.27}$$

In the above calculations, the scattering matrices only apply to the states with the same subscripts. Using Eq. 4.2, each state can be transformed back into the original non-chiral system in terms of right- and left-moving photons,

$$|X_{\text{out}}\rangle = |X_{\text{out}}\rangle_{R^{(N)}} + |X_{\text{out}}\rangle_{R^{(N-1)}L^{(1)}} + \cdots + |X_{\text{out}}\rangle_{L^{(N)}}. \tag{4.28}$$

Here, $|X_{\text{out}}\rangle_{R^{(j)}L^{(N-j)}}$ describes the scattered photon state in the $R^{(j)}L^{(N-j)}$ space where j photons propagate to the right (i.e., transmitted) and $N-j$ photons propagate to the left (reflected). Such a procedure facilitates the calculations by allocating the scattering processes into decoupled chiral systems, each of which involves less computational complexity. In the following, we demonstrate this computational scheme by calculating the scattered photon state for a 3-photon Fock state.

4.5 Example: the Scattering of 3-photon Fock States in Non-chiral Systems

4.5.1 The Scattered Photon Wavefunctions

Having introduced the general approach to solve the scattering problems in the non-chiral space, we now calculate the scattered photon states for a concrete example. Consider an input state of a 3-photon Fock state, formed by three overlapping photons, wherein each photon is represented by a Gaussian wave packet. Such a state is a product state which has no correlations. Each photon is on resonant with the atom and has a broad extension in the real space so that the bandwidth is narrow. The single-photon wavefunction is

$$\phi_i(x) = (2\pi\sigma_x^2)^{-1/4} e^{-x^2/4\sigma_x^2} e^{i(\Omega/v)x}. \tag{4.29}$$

Here, $|\phi_i(x)|^2$ is normalized to unity when integrated over x from $-\infty$ to $+\infty$. The standard deviation $\sigma_x = 10v\tau_r$ and $\sigma_\omega = 0.2\Gamma$ ($\tau_r = 1/\Gamma$ is the radiation lifetime for the spontaneous emission). After scattering, the 3-photon Hilbert space is decomposed into four orthogonal spaces: $R^{(3)}$, $R^{(2)}L^{(1)}$, $R^{(1)}L^{(2)}$, and $L^{(3)}$. A direct calculation using the computational scheme presented above reveals that all three photons are most likely to be reflected into the $L^{(3)}$ space, with a probability $P_{L^{(3)}} \equiv \int\int\int dx_1 dx_2 dx_3 |\langle x_1, x_2, x_3 | X_{\text{out}} \rangle_{L^{(3)}}|^2 \approx 55\%$; while the probability that all three photons are transmitted into the $R^{(3)}$ space is the least: $P_{R^{(3)}} \equiv \int\int\int dx_1 dx_2 dx_3 |\langle x_1, x_2, x_3 | X_{\text{out}} \rangle_{R^{(3)}}|^2 \approx 2\%$. The remaining probability is distributed within the other two possibilities with $P_{R^{(2)}L^{(1)}} \approx 13\%$ and $P_{R^{(1)}L^{(2)}} \approx 29\%$. Such a probability distribution is completely beyond the single-photon picture; for a single photon with the same Gaussian wavefunction form, it is numerically found that the photon is essentially completely reflected with a reflectivity over 99% and a transmissivity less than 1% [64]. Thus, based upon the single-photon picture, *if there is no correlations induced by the atom*,

one would have expected $P_{L^{(3)}} > (99\%)^3 \approx 97\%$ and $P_{R^{(3)}} < (1\%)^3 = 10^{-6}$. Thus, for the 3-photon case, $P_{R^{(3)}}$ is greatly enhanced by the correlations. Such an example demonstrates that the dynamics in the multiple photon scattering processes are dramatically influenced by the correlations induced by the atom. Thus, it is of great interest to understand how the three photons get transmitted in the presence of the atom-induced correlations. For this purpose, we numerically checked the transmitted 3-photon wavefunction in the $R^{(3)}$ space, which can be expressed as:

$$h_{R^{(3)}}(x_1, x_2, x_3) = \frac{1}{8}[h_{e^{(3)}}(x_1, x_2, x_3) + h_{e^{(2)}o^{(1)}}(x_1, x_2, x_3) + h_{e^{(1)}o^{(2)}}(x_1, x_2, x_3) + h_{o^{(3)}}(x_1, x_2, x_3)]. \tag{4.30}$$

Here the functions $h_{e^{(3)}}(x_1, x_2, x_3)$, $h_{e^{(2)}o^{(1)}}(x_1, x_2, x_3)$, $h_{e^{(1)}o^{(2)}}(x_1, x_2, x_3)$, and $h_{o^{(3)}}(x_1, x_2, x_3)$ are the scattered wavefunctions in the $e^{(3)}$, $e^{(2)}o^{(1)}$, $e^{(1)}o^{(2)}$, and $o^{(3)}$ subspaces, respectively.

It is numerically found that the non-chiral wavefunction $h_{R^{(3)}}(x_1, x_2, x_3)$ is essentially due to the chiral wavefunction of the 3-photon bound state in $h_{e^{(3)}}(x_1, x_2, x_3)$. We emphasize that $h_{e^{(3)}}(x_1, x_2, x_3)$ also contains components other than the 3-photon bound state. Specifically, it is the second term in the type-2 wavefunction, and the type-3 wavefunction that contribute to $h_{R^{(3)}}(x_1, x_2, x_3)$ (see section 3). In contrast, wavefunctions $h_{e^{(2)}o^{(1)}}$, $h_{e^{(1)}o^{(2)}}$, $h_{o^{(3)}}$, and the rest parts in wavefunctions $h_{e^{(3)}}(x_1, x_2, x_3)$ numerically cancel out with each other, thus do not contribute to the 3-photon transmitted wavefunction $h_{R^{(3)}}(x_1, x_2, x_3)$. Therefore, we conclude that the incoming three photons, which can not pass through the atom individually, now are able to pass through the atom as a whole by forming a 3-photon bound state.

We now look into the wavefunctions in more details. To facilitate the visualization of a wavefunction that contains three spatial coordinates, we transform the wavefunction in terms of the relative coordinates as follows:

$$h_r(x_1 - x_3, x_2 - x_3, x_3) \equiv \langle x_1 - x_3, x_2 - x_3, x_3 | X \rangle, \tag{4.31}$$

where $|X\rangle$ is an arbitrary 3-photon state and the subscript 'r' denotes the relative coordinates $(\Delta_1, \Delta_2, x_3) \equiv (x_1 - x_3, x_2 - x_3, x_3)$. Such a transformation has a Jacobian $J = 1$, and maintains the exchange symmetry of the photonic wavefunction. As the transformed wavefunction still contains three variables, we eliminate x_3 by integrating the probability density function as follows:

$$\begin{aligned} \int dx_3 |h_r(x_1 - x_3, x_2 - x_3, x_3)|^2 &\equiv \int dx_3 |h_r(\Delta_1, \Delta_2, x_3)|^2, \\ &\equiv p(\Delta_1, \Delta_2). \end{aligned} \tag{4.32}$$

The relative probability density function $p(\Delta_1, \Delta_2)$ describes the probability density of finding two photons from the viewpoint of the third one. This function also exhibits two interesting symmetries. Firstly, by exchanging the coordinates x_1 and x_2 in the photonic wavefunction h_r, one can immediately see that the function $p(\Delta_1, \Delta_2)$ is symmetric along the line $\Delta_1 = \Delta_2$, i.e.,

$$p(\Delta_1, \Delta_2) = p(\Delta_2, \Delta_1). \tag{4.33}$$

Secondly, $p(\Delta_1, \Delta_2)$ also exhibits inversion symmetry with respect to the origin of the coordinate system, $p(\Delta_1, \Delta_2) = p(-\Delta_1, -\Delta_2)$. The proof is straightforward:

$$\begin{aligned} p(\Delta_1, \Delta_2) &\equiv \int_{-\infty}^{+\infty} dx_3 |h_r(\Delta_1, \Delta_2, x_3)|^2, \\ &= \int_{-\infty}^{+\infty} dx_3 |h_r(x_1 - x_3, x_2 - x_3, x_3)|^2, \\ &= \int_{+\infty}^{-\infty} (-dx_3) |h_r\left[(-x_1) - (-x_3), (-x_2) - (-x_3), (-x_3)\right]|^2, \\ &= \int_{+\infty}^{-\infty} (-dx_3) |h_r(x_3 - x_1, x_3 - x_2, -x_3)|^2, \\ &= \int_{+\infty}^{-\infty} (-dx_3) |h_r(-\Delta_1, -\Delta_2, -x_3)|^2, \\ &= \int_{-\infty}^{+\infty} dx_3 |h_r(-\Delta_1, -\Delta_2, x_3)|^2, \\ &= p(-\Delta_1, -\Delta_2). \end{aligned} \tag{4.34}$$

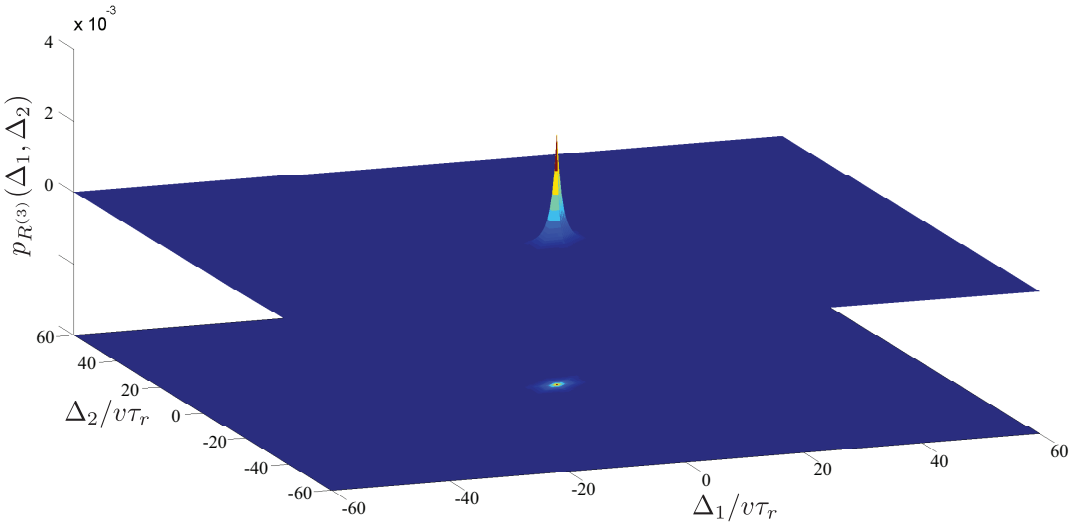

Figure 4.2: Relative probability density function $p_{R^{(3)}}(\Delta_1, \Delta_2)$ for the scattered photon states in the $R^{(3)}$ space (all three photons are transmitted and propagate to the right). A projection of the pattern is also plotted underneath to aid visualization.

Now, we plot the relative probability density function $p_{R^{(3)}}$ and $p_{L^{(3)}}$ in the $R^{(3)}$ space and the $L^{(3)}$ space, respectively. Fig. 4.2 plots $p_{R^{(3)}}(\Delta_1, \Delta_2)$ for the scattered 3-photon state in the $R^{(3)}$ space. A pronounced single narrow peak at $\Delta_1 = \Delta_2 = 0$ clearly emerges with a full width at half maximum (FWHM) $\approx 1.2v\tau_r$. Thus, we have $p_{R^{(3)}}(0, \Delta_2) > p_{R^{(3)}}(\Delta_1, \Delta_2)$ for all $\Delta_1 \neq 0$. The emergence of the center peak indicates photonic bunching, as the probability of finding three photons together is significantly larger than the probability of finding them apart. Mathematically, $p_{R^{(3)}}(\Delta_1, \Delta_2)$ is related to the second-order correlation function as follows (the relation can be derived by using Eq. D.12 and Eq. 4.32),

$$g^{(2)}(\tau) = \frac{2}{3} P_{R^{(3)}} \frac{\int d\Delta_2 p_{R^{(3)}}(v\tau, \Delta_2)}{\int dx_0 |\phi_{R^{(3)}}(x_0)|^2 |\phi_{R^{(3)}}(x_0 + v\tau)|^2}. \tag{4.35}$$

Here, x_0 is the position of the detector, and $\phi_{R^{(3)}}(x)$ is the probability of finding a single photon at position x in the scattered state in $R^{(3)}$ space regardless of the position of the other two photons (see Eq. D.8). Numerically, it is found that $\phi_{R^{(3)}}(x)$ has a similar broad extension as that of $\phi_i(x)$. τ is the difference in the arrival times between two photons. Thus,

when τ is several times of τ_r, the numerator of $g^{(2)}(\tau)$ is much smaller than the numerator of $g^{(2)}(0)$ due to the pronounced peak at the center; while the denominators of $g^{(2)}(\tau)$ and $g^{(2)}(0)$ are numerically found be roughly the same. Therefore, it is numerically found that $g^{(2)}(0) > g^{(2)}(\tau)$, confirming the photonic bunching [105].

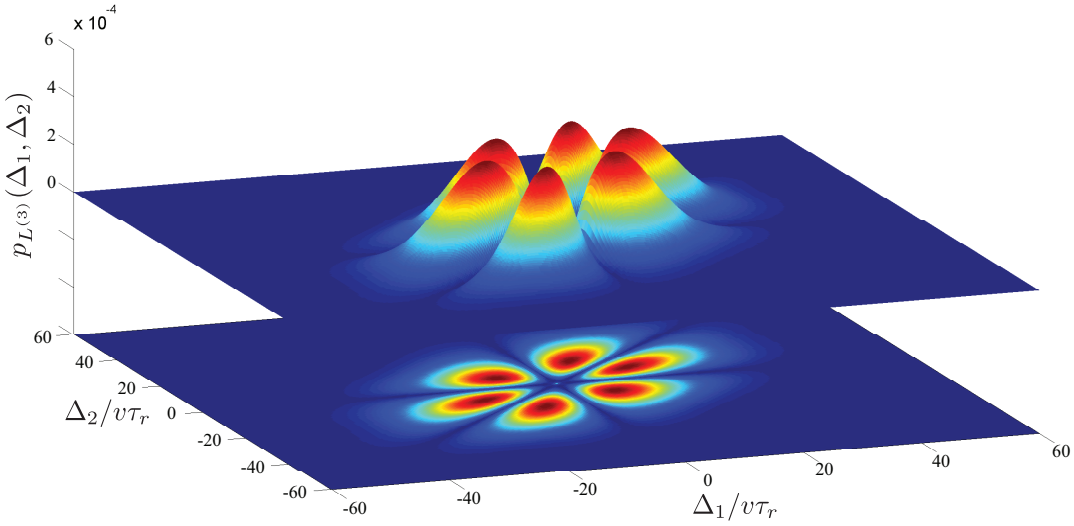

Figure 4.3: Relative probability density function $p_{L^{(3)}}(\Delta_1, \Delta_2)$ for the scattered wavefunction in the $L^{(3)}$ space (all three photons get reflected and propagate to the left). A projection of the pattern is also plotted underneath to aid visualization.

On the other hand, the photon statistics for the reflected photons is fundamentally different in the $L^{(3)}$ space. Fig. 4.3 plots $p_{L^{(3)}}(\Delta_1, \Delta_2)$ for the scattered 3-photon photon state in the $L^{(3)}$ space, which shows six broad peaks separated by three boundaries ($\Delta_1 = 0$, $\Delta_2 = 0$, and $\Delta_1 = \Delta_2$), respectively. The relative probability function is essentially depleted along the boundaries, signaling the photonic anti-bunching, as the probability of finding any two photons together ($\Delta_1 = 0$, $\Delta_2 = 0$, or $\Delta_1 = \Delta_2$) is significantly smaller than the probability of finding them apart ($\Delta_1 \neq 0$, $\Delta_2 \neq 0$, and $\Delta_1 \neq \Delta_2$). Mathematically, such an observation can be rigorously confirmed by directly computing the second-order correlation function for the scattered photon state in the $L^{(3)}$ space. The $g^{(2)}(\tau)$ can be similarly expressed in terms

of the relative probability density function, as follows (see Eq. D.12 and Eq. 4.32),

$$g^{(2)}(\tau) = \frac{2}{3} P_{L^{(3)}} \frac{\int d\Delta_2 p_{L^{(3)}}(v\tau, \Delta_2)}{\int dx_0 |\phi_{L^{(3)}}(x_0)|^2 |\phi_{L^{(3)}}(x_0 + v\tau)|^2}, \tag{4.36}$$

where $\phi_{L^{(3)}}(x)$ is the probability of finding a single photon at position x in the scattered state in the $L^{(3)}$ space regardless of the position of the other two photons, which has a similar broad extension of $\phi_i(x)$. By comparing $g^{(2)}(0)$ and $g^{(2)}(\tau)$, the prior one has a much smaller numerator and their denominators are roughly the same. Thus $g^{(2)}(0) < g^{(2)}(\tau)$, confirming photonic anti-bunching. Such a non-classical phenomenon is in contrast to the bunching effects for the transmission field. Moreover, the photonic bunching and anti-bunching are also manifest in the states in other orthogonal spaces. For example, the two right moving photons in the state that belongs to the $R^{(2)}L^{(1)}$ space exhibit bunching behavior, while the two left moving photons in the state that belongs to $R^{(1)}L^{(2)}$ space exhibit anti-bunching behavior. We note here that the anti-bunching behavior has also been discussed in Ref. [106, 107] when the two-level atom is driven by a weak classical driving field.

4.5.2 Third-order Correlation Function

From the wavefunctions of the scattered 3-photon state, the third-order correlation function in each subspace can be computed (Appendix D). For example, the third-order correlation function for the scattered photon wavefunction in the $L^{(3)}$ space is

$$g^{(3)}(\tau_1, \tau_2) = \frac{2}{9} P^2_{L^{(3)}} \frac{\int dx_0 |h_{L^{(3)}}(x_0, x_0 + v\tau_1, x_0 + v\tau_2)|^2}{\int dx_0 |\phi_{L^{(3)}}(x_0)|^2 ||\phi_{L^{(3)}}(x_0 + v\tau_1)|^2 ||\phi_{L^{(3)}}(x_0 + v\tau_2)|^2|}, \tag{4.37}$$

which is plotted in Fig. 4.4. At the origin of the figure, $g^{(3)}(0,0)$ is numerically found to 0.09. We found that this value could be further suppressed when the grid spacing is decreased at the expense of computational resources. moreover, three lines $\tau_1 = 0$, $\tau_2 = 0$, and $\tau_1 = \tau_2$ separate $g^{(3)}(\tau_1, \tau_2)$ into six regions. The values on the three lines are numerically found to be essentially zero. We also note that the numerator of the third-order correlation function

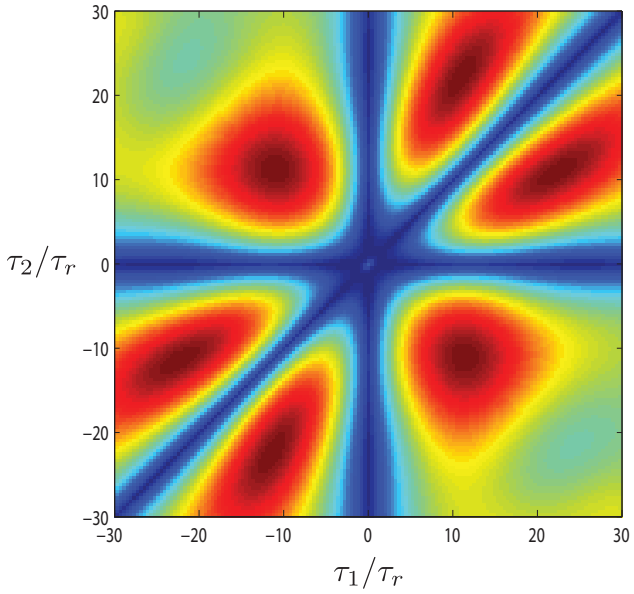

Figure 4.4: Third-order correlation function for the scattered photon wavefunction in $L^{(3)}$ space.

(Eq. 4.37) has the same functional form as the relative probability density function (Eq. 4.32). Thus, Fig. 4.4 looks qualitatively the same as that of the projection in Fig. 4.3. Moreover, second-order correlation function can also be inferred from the third-order correlation as follows (the relation can be derived using Eq. D.10 and Eq. D.11),

$$g^{(2)}(\tau) = \frac{3}{P_{L^{(3)}}} \int dx_3 g^{(3)}(\tau, \frac{x_3 - x_0}{v}) |\phi_{L^{(3)}}(x_3)|^2. \tag{4.38}$$

Since $g^{(3)}(0, \tau_2) \approx 0$ essentially holds for almost all τ_2, $g^{(2)}(0) \approx 0$ is obtained. On the other hand, third-order correlation function for the scattered photon wavefunction in the $R^{(3)}$ space can also be plotted, and a bright spot is observed in the origin. Such a pattern looks qualitative the same as that of the projection in Fig. 4.2, and will not be duplicated here. The third-order correlation functions for the wavefunctions in $R^{(2)}L^{(1)}$ and $R^{(1)}L^{(2)}$ spaces are zero, as a fixed detector can never register three photons in the current setup.

4.6 Summary and Expectation

In this Chapter, we presented a comprehensive study on the analytic approach to solve the multi-photon scattering problems in a waveguide QED system. The fermionic degree of freedom due to the atom induces photon-photon correlations through scattering processes. These photon correlations significantly modify the photon transport properties, which are completely out of the scope of the single-photon picture. For example, after the uncorrelated photonic Fock state scattered by the atom, the transmitted photons, due to the induced correlations, now are bunched, while the reflected photons are anti-bunched. Moreover, the capability of computing the scattering processes for input Fock states with arbitrary number of photons enables one to compute the scattered state for an input coherent state. In principle, one can decompose the coherent state into a linear superposition of all possible Fock state with photon number $N = 1, 2, 3, \cdots$. Then, the scattered photon states for all the Fock states can be computed individually. After that, all the computed scattered states are recombined to obtain the scattered state for the input coherent state. Such a possibility can be practical implemented when the mean photon number is small.

The above procedures can be further generalized to the cases when the incident photons are in the superposition state, i.e., entangled or even involving photons incident from both sides of the atom. For each case, one needs to employ appropriate input state by using corresponding operators in the first row of Eq. 4.23. The rest steps including the construction of the $\mathbf{S}$ matrix remain the same.

Chapter 5

Deep Subwavelength Optical Imaging

5.1 Introduction

Investigations of nanophotonic systems also give us the capability to achieve deep subwavelength optical imaging. Deep subwavelength optical imaging, i.e., which is the capability to discern details much smaller than the wavelength of the illuminating light, will have a strong impact in the life science and in a broad range of next-generation scientific and industrial applications. State-of-the-art approaches to beat the diffraction limit in optical imaging include using (1) artificially engineered materials (e.g., superlens [108] and hyperlens [109]); and (2) fluorescent markers, such as photo-activated localization microscopy (PALM) [110] and stochastic optical reconstruction microscopy (STORM) [111]. Despite demonstrated superior performance, the implementations of these sophisticated techniques face fundamental challenges [112], including material losses and as yet unattainable fabrication finesse, or only work for a narrow class of samples, such as intensely luminescent [113, 114] or sparse objects [115]. Another approach to achieve deep subwavelength resolution is the near-field scanning optical microscopy (NSOM) [116, 117]. Still, NSOM suffers from low transmissivity of optical signals, as the apertures are far smaller than the incident light wavelength. In practice, even with the enormous advances brought about by electron and scanning probe

microscopy, about 80% of all microscopy investigations in the life sciences are still carried out optically [118]. It is thus highly desirable to develop a robust optical imaging technique that overcomes at least some of the limitations in the current approaches.

In this Chapter, we propose a conceptually new, ultra-high resolution, high-throughput, and non-destructive optical lens based on artificially engineered materials for optical imaging that beats the resolution limit of conventional optical instruments and of the recently demonstrated superlens and hyperlens. The key enabling mechanism to achieve ultra-high resolution is to create an array of correlated nano-torches (CNT) to light up the surrounding sample: each light torch has a linear dimension that is far smaller than the wavelength, and contains strong evanescent fields that greatly enhance the light-matter interactions. In such a mechanism, the resolution is primarily determined by the size of the torch, rather than the wavelength of the illuminating light. Moreover, the brightness of each torch depends on the light-matter interactions occurred at its neighboring torches. The correlations between the torches enable the differentiation of contributions from the scattering and absorption of the signal, thereby allow the determination for the *complex* refractive index of the sample. The mechanism is also potentially scalable to be used at different illuminating wavelengths, so long as the criteria of correlated nano-torches are satisfied. To demonstrate the superior performance, we show numerically that the CNT-lens can achieve a resolution of $\lambda/50$ ($\sim 40\,\text{nm}$ at $\lambda = 2.08\,\mu\text{m}$), and has an extraordinarily large signal throughput, even in the presence of material losses. We further show that near-field information can be encoded into propagating waves by coupling the CNT-lens to a passive waveguide. Owing to the large electric field enhancement, the CNT-lens provides a large contrast-to-noise ratio (CNR), and thus is robust to external noises.

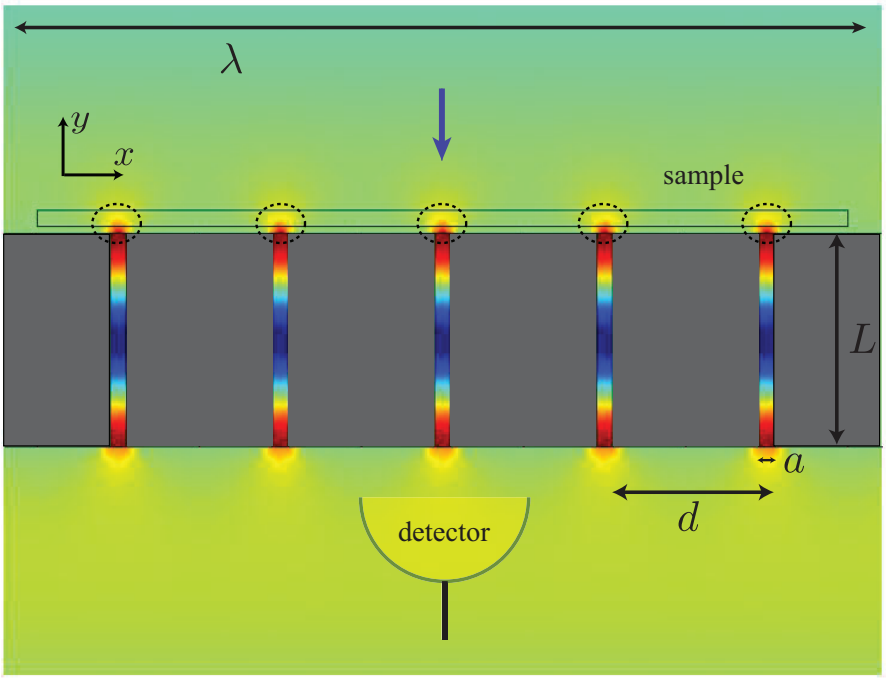

Figure 5.1: Schematic of the CNT-lens. The dashed circles denote the bright nano-torches. The downward blue arrow indicates the direction of the incoming light. The background color indicates the x-component of the electric field profile for a TE incoming plane wave.

5.2 Schematics of the CNT-lens

The simplest realization of the CNT-lens is an one-dimensional subwavelength metallic grating (Fig. 5.1). The CNT-lens is made of a metallic thin film with periodic cut-through slits, which can be either empty or filled with transparent dielectric materials. The slit width a and the grating periodicity d are in the subwavelength regime, i.e. $a < d < \lambda$. It has been shown both theoretically [7] and experimentally [119] that the CNT-lens exhibits artificial dielectric behaviors, and can be precisely mapped into a homogenous dielectric slab, showing a Fabry-Perot transmission spectrum. The CNT-lens permits a large signal throughput for a TE incoming wave (transverse electric field pointing in the x-direction) at resonant frequencies, which could increase the signal-to-noise ratio (SNR) for noises with fixed power level. The extraordinary transmission is due to the subwavelength periodic structure, and can not be achieved by using only a single slit. Moreover, the electric fields in the slits

are greatly enhanced (the enhancement factor is d/a for perfect electric conductor [7]), and strong evanescent torches are formed at both ends of each slit, which enhance the light-matter interactions (Fig. 5.1). In the following, we show that the lateral resolution of the image is determined by the torch size, which can be one or two orders of magnitude smaller than the wavelength. The size of each torch in the x-direction is defined as the full width at half maximum (FWHM) of the electric field; numerically it is found to be on the same order of the slit width.

5.3 Imaging Processes

Here, we describe several steps in the imaging processes in details, including the system setup, data acquisition, and reconstruction algorithm, as follows.

5.3.1 System Setup

A sample is placed on the same side of the illuminating light to interact with the evanescent torches (Fig. 5.1). On the other side of the CNT-lens, a detector is placed in the proximity of one slit (detection slit) to measure from the slit the output optical flux (thus the field strength). One important feature of the CNT-lens is that the slits are coupled, so that when one slit is covered by the sample, the field strengths in its neighboring slits are modified accordingly. Consequently, each measurement includes the information of the local optical properties of every periodic part of the sample that covers the slits at the same time.

5.3.2 Data acquisition

Consider a long sample with an unknown refractive index profile $n(x)$ which is to be determined. $n(x)$ is assumed to be real for now. The following procedures determine $n(x)$ over a continuous segment with length Nd, where N is an arbitrary integer. The refractive index of the sample beyond the segment is assumed to be uniform n_b.

(i) Select a step size δ, which also specifies the pixel size in the reconstructed image. The imaging resolution is given by $\max\{a, \delta\}$.

(ii) Divide the segment into $N\Delta$ slices, where $\Delta = d/\delta$. Without losing generality, here we assume $\delta = a$, and the CNT-lens is designed such that d/a is an integer. The index of each slice is taken as uniform and is denoted by $n_i, i = 1, 2, \cdots, N\Delta$, from right to left.

(iii) Start with $i = 1$ slice covering the detection slit, and record the measurement E_1. Note that the other slits are covered by the recurrent slices labeled by $i = 1 + \Delta, 1 + 2\Delta, \cdots, 1 + (N-1)\Delta$. The set of the slices is collectively denoted by S_1.

(iv) Shift the sample by δ in the x-direction, so that now $i = 2$ slice covers the detection slit. Record the measurement E_2. Now the other slits are covered by the recurrent slices labeled by $i = 2 + \Delta, 2 + 2\Delta, \cdots, 2 + (N-1)\Delta$. The set of the slices is collectively denoted by S_2. S_1 and S_2 are exclusive. Fig. 5.2 depicts the configurations for the slices comprising a general set S_j.

(v) Repeat the shift till $i = N\Delta$ slice covers the detection slit, and record the measurement $E_{N\Delta}$. These $N\Delta$ measurements $\{E_1, E_2, \cdots, E_{N\Delta}\}$ can be partitioned into Δ groups, according to the slice set $S_j, j = 1, 2, \cdots, \Delta$. Each group contains N measurements.

To extract the global information of the sample, we develop a highly efficient and accurate inverse differential algorithm to reconstruct the image from the measurements as follows.

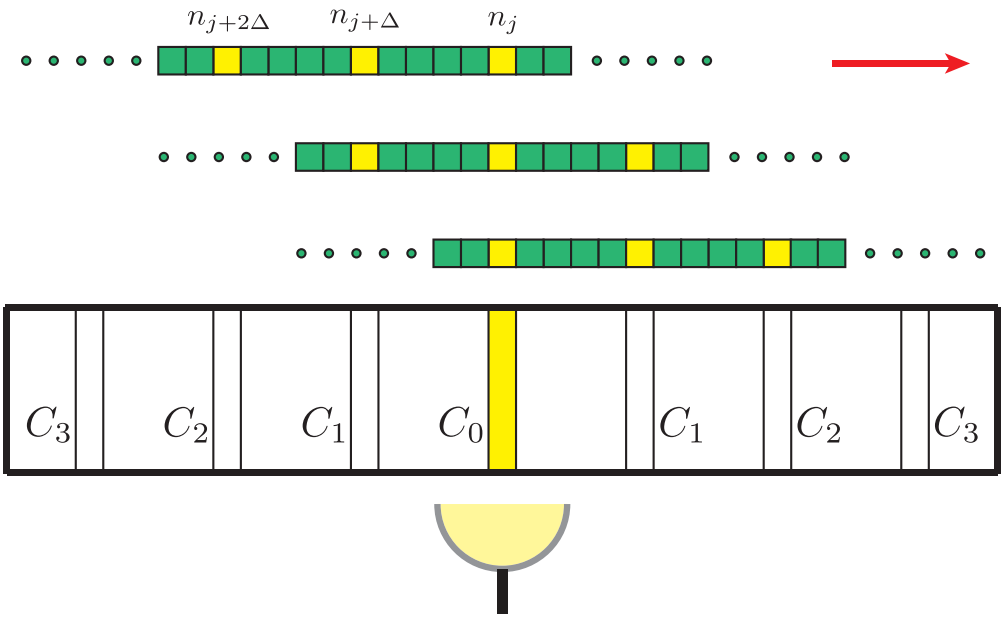

Figure 5.2: Data acquisition process. Shown are three non-consecutive configurations of the slices (highlighted in yellow color) comprising a general set S_j. The measurements for all configurations for S_j form the j-th group. Coupling constants C_i's are labeled at corresponding slits. The red arrow indicates the shifting direction.

5.3.3 Reconstruction Algorithm

All the measurements in the same group are coupled. To extract the information of $n(x)$, we envision the inhomogeneous sample being imaged is derived from a uniform material with index n_b, and compare the differential between measurements. The total field differential introduced by the sample is a linear summation of the contributions from all slits, and each contribution is proportional to the local index variation at every slit. For example, the first measurement E_j in the j-th group is taken to have the following form:

$$E_j = E_b + (n_j - n_b)C_0E_{\text{inc}} + (n_{(j+\Delta)} - n_b)C_1E_{\text{inc}} + (n_{(j+2\Delta)} - n_b)C_2E_{\text{inc}} + \cdots , \qquad (5.1)$$

where E_{inc} is the electric field of the incoming light, and E_b is the field strength for a uniform sample with index n_b, which can be obtained numerically. The dimensionless quantity $C_i, i = 0, 1, 2, \cdots$ describes the self- and mutual-couplings between the detection slit and its neighboring slits (Fig. 5.2). C_i's can be either positive or negative, and can be numerically

determined for specified index variation. Within the j-th group, the N measurements can be recast into a compact matrix form

$$\begin{pmatrix} C_0 & C_1 & C_2 & \cdots & C_{N-1} \\ C_1 & C_0 & C_1 & \cdots & C_{N-2} \\ C_2 & C_1 & C_0 & \cdots & C_{N-3} \\ \vdots & \vdots & \vdots & \vdots & \vdots \\ C_{N-1} & C_{N-2} & C_{N-3} & \cdots & C_0 \end{pmatrix}_{N\times N} \begin{pmatrix} \Delta n_j \\ \Delta n_{(j+\Delta)} \\ \Delta n_{(j+2\Delta)} \\ \vdots \\ \Delta n_{(j+(N-1)\Delta)} \end{pmatrix}_{N\times 1} = \begin{pmatrix} \Delta\tilde{E}_j \\ \Delta\tilde{E}_{(j+\Delta)} \\ \Delta\tilde{E}_{(j+2\Delta)} \\ \vdots \\ \Delta\tilde{E}_{(j+(N-1)\Delta)} \end{pmatrix}_{N\times 1}, \tag{5.2}$$

with $\Delta\tilde{E}_j = (E_j - E_b)/E_{\text{inc}}$ and $\Delta n_j = n_j - n_b$. Repeating the process for all groups to solve for all Δn provides $n(x)$ for the entire segment being imaged. It is worth mentioning that a rescaling of all C_i's does not change the contrast of the reconstructed image. Moreover, in practice, the CNT-lens can be designed such that only the first few C_i's make contributions. Such an approach is validated by numerical simulations; it is numerically found that a good choice of n_b based upon the knowledge of the sample greatly increases the accuracy. The algorithm is also robust for a fairly wide range of n_b. One of the advantages of the differential algorithm is that, as only the differential of the fields is used, ultra-high resolution can still be achieved even if fabrication imperfections are present in the grating.

5.4 Numerical Simulations

Having introduced the general scheme, we now demonstrate the superior performance of the CNT-lens. The CNT-lens is made of silver, which has an index $n_{\text{Ag}} = 0.99886 - 14.128i$ [120] at wavelength $\lambda = 2.08\,\mu$m (e.g. HO:YAG laser). The grating is designed so that $d = 400\,$nm and $a = 40\,$nm, with unfilled slits, and the thickness is $L = 662\,$nm such that the grating is on resonance with the illuminating light. Numerically, the CNT-lens transmits 66% of light and reflects only 3% (the remaining dissipates).

5.4.1 Imaging Isolated Defects

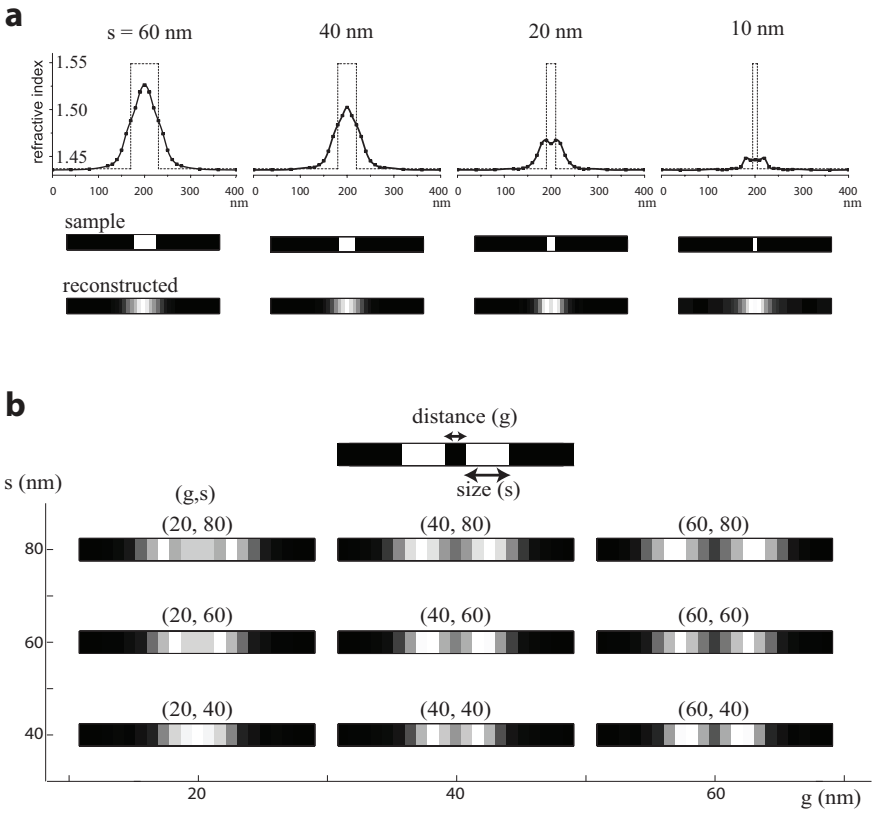

Figure 5.3: (a) Reconstructed images of a small defect in an otherwise uniform silica. The dashed lines describe the sample index profile, while the black dots connected by solid lines denote the reconstructed index profile. To aid the visualization, the sample and the reconstructed images are also plotted using the grey scale color map, with white and black colors indicating the maximum and minimum values, respectively, in each case. (b) Reconstructed images of two small defects in proximity, with varying size and separation.

Applying the reconstruction algorithm, Fig. 5.3a shows the reconstructed images of a 40 nm-thick sample containing a single defect ($n = 1.54893$, e.g. Barium crown glass, N-BAK1 [121]) in an otherwise uniform silica ($n = 1.43689$ [122]). n_b is chosen to be the index of silica. The defects with different sizes $s = 60\,\text{nm}$, $40\,\text{nm}$, $20\,\text{nm}$, and $10\,\text{nm}$, respectively, are imaged. The reconstructed images have FWHM 70 nm, 62 nm, 58 nm, and 53 nm, respectively. For even smaller defects, the FWHM is found numerically to approach the size of the light torch ($\sim a$), which gives the point spread function (PSF) of the imaging system. That is, for features that are smaller than the slit width, their images are blurred to be no less than the

slit width. We note that the two kinks in the two larger samples and the two peaks in the two smaller samples are due to the strong evanescent electric field in the y-direction right at the corner of the slits; numerically, we found that they disappear when the sample is slightly away (say 10 nm) from the CNT-lens.

Next, we investigate the resolving power of the CNT-lens to distinguish a small distance g between two small defects with size s. The reconstructed images are shown in Fig. 5.3b. The results indicate that when $g \geq 40\,\text{nm}$ $(= a)$, the two defects can always be distinguished regardless of their size. On the other hand, the results show that a very small distance $(g = 20\,\text{nm})$ between two large defects $(s = 80, 60\,\text{nm})$ can be resolved by the CNT-lens. Such a case, from our algorithm, can be considered as the complementary case wherein a small defect with size g is embedded in an otherwise homogenous material. The result does not violate the well known Abbe-Rayleigh criterion, which describes the resolving power between two point objects.

5.4.2 Imaging Samples with Varying Index Profile

Till now, we assume that the detector placed in the near field does not perturb the measurements significantly. In practice, such a perturbation introduced by a measuring aperture is always present. Here we show that accurate image reconstruction is still possible in the presence of the near field perturbation. Consider a slab waveguide permeating through the light torch of the detection slit (Fig. 5.4a). The waveguide can perturb the strong evanescent field, and excite propagating waves inside the waveguide, which can be propagated afar to be measured at the other end. Fig. 5.4b shows the reconstructed image for a $1.2\,\mu$m long sample, and both the reconstructed images with (red squares) and without (blue dots) the waveguide are in good agreement with the original index profile. The slab waveguide is made of silicon ($n = 3.44989$ [122]), embedded in a silica substrate. The width of the slab waveguide is $w_w = 250\,\text{nm}$ and the gap between the waveguide and the CNT-lens is

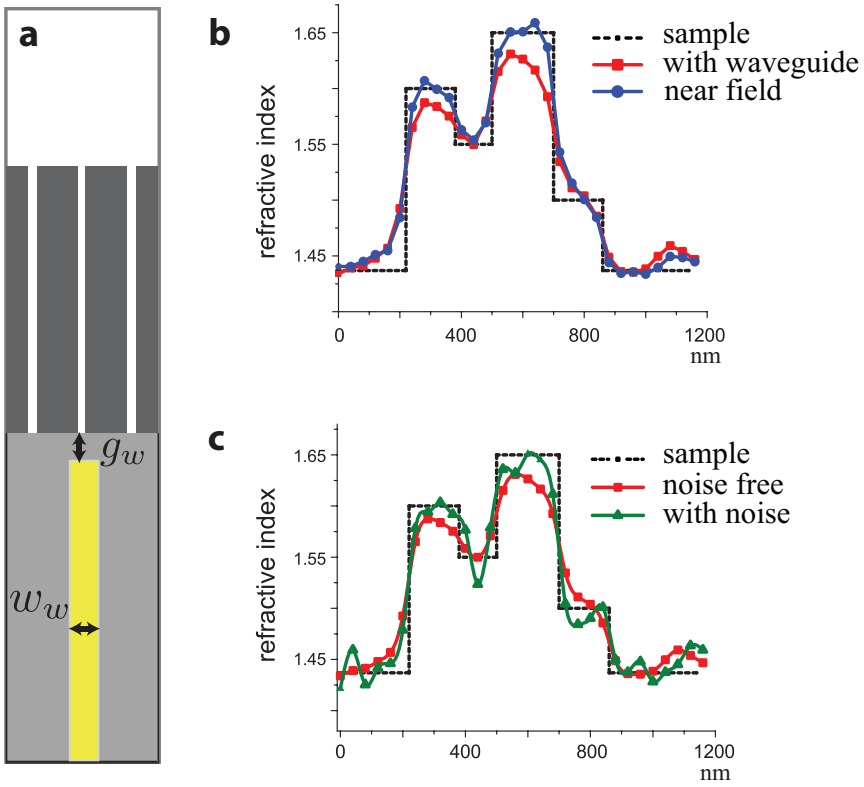

Figure 5.4: (a) Schematic of a slab waveguide in the proximity of the detection slit. (b) Index profile of the sample (dashed line), the reconstructed index profile with (red squares) and without (blue dots) the waveguide. The thick lines in the reconstructed profiles are obtained by spline interpolation method. (c) Index profile of the sample (dashed line), and of the reconstructed image with (green triangles) and without (red squares) noises.

$g_w = 210\,\text{nm}$, determined through an optimization procedure: w_w is fixed so that only the first three coupling constants are significant and $|C_1/C_0| = 0.67$, $|C_2/C_0| = 0.29$; g_w is decided by maximizing $|C_0|$ so that the contrast in the image is as large as possible. Another important issue that degrades the performance of any imaging system is the noise. Here we demonstrate the robustness of the CNT-lens against external local random noises by adding the noises to the measurements E_j (E_b is essentially noise-free, either when obtained numerically, or measured experimentally for an extended period of time). The intensity of random noises is represented by $0.2\% \times I \times C_{\text{Rand}}$, where I is the incident intensity and C_{Rand} is a random number between $[-1, 1]$. Fig. 5.4c shows the reconstructed image with (green triangles) and without (red squares) noises, assuming the presence of the waveguide.

5.4.3 Imaging Samples with Complex Index Profile

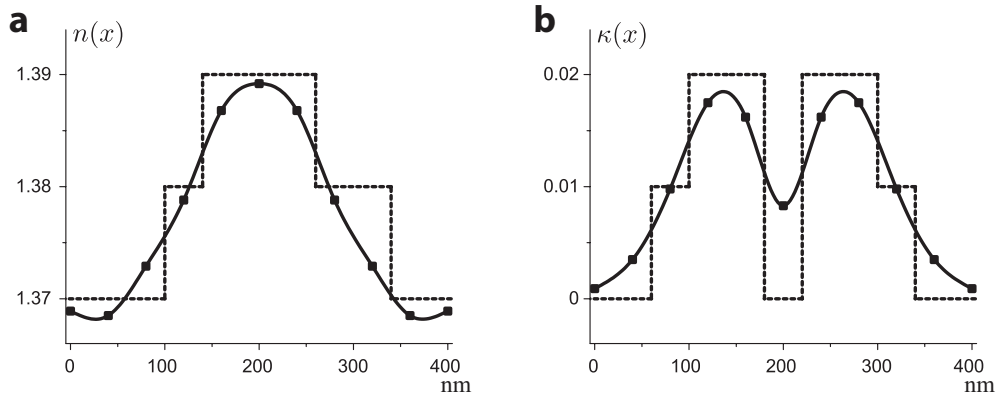

Figure 5.5: Reconstruction of the complex refractive index. (a) The real part. The sample is denoted by the dashed line and the reconstructed image is denoted by black dots connected with a solid line. (b) The imaginary part.

In most biological tissues, due to light scattering and absorption, the optical property is described by a spatially varying complex refractive index: $\tilde{n}(x) = n(x) + i\kappa(x)$. The correlations between the slits allow us to determine $\tilde{n}(x)$ in one scanning process by using two detectors. In such a situation, when one slit is covered by a sample with a complex index, $n(x)$ and $\kappa(x)$ contribute independently to the total measured differential field (in general $n(x)$ and $\kappa(x)$ give rise to two different set of coupling constants). By measuring at two neighboring slits (or in general, any two correlated slits), $\tilde{n}(x)$ can be determined by applying the reconstruction algorithm outlined above. Fig. 5.5 shows the reconstructed complex refractive index profile. Such a capability to reconstruct the complex index based on correlations is not possible in the single-slit scenario.

5.5 Summary and Expectation

In this Chapter, we propose a conceptually new designs of the CNT-lens, which provides a promising alternative modality to achieve ultra-high resolution in optical imaging. The scalability of the CNT-lens, i.e., to work at different optical frequencies by designing the

lens with different dimensions, provides a unique feature to find broad applications. Also, the sample may be shifted continuously and steadily, while the detector is timed to take measurements at fixed time intervals. Together with simultaneous multi-channel detection, the data acquisition time can be significantly reduced. For samples with exceedingly large index contrast, the reconstruction algorithm can be generalized to use the nonlinear differential to accurately reconstruct the images. Finally, we note that a two-dimensional image can be obtained by applying twice the one-dimensional scanning process in two orthogonal directions, once in each direction, and does not require a time-consuming exhaustive point-by-point two-dimensional scanning. These capabilities will likely extend the applicability of the CNT-lens.

Chapter 6

Ultralong Nanojet

6.1 Introduction

Another interesting phenomenon that can focus light to a subwavelength spot is photonic nanojet. The photonic nanojet phenomenon was first numerically discovered in 2004 [15]. When the incident light is scattered by a homogenous single dielectric sphere, a high intensity beam with a subwavelength waist emerges on the shadow-side of the sphere. The nanojet has potential applications in nanoparticle sensing [123], subwavelength nanopatterning and nanolithography [124, 125], and the realizations of low-loss coupled resonator optical waveguide (CROW) [126, 127]. For all applications, it is desired that the nanojets extend as far as possible in the forward direction. Using simple ray optics, it can be shown that the photonic nanojet phenomenon occurs only when the sphere index n is less than 2, which gives an upper bound of n (hereafter, we assume the background is air). It can further be shown that the smaller the index n is, the further the nanojet reaches. Nonetheless, the lowest available index for conventional optical materials at visible light frequency range is around 1.37 [128]. The nanojet is only several wavelengths long for a microsphere with an index roughly equal to 1.37. Such a shortcoming can be understood by looking at the energy power flow (Poynting vector) around the focal point (Fig. 6.1a). In such a case, a

rapid convergence near the focal point also unavoidably leads to a fast divergence, thereby a short nanojet. Consequently, to obtain a long nanojet, the key point is to engineer the microsphere so that the power flow near the focal point is essentially parallel so as to have a small angular deviation. Along this direction of reasoning, multilayer microspheres (up to 100 layers) with graded-index between $\sqrt{2}$ and 1 have been proposed and shown to exhibit elongated nanojets [129]. Although intricate nanorod metamaterials can achieve such a low index ($1.05 - 1.28$ [130]), the fabrication and integration with desired index profile are still challenging. In this following, we will show that we design a simple two-layer microsphere structure with required power flow behavior (Fig. 6.1b), with indices readily available from conventional optical materials, to achieve an enormously long nanojet. In particular, we show that for a glass-based two-layer microsphere (e.g., BaF and LaSF), the nanojet has a remarkable extension of 22 wavelengths long. Such a capability will make the nanojet applications more viable.

6.2 Geometry and Underlying Physics

We start by describing the two-layer microsphere geometry (Fig. 6.2). The sphere consists of an inner core of radius R_c and with a refractive index n_c, and of a shell with outer radius R_s and with an index n_s. The enabling feature in this design is that the aforementioned power flow behavior can be accomplished if the core index n_c is smaller than the shell index n_s ($n_c < n_s$). This scenario is different from the previously proposed multilayer microspheres [129] wherein the refractive index monotonically decreases from the core (index $\sqrt{2}$) to the outer shell (index 1). For both multilayer and single microsphere cases, the power flow inside the sphere always converges, while for the proposed two-layer microsphere structure, the power flow inside the sphere experiences alternative convergence and divergence, where the divergence acts to counter-balance and slow down the convergence (Fig. 6.2b). For properly chosen indices, the counter-balance can be effective so as to minimize the divergence angle

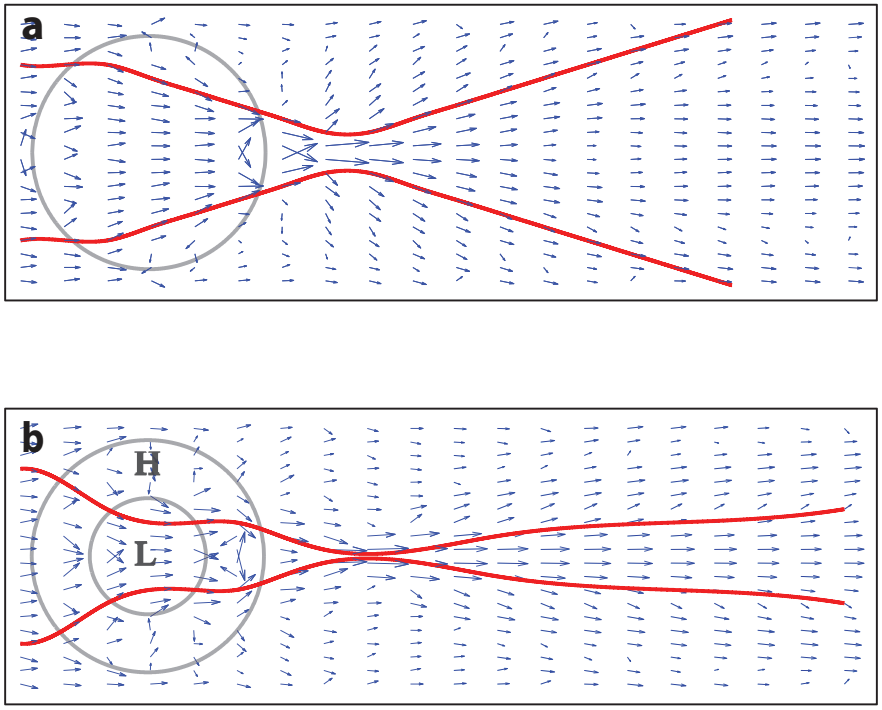

Figure 6.1: Power flow plots for microspheres. (a) A single microsphere. (b) A two-layer microsphere. 'H' and 'L' denote the low index core and high index shell, respectively. The arrows denote the Poynting vectors at each grid point. The two continuous red lines in each figure are the streamlines for the Poynting vector fields, assuming the same two fixed starting points on the incident side for each case.

at the focal point. We emphasize here that the power flow behavior can not be correctly inferred from the trajectory of the ray optics, as the dimensions of the layers are of the same orders of magnitude as the wavelength. Full-wave treatment is required to obtain numerically correct behavior.

6.3 Intensity Distributions

Having introduced the criteria for elongated nanojets, we now plot the intensity distributions of the nanojets using the exact Mie theory [37] (see Appendix E) to provide a direct visualization of the nanojets. For an incident plane wave propagating along the z-direction and linearly polarized in the x-direction (Fig. 6.2), Fig. 6.3 plots the intensity distributions

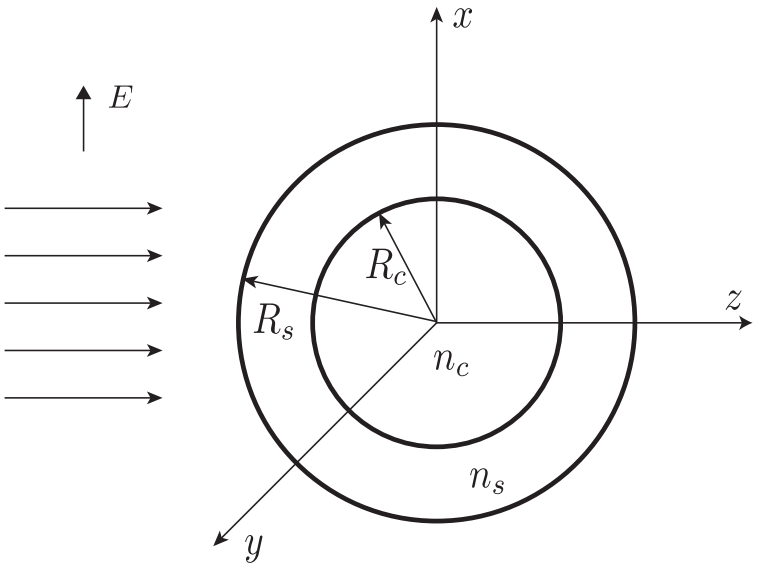

Figure 6.2: Schematics of the two-layer microsphere. The sphere consists of an inner core of radius R_c and with a refractive index n_c, and of a shell with outer radius R_s and with an index n_s. The directions of the incident plane wave and the polarization are also denoted.

for the scattering processes. While plotting, we sum up the vector spherical harmonics up to order $n = 45$. We have checked the convergence such that, when order $n = 46$ is added, the relative electric field change is less than 10^{-4} at all grid points. Fig. 6.3a plots the nanojet for a single microsphere case, while Fig. 6.3b plots the nanojet for the case of a two-layer microsphere. To plot the intensity distributions, we have chosen the wavelength of the incident light to be $\lambda = 632.8\,\text{nm}$ (He-Ne laser); and the radius of the single sphere is $R = 5\lambda$, $n = 1.377$ (MgF_2 [122]); the two-layer microsphere is designed with $R_c = 2.5\lambda$, $n_c = 1.6028$ (BaF [121]), and $R_s = 5\lambda$, $n_s = 1.8445$ (LaSF [121]). For different wavelengths, the same geometry also works as long as the indices are kept the same. The intensity profile on the z-axis is also plotted for each case. To quantify the extensions of the nanojets, we define the beam length L as the distance on the z-axis from the edge of the sphere on the shadow side ($z/\lambda = 5$ in the intensity profile plots) to the spatial point where the intensity drops to twice of that of the incident light (the same definition is also adopted in [129]). The designed two-layer microsphere has a beam length $L \sim 22\lambda$, which is more than twice longer than that for the single sphere case ($L \sim 9\lambda$). In Fig. 6.3, the intensity profile in the

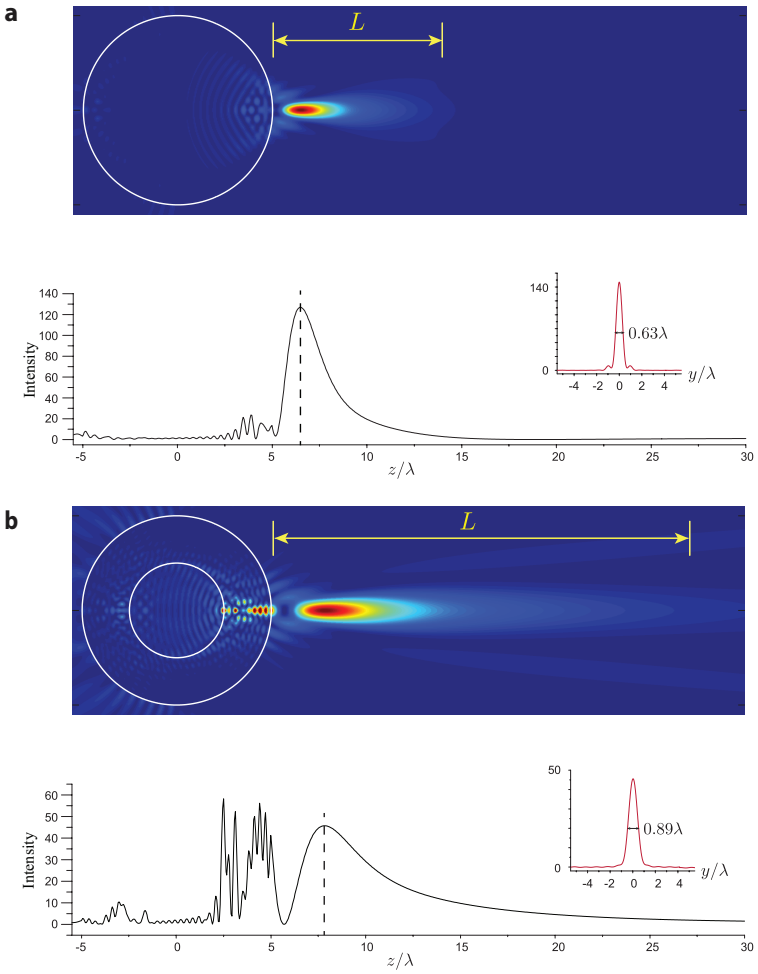

Figure 6.3: Intensity plots of the nanojets. (a) A single microsphere with $R = 5\lambda$, $n = 1.377$ (MgF_2). (b) A two-layer microsphere with $R_c = 2.5\lambda$, $n_c = 1.6028$, and $R_s = 5\lambda$, $n_s = 1.8445$. In each case, the upper panel plots the intensity for the $y - z$ plane; and the lower panel plots the intensity profile along the z-direction. In the intensity profile, the origin of coordinate corresponds to the center of the sphere, and the locations of the focal points are denoted by the dashed lines. Transverse profile at the focal point is also shown in the inset. To clearly show the details of the nanojets, the maximum value of the colormap is chosen to be the value at the focal point.

transverse y-direction (beam waist) at the focal point is also plotted in the inset. Although the elongated nanojet in the two-layer microsphere case has a broadened transverse profile compared with that of the single sphere case, its full width at half maximum (FWHM) is still at subwavelength scale ($\sim 0.89\,\lambda$). We now comment on some properties of the intensity profiles of the nanojets. Firstly, for the two-layer microsphere case, as the nanojet is much longer and slightly wider, energy conservation implies that the intensity at the focal point is accordingly somewhat smaller than that for the single sphere case (46 vs 127 in units of the intensity of the incoming light). Secondly, due to the multiple scatterings in the outer shell for the two-layer microsphere case, there exists strong standing-wave-like interferences in the outer shell. In contrast, the interferences in the single sphere case is much weaker.

More significantly, using the same low-index core high-index shell design strategy, we now show that long nanojets can be formed by using materials with index larger than 2. Such a capability opens up a wide range of materials for nanojet generation. To date, materials with such a large refractive index are excluded from the considerations for nanojet generation for both single sphere and graded-index multilayer microsphere cases, due to the ray optics predictions and aforementioned monotonically convergence processes. By introducing the counter-balance mechanism for alternative convergence and divergence in the two-layer microsphere structures, our design can accommodate large index materials (≥ 2) to form long nanojets. Notably, long nanojets at infrared frequency range using semiconductor materials (doped and undoped) now become readily feasible. Fig. 6.4 shows an elongated nanojet with $L \sim 15\lambda$ formed by a two-layer microsphere ($R_c = 2.5\lambda$, $n_c = 2$; $R_s = 5\lambda$, $n_s = 3.85$). The same strong standing-wave-like interferences can also be seen in the outer shell. Here, we note that using semiconductors to form nanojets has been discussed in [15]. In that case, however, the background has an index larger than 1, so that the ratio between the refractive index of the sphere and the background is still less than 2. That is, nanojet generation using semiconductors in air has not been achieved so far. Moreover, we note that the refractive index upper bound $n = 2$ given by the ray optics is overestimated. By applying the full-wave

analysis, we found that for a single microsphere with $R = 5\lambda$, the largest index to form a nanojet is only around 1.75, which is 12.5% smaller than that given by the ray optics.

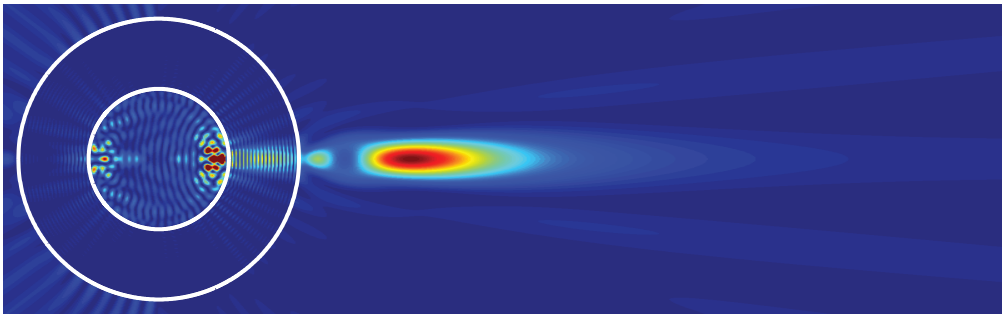

Figure 6.4: A long nanojet formed by a two-layer microsphere with high refractive index materials ($n_c = 2$, $n_s = 3.85$, $R_c = 2.5\lambda$, and $R_s = 5\lambda$).

6.4 Summary and Expectation

In this Chapter, we designed a simple two-layer microsphere, which can generate an ultralong nanojet, using conventionally available optical materials. We further show that long nanojets can be formed using semiconductor materials at infrared frequencies. This capability will greatly facilitate the successful applications of nanojets.

References

[1] Y. Cui, Q. Wei, H. Park, and C.M. Lieber. Nanowire nanosensors for highly sensitive and selective detection of biological and chemical species. *Science*, 293:1289, 2001.

[2] C. Grillet, C.L.C. Smith, D. Freeman, S. Madden, B. Luther-Davies, E. Magi, and B. Eggleton. Efficient coupling to chalcogenide glass photonic crystal waveguides via silica optical fiber nanowires. *Optics Express*, 14:1070, 2006.

[3] L. Tong, R.R. Gattass, J.B. Ashcom, S. He, J. Lou, M. Shen, and E. Mazur. Subwavelength-diameter silica wires for low-loss optical wave guiding. *Nature*, 426:816, 2003.

[4] D. Loss and D.P. DiVincenzo. Quantum computation with quantum dots. *Physical Review A*, 57:120, 1998.

[5] X. Michalet, F.F. Pinaud, L.A. Bentolila, J.M. Tsay, S.J.J.L. Doose, J.J. Li, and S. Weiss. Quantum dots for live cells, in vivo imaging, and diagnostics. *Science*, 307:538, 2005.

[6] D.R. Smith, J.B. Pendry, and M.C. Wiltshire. Metamaterials and negative refractive index. *Science*, 305:788, 2004.

[7] J.T. Shen, P.B. Catrysse, and S. Fan. Mechanism for designing metallic metamaterials with a high index of refraction. *Physical Review Letters*, 94:197401, 2005.

[8] K.J. Vahala. Optical microcavities. *Nature*, 424:839, 2003.

[9] Y. Shen and J.T. Shen. Nanoparticle sensing using whispering-gallery-mode resonators: plasmonic and rayleigh scatterers. *Physical Review A*, 85:013801, 2012.

[10] Y. Shen and J. T. Shen. Numerical investigation of rayleigh nanoparticlesensing using a whispering-gallery-mode resonator. *Journal of the Optical Society of America B*, 29:2897, 2012.

[11] Y. Shen, D.R. Chen, and J.T. Shen. Statistical theory of nanoparticle sensing using a whispering-gallery-mode resonator. *Physical Review A*, 85:063808, 2012.

[12] Y. Shen, M. Bradford, and J.T. Shen. Single-photon diode by exploiting the photon polarization in a waveguide. *Physical review letters*, 107:173902, 2011.

[13] Y. Shen and J.T. Shen. Photonic fock states scattering in waveguide QED and their correlation functions. *In Press*, 2015.

[14] Y. Shen and J.T. Wang, L.V. amd Shen. Deep subwavelength optical imaging using correlated nano-torches. *Applied Physics Letters*, 103:1119, 2013.

[15] Z. Chen, A. Taflove, and V. Backman. Photonic nanojet enhancement of backscattering of light by nanoparticles: a potential novel visible-light ultramicroscopy technique. *Optics Express*, 12:1214, 2004.

[16] Y. Shen, L.V. Wang, and J.T. Shen. Ultralong photonic nanojet formed by a two-layer dielectric microsphere. *Optics Letters*, 39:4120, 2014.

[17] S. Menon, J. Hansen, L. Nazarenko, and Y. Luo. Climate effects of black carbon aerosols in China and India. *Science*, 297:5590, 2002.

[18] S.T. Holgate, J.M. Koren, J.M. Samet, and R.L. Maynard. *Air pollution and health*. Academic Press, San Diego, 1999.

[19] M.R. Hilleman. Overview: cause and prevention in biowarfare and bioterrorism. *Vaccine*, 20:3055, 2002.

[20] M.V. Yezhelyev, X. Gao, Y. Xing, A. Al-Hajj, S. Nie, and R.M. O'Regan. Emerging use of nanoparticles in diagnosis and treatment of breast cancer. *Lancet Oncol*, 7:657, 2006.

[21] J.T. Shen and S. Fan. Theory of single-photon transport in a single-mode waveguide. ii. coupling to a whispering-gallery resonator containing a two-level atom. *Physical Review A*, 79:023838, 2009.

[22] A. Mazzei, S. Gotzinger, L.D.S. Menezes, G. Zumofen, O. Benson, and V. Sandoghdar. Theory of single-photon transport in a single-mode waveguide. ii. coupling to a whispering-gallery resonator containing a two-level atom. *Physical Review Letters*, 99:173603, 2007.

[23] K.R. Hiremath and V.N. Astratov. Perturbations of whispering gallery modes by nanoparticles embedded in microcavities. *Optics express*, 16:5421, 200.

[24] X. Yi, Y.F. Xiao, Y.C. Liu, B.B. Li, Y.L. Chen, Y. Li, and Q. Gong. Multiple-Rayleigh-scatterer-induced mode splitting in a high-Q whispering-gallery-mode microresonator. *Physical Review A*, 83:023803, 2011.

[25] J. Zhu, S.K. Ozdemir, Y.F. Xiao, L. Li, L. He, D.R. Chen, and L. Yang. On-chip single nanoparticle detection and sizing by mode splitting in an ultrahigh-Q microresonator. *Nature Photonics*, 4:46, 2010.

[26] M.A. Santiago-Cordoba, S.V. Boriskina, F. Vollmer, and M.C. Demirel. Nanoparticle-based protein detection by optical shift of a resonant microcavity. *Applied Physics Letters*, 99:7, 2010.

[27] A. B. Matsko and V. S. Ilchenko. Optical resonators with whispering gallery modes i: basics. *IEEE J. Sel. Top. Quantum Electron*, 12:3, 2006.

[28] T. J. Kippenberg, S. M. Spillane, and K. J. Vahala. Modal coupling in traveling-wave resonators. *Optics Letters*, 27:1669, 2002.

[29] J.T. Shen and S. Fan. Theory of single-photon transport in a single-mode waveguide. i. coupling to a cavity containing a two-level atom. *Physical Review A*, 79:023837, 2009.

[30] M.T. Rakher, L. Ma, O. Slattery, X. Tang, and K. Srinivasan. Quantum transduction of telecommunications-band single photons from a quantum dot by frequency upconversion. *Nature Photonics*, 4:786, 2010.

[31] K. Srinivasan and O. Painter. Mode coupling and cavityquantum-dot interactions in a fiber-coupled microdisk cavity. *Physical Review A*, 75:023814, 2007.

[32] http://www.comsol.com.

[33] S.M. Spillane, T.J. Kippenberg, O.J. Painter, and K.J. Vahala. Ideality in a fiber-taper-coupled microresonator system for application to cavity quantum electrodynamics. *Physical Review Letters*, 91:043902, 2003.

[34] S.A. Dyer. *Air pollution and health.* Wiley, 2001.

[35] J.D. Joannopoulos, S.G. Johnson, J.N. Winn, and R.D. Meade. *Photonic crystals: molding the flow of light.* Princeton university press, 2011.

[36] D.J. Griffiths. *Introduction to Electrodynamics.* Prentice Hall, 1999.

[37] C.F. Bohren and D.R. Huffman. *Absorption and scattering of light by small particles.* John Wiley and Sons, 2008.

[38] A.T. Zimmer, P.A. Baron, and P. Biswas. The influence of operating parameters on number-weighted aerosol size distribution generated from a gas metal arc welding process. *Journal of Aerosol Science*, 33:519, 2002.

[39] T. Tuch, P. Brand, H.E. Wichmann, and J. Heyder. Variation of particle number and mass concentration in various size ranges of ambient aerosols in eastern germany. *Atmospheric Environment*, 31:4193, 1997.

[40] L.A. Sgro, G. Basile, A.C. Barone, A. DAnna, P. Minutolo, A. Borghese, and A. DAlessio. Detection of combustion formed nanoparticles. *Chemosphere*, 51:1079, 2003.

[41] D.B. Kittelson, W.F. Watts, and J.P. Johnson. Nanoparticle emissions on minnesota highways. *Atmospheric Environment*, 38:9, 2004.

[42] W.C. Hinds. *Aerosol Technology.* Wiley-Interscience, 1999.

[43] K. Gallo, G. Assanto, K.R. Parameswaran, and M.M. Fejer. All-optical diode in a periodically poled lithium niobate waveguide. *Applied Physics Letters*, 79:314, 2001.

[44] P. Yeh. *Optical waves in layered media.* Wiley, 1988.

[45] B.E.A. Saleh and M.C. Teich. *Fundamentals of Photonics.* Wiley, 2007.

[46] J. Fujita, M. Levy, R.M. Osgood Jr, L. Wilkens, and H. Dotsch. Waveguide optical isolator based on machzehnder interferometer. *Applied Physics Letters*, 76:2158, 2000.

[47] S. Mujumdar and H. Ramachandran. Use of a graded gain random amplifier as an optical diode. *Optics Letters*, 26:929, 2001.

[48] M. Scalora, J.P. Dowling, C.M. Bowden, and M.J. Bloemer. The photonic band edge optical diode. *Journal of Applied Physics*, 76:2023, 1994.

[49] P. Michler, A. Kiraz, C. Becher, W.V. Schoenfeld, P.M. Petroff, and A. Zhang, L. nad Imamoglu. A quantum dot single-photon turnstile device. *Science*, 290:2282, 2000.

[50] C. Kurtsiefer, S. Mayer, P. Zarda, and H. Weinfurter. Stable solid-state source of single photons. *Physical Review Letters*, 85:290, 2000.

[51] E. Moreau, I. Robert, J.M. Gerard, I. Abram, L. Manin, and V. Thierry-Mieg. Single-mode solid-state single photon source based on isolated quantum dots in pillar microcavities. *Applied Physics Letters*, 79:2865, 2001.

[52] A.A. Houck, D.I. Schuster, J.M. Gambetta, J.A. Schreier, B.R. Johnson, J.M. Chow, and R.J. Schoelkopf. Generating single microwave photons in a circuit. *Nature*, 449:328, 2007.

[53] T. Yoshie, A. Scherer, J. Hendrickson, G. Khitrova, H.M. Gibbs, G. Rupper, and D.G. Deppe. Vacuum rabi splitting with a single quantum dot in a photonic crystal nanocavity. *Nature*, 432:200, 2004.

[54] H. De Riedmatten, M. Afzelius, M.U. Staudt, C. Simon, and N. Gisin. A solid-state lightmatter interface at the single-photon level. *Nature*, 456:773, 2008.

[55] K.K. Lee, Y. Avniel, and S.G. Johnson. Design strategies and rigorous conditions for single-polarization single-mode waveguides. *Optics Express*, 16:15170, 2008.

[56] W. Hansen, T.P. Smith III, K.Y. Lee, J.A. Brum, C.M. Knoedler, J.M. Hong, and D.P. Kern. Zeeman bifurcation of quantum-dot spectra. *Physical Review Letters*, 62:2168, 1989.

[57] R. Rinaldi, P.V. Giugno, R. Cingolani, H. Lipsanen, M. Sopanen, J. Tulkki, and J. Ahopelto. Zeeman effect in parabolic quantum dots. *Physical Review Letters*, 77:342, 1996.

[58] R. Hanson, B. Witkamp, L.M.K. Vandersypen, L.W. Van Beveren, J.M. Elzerman, and L.P. Kouwenhoven. Zeeman energy and spin relaxation in a one-electron quantum dot. *Physical Review Letters*, 91:196802, 2003.

[59] W.S. Boyle. Far infrared magneto-optic effects from impurities in germanium. *Journal of Physics and Chemistry of Solids*, 8:321, 1959.

[60] P. Fisher and H.Y. Fan. Optical and magneto-optical absorption effects of group iii impurities in germanium. *Physical Review Letters*, 2:456, 1959.

[61] S. Zwerdling, K.J. Button, and B. Lax. Zeeman effect of impurity levels in silicon. *Physical Reviews*, 118:975, 1960.

[62] K. Seeger. *Semiconductor physics: an introduction*. Springer Science and Business Media, 2004.

[63] R.W. Boyd. *Nonlinear Optics*. Academic, 2008.

[64] J.T. Shen and S. Fan. Coherent photon transport from spontaneous emission in one-dimensional waveguides. *Optics Letters*, 30:2001, 2005.

[65] E. Waks and J. Vuckovic. Dipole induced transparency in drop-filter cavity-waveguide systems. *Physical Review Letters*, 96:153601, 2006.

[66] S. Fan, J.N. Winn, A. Devenyi, J.C. Chen, R.D. Meade, and J.D. Joannopoulos. Guided and defect modes in periodic dielectric waveguides. josa b, 12(7), 1267-1272. *Journal of the Optical Society of America B*, 12:1267, 1995.

[67] E. Harbord, P. Spencer, E. Clarke, and R. Murray. Radiative lifetimes in undoped and p-doped inas/gaas quantum dots. *Physical Review B*, 80:195312, 2009.

[68] T. Mensing, L. Worschech, R. Schwertberger, J.P. Reithmaier, and A. Forchel. Magneto-optical investigations of single self-assembled inas/ingaalas quantum dashes. *Physical Review B*, 82:2799, 2003.

[69] A. Badolato, K. Hennessy, M. Atature, J. Dreiser, E. Hu, P.M. Petroff, and A. Imamoglu. Deterministic coupling of single quantum dots to single nanocavity modes. *Science*, 308:1158, 2005.

[70] A. Dousse, J. Suffczynski, R. Braive, A. Miard, A. Lematre, I. Sagnes, and P. Senellart. Scalable implementation of strongly coupled cavity-quantum dot devices. *Applied Physics Letters*, 94:121102, 2009.

[71] S.M. Thon, M.T. Rakher, H. Kim, J. Gudat, W.T. Irvine, P.M. Petroff, and D. Bouwmeester. Strong coupling through optical positioning of a quantum dot in a photonic crystal cavity. *Applied Physics Letters*, 94:111115, 2009.

[72] T. Van der Sar, J. Hagemeier, W. Pfaff, E.C. Heeres, S.M. Thon, H. Kim, and R. Hanson. Deterministic nanoassembly of a coupled quantum emitterphotonic crystal cavity system. *Applied Physics Letters*, 98:193103, 2011.

[73] A.P. Feresidis, G. Goussetis, S. Wang, and J.C. Vardaxoglou. Artificial magnetic conductor surfaces and their application to low-profile high-gain planar antennas. *Antennas and Propagation, IEEE Transactions on*, 53:209, 2005.

[74] I.V. Lindell and A.H. Sihvola. Perfect electromagnetic conductor. *Journal of Electromagnetic Waves and Applications*, 19:861, 2005.

[75] W. Eickhoff. Stress-induced single-polarization single-mode fiber. *Optics Letters*, 7:629, 1982.

[76] K. Saitoh and M. Koshiba. Single-polarization single-mode photonic crystal fibers. *IEEE Photonics Technology Letters*, 15:1384, 2003.

[77] Hofheinz. M, E.M. Weig, M. Ansmann, R.C. Bialczak, E. Lucero, M. Neeley, A.D. Oconnell, H. Wang, J.M. Martinis, and A.N. Cleland. Generation of fock states in a superconducting quantum circuit. *Nature*, 454:310, 2008.

[78] J. Jacabson, G. Bjork, I. Chuang, and Y. Yamamoto. Photonic de broglie waves. *Physical Review Letters*, 74:4835, 1995.

[79] A.N. Boto, P. Kok, D.S. Abrams, S.L. Braunstein, C.P. Williams, and J.P. Dowling. Quantum interferometric optical lithography: exploiting entanglement to beat the diffraction limit. *Physical Review Letters*, 85:2733, 2000.

[80] S. Bentley and R. Boyd. Nonlinear optical lithography with ultra-high sub-rayleigh resolution. *Optics Express*, 12:5735, 2004.

[81] M. Tsang. Quantum imaging beyond the diffraction limit by optical centroid measurements. *Physical Review Letters*, 102:3601, 2009.

[82] V. Giovannetti, S. Lloyd, L. Maccone, and J.H. Shapiro. Sub-Rayleigh-diffraction-bound quantum imaging. *Physical Review A*, 79:3827, 2009.

[83] C. Monroe. Quantum information processing with atoms and photons. *Nature*, 416:238, 2002.

[84] A. Kuhn, M. Hennrich, and G. Rempe. Deterministic single-photon source for distributed quantum networking. *Physical Review Letters*, 89:7901, 2002.

[85] V.I. Rupasov and V.I. Yudson. Rigorous theory of cooperative spontaneous emission of radiation from a lumped system of two-level atoms: Bethe ansatz method. Zh Èksp Teor Fiz, 87:1617, 1984.

[86] S. Fan, S.E. Kocabas, and J.T. Shen. Input-output formalism for few-photon transport in one-dimensional nanophotonic waveguides coupled to a qubit. *Physical Review A*, 82:063821, 2010.

[87] J.T. Shen and S. Fan. Strongly correlated multiparticle transport in one dimension through a quantum impurity. *Physical Review A*, 76:062709, 2007.

[88] J. Daboul and M.M. Nieto. Quantum bound states with zero binding energy. *Physical Review A*, 195:357, 1994.

[89] K. Hennessy, A. Badolato, M. Winger, D. Gerace, M. Atature, S. Gulde, S. Falt, E.L. Hu, and A. Imamoglu. Quantum nature of a strongly coupled single quantum dot–cavity system. *Nature*, 445:896, 2007.

[90] I. Fushman, D. Englund, A. Faraon, N. Stoltz, P. Petroff, and J. Vuckovic. Controlled phase shifts with a single quantum dot. *Science*, 320:769, 2008.

[91] J. You and F. Nori. Atomic physics and quantum optics using superconducting circuits. *Nature*, 474:589, 2011.

[92] A. Wallraff, D.I. Schuster, A. Blais, L. Frunzio, R. Huang, J. Majer, S. Kumar, S.M. Girvin, and R.J. Schoelkopf. Strong coupling of a single photon to a superconducting qubit using circuit quantum electrodynamics. *Nature*, 431:162, 2004.

[93] N.B. Manson, J.P. harrison, and M.J. Sellars. Nitrogen-vacancy center in diamond: Model of the electronic structure and associated dynamics. *Physical Review B*, 74:4303, 2006.

[94] J. Eschner, C. Raab, F. Schmidt-Kaler, and R. Blatt. Light interference from single atoms and their mirror images. *Nature*, 413:6855, 2001.

[95] C.J. Hood, M.S. Chapman, T.W. Lynn, and H.J. Kimble. Real-time cavity qed with single atoms. *Physical Review Letters*, 80:4157, 1998.

[96] M. Tokushima, H. Kosaka, A. TomitaT, and H. Yamada. Lightwave propagation through a 120 sharply bent single-line-defect photonic crystal waveguide. *Physical Review Letters*, 76:952, 2000.

[97] T. Lund-Hansen, S. Stobbe, B. Julsgaard, H. Thyrrestrup, T. Sunner, M. Kamp, A. Forchel, and P. Lodahl. Experimental realization of highly efficient broadband coupling of single quantum dots to a photonic crystal waveguide. *Physical Review Letters*, 101:113903, 2008.

[98] V.S.C.M. Rao and S. Hughes. Single quantum-dot purcell factor and β factor in a photonic crystal waveguide. *Physical Review B*, 75:205437, 2007.

[99] F.D.M. Haldane and S. Raghu. Possible realization of directional optical waveguides in photonic crystals with broken time-reversal symmetry. *Physical Review Letters*, 100:013904, 2008.

[100] Z. Wang, Y.D. Chong, J. Joannopoulos, and M. Soljacic. Reflection-free one-way edge modes in a gyromagnetic photonic crystal. *Physical Review Letters*, 100:013905, 2008.

[101] W. Greiner and J. Reinhardt. *Field quantization.* Springer, 1996.

[102] J.J. Sakurai. *Modern Quantum Mechanics.* Addison-Wesley, 1994.

[103] M. Karbach and G. Muller. Introduction to the bethe ansatz ii. *arXiv*, 1998.

[104] G.H. Hardy and S. Ramanujan. Asymptotic formulaæ in combinatory analysis. *Proceedings of the London Mathematical Societ*, 2:75, 1918.

[105] L. Mandel and E. Wolf. *Optical coherence and quantum optics.* Cambridge university press, 1995.

[106] H.J. Kimble, M. Dagenasis, and L. Mandel. Photon antibunching in resonance fluorescence. *Physical Review Letters*, 39:691, 1977.

[107] J.T. Hoffges, H.W. Baldauf, T. Eichler, S.R. Helmfrid, and H. Walther. Heterodyne measurement of the fluorescent radiation of a single trapped ion. *Optics Communications*, 133:170, 1997.

[108] J.B. Pendry. Negative refraction makes a perfect lens. *Physical Review Letters*, 85:3966, 2000.

[109] Z. Jacob, L. Alekseyev, and E. Narimanov. Optical hyperlens: far-field imaging beyond the diffraction limit. *Optics Express*, 14:8247, 2006.

[110] E. Betzig, G.H. Patterson, R. Sougrat, W. Lindwasser, S. Olenych, J.S. Bonifacino, M.W. Davidson, J. Lippincott-Schwartz, and H.F. Hess. Imaging intracellular fluorescent proteins at nanometer resolution. *Science*, 313:1642, 2006.

[111] M.J. Rust, M. Bates, and X. Zhuang. Sub-diffraction-limit imaging by stochastic optical reconstruction microscopy (STORM). *Nature Methods*, 3:793, 2006.

[112] E.T.F. Rogers, J. Lindberg, T. Roy, S. Savo, J.E. Chad, M.R. Dennis, and N.I. Zheludev. A super-oscillatory lens optical microscope for subwavelength imaging. *ature materials*, 11:432, 2012.

[113] S.W. Hell. Toward fluorescence nanoscopy. *Nature materials*, 21:1347, 2003.

[114] B. Huang, W. Wang, M. Bates, and X. Zhuang. Three-dimensional super-resolution imaging by stochastic optical reconstruction microscopy. *Science*, 319:5864, 2008.

[115] A. Cuche, A. Drezet, Y. Sonnefraud, O. Faklaris, F. Treussart, J.F. Roch, and Huant. S. Near-field optical microscopy with a nanodiamond-based single-photon tip. *Optics Express*, 17:19969, 2009.

[116] D.W. Pohl, W. Denk, and M. Lanz. Optical stethoscopy: Image recording with resolution $\lambda/20$. *Applied Physics Letters*, 44:651, 1984.

[117] E Betzig, A. Lewis, A. Harootunian, M. Isaacson, and E. Kratschmer. Near field scanning optical microscopy (NSOM): Development and biophysical applications. *Biophysical Journal*, 49:269, 1986.

[118] S.W. Hell. Far-field optical nanoscopy. *Science*, 316:5828, 2007.

[119] A. Pimenov and A. Loidl. Experimental demonstration of artificial dielectrics with a high index of refraction. *Physical Review B*, 74:193102, 2006.

[120] E.D. Palik. *Handbook of Optical Constants of Solids: Index*. Academic press, 1998.

[121] Schott optical glass data sheet catalog. http://www.us.schott.com/english/index.html.

[122] M. Bass, C. DeCusatis, J. Enoch, V. Lakshminarayanan, G. Li, C. MacDonald, V. Mahajan, and E.V. Stryland. *Handbook of optics, Third Edition Volume IV: Optical Properties of Materials, Nonlinear Optics, Quantum Optics*. McGraw-Hill, 2009.

[123] X. Li, Z. Chen, A. Taflove, and V. Backman. Optical analysis of nanoparticles via enhanced backscattering facilitated by 3-d photonic nanojets. *Optics Express*, 13:526, 2005.

[124] E. Mcleod and C.B. Arnold. Subwavelength direct-write nanopatterning using optically trapped microspheres. *Nature nanotechnology*, 3:413, 2008.

[125] W. Wu, A. Katsnelson, O.G. Memis, and H. Mohseni. A deep sub-wavelength process for the formation of highly uniform arrays of nanoholes and nanopillars. *Nanotechnology*, 18:485302, 2007.

[126] A. Kapitonov and V. Astratov. Observation of nanojet-induced modes with small propagation losses in chains of coupled spherical cavities. *Optics Letters*, 32:409, 2007.

[127] S. Yang and V.N. Astratov. Photonic nanojet-induced modes in chains of size-disordered microspheres with an attenuation of only 0.08 db per sphere. *Applied Physics Letters*, 92:261111, 2008.

[128] E.F. Schubert, J.K. Kim, and J.Q. Xi. Low-refractive-index materials: A new class of optical thin-film materials. *physica status solidi (b)*, 244:3002, 2007.

[129] S.C. Kong, A Taflove, and V. Backman. Quasi one-dimensional light beam generated by a graded-index microsphere. *Optics Express*, 17:3722, 2009.

[130] L.W. Hrubesh and J.F. Poco. Method of producing optical quality glass having a selected refractive index. *US Patent*, 6:158, 2000.

[131] M. Scully and M. Zubairy. *Quantum optics*. Cambridge university press, 1997.

[132] M. Bradford and J.T. Shen. Numerical approach to statistical properties of resonance fluorescence. *Optics Letters*, 39:5558, 2014.

Appendix A

N-photon Eigenstates in the Chiral System

In this Appendix, we show the details of how to construct the eigenstates by solving Eq. 4.5 and Eq. 4.6. To begin with, a direct observation of Eq. 4.5 reveals that in the region wherein none of the coordinates is zero, Eq. 4.5 describes a free system, and thereby permitting plane wave solution. Thus, the general form of eigenstate wavefunction in the region $x_1 < x_2 <$

$\cdots < x_N$ can be parameterized as follows:

$$f(x_1, x_2, \cdots, x_N) = \begin{cases} \sum_{\mathcal{P}\in S_N} A_{N+1}(\mathcal{P}) \exp(i \sum_{j=1}^{N} k_j x_{\mathcal{P}_j}), \\ \quad \text{in subregion } N+1 \quad (x_1 < x_2 < \cdots < x_N < 0), \\ \sum_{\mathcal{P}\in S_N} A_N(\mathcal{P}) \exp(i \sum_{j=1}^{N} k_j x_{\mathcal{P}_j}), \\ \quad \text{in subregion } N \quad (x_1 < x_2 < \cdots < x_{N-1} < 0 < x_N), \\ \qquad \cdots \\ \qquad \cdots \\ \qquad \cdots \\ \sum_{\mathcal{P}\in S_N} A_1(\mathcal{P}) \exp(i \sum_{j=1}^{N} k_j x_{\mathcal{P}_j}), \\ \quad \text{in subregion } 1 \quad (0 < x_1 < x_2 < \cdots < x_N). \end{cases} \tag{A.1}$$

In this expression, we restrict to the region of $x_1 < x_2 < \cdots < x_N$, and the expressions of the wavefunction in other regions can be obtained using the bosonic symmetry. k_1, k_2, $\cdots$, and k_N are in general N complex numbers subject to the constraint of $k_1+k_2+\cdots+k_N = E/(v\hbar)$, among others. The orders of the k's are fixed. The summation $\mathcal{P} \in S_N$ accounts for all the $N!$ permutations of the labels $\{1, 2, \cdots, N\}$, and is assigned to the coordinates x's. All the coefficients A's, in addition to their explicit labels, are in general a function of all the k's and the corresponding $\mathcal{P}$. With this wavefunction, one can use the boundary conditions in Eq. 4.5 and Eq. 4.6 to determine all the constrains regarding to the coefficients A's and wave numbers k's.

A.1 N-photon Extended State

To proceed, the first attempt is to assume all the k's are real and all the $N!$ A's are nonzero. To investigate those coefficient relations, we focus on two representative terms in the same

subregion, which are $e^{\cdots+k_m x_j+\cdots+k_n x_{j+1}+\cdots}$ and $e^{\cdots+k_m x_{j+1}+\cdots+k_n x_j+\cdots}$ with $1 \le m < n \le N$ and $j = 1, 2, \cdots, N-1$. Except for the exchange of x_j and x_{j+1}, these two terms have exact the same orders of the other coordinates. Specifically, we rewrite the wavefunction to explicitly show the two terms,

$$
f(x_1, x_2, \cdots, x_N) = \begin{cases}
\cdots + A_{N+1}(\cdots, j, \cdots, j+1, \cdots) e^{i(\cdots+k_m x_j+\cdots+k_n x_{j+1}+\cdots)} + \cdots \\
\cdots + A_{N+1}(\cdots, j+1, \cdots, j, \cdots) e^{i(\cdots+k_m x_{j+1}+\cdots+k_n x_j+\cdots)} + \cdots, \\
\quad \text{in subregion } N+1 \quad (x_1 < x_2 < \cdots < x_N < 0), \\
\\
\cdots + A_N(\cdots, j, \cdots, j+1, \cdots) e^{i(\cdots+k_m x_j+\cdots+k_n x_{j+1}+\cdots)} + \cdots \\
\cdots + A_N(\cdots, j+1, \cdots, j, \cdots) e^{i(\cdots+k_m x_{j+1}+\cdots+k_n x_j+\cdots)} + \cdots, \\
\quad \text{in subregion } N \quad (x_1 < x_2 < \cdots < x_{N-1} < 0 < x_N), \\
\\
\qquad \cdots \\
\qquad \cdots \\
\qquad \cdots \\
\\
\cdots + A_1(\cdots, j, \cdots, j+1, \cdots) e^{i(\cdots+k_m x_j+\cdots+k_n x_{j+1}+\cdots)} + \cdots \\
\cdots + A_1(\cdots, j+1, \cdots, j, \cdots) e^{i(\cdots+k_m x_{j+1}+\cdots+k_n x_j+\cdots)} + \cdots, \\
\quad \text{in subregion } 1 \quad (0 < x_1 < x_2 < \cdots < x_N).
\end{cases}
\tag{A.2}
$$

By investigating the boundary between subregion $N+1$ and subregion N where x_N crosses from 0^- to 0^+, the two equations of motion to be solved now become

$$-iv\left[f(x_1,x_2,\cdots,x_{N-1},0^+)-f(x_1,x_2,\cdots,x_{N-1},0^-)\right]+\frac{V}{\sqrt{N}}e(x_1,x_2,\cdots,x_{N-1})=0, \tag{A.3}$$

$$iv\left[-\frac{\partial}{\partial x_1}-\frac{\partial}{\partial x_2}-\cdots-\frac{\partial}{\partial x_{N-1}}-(E/\hbar-\Omega)\right]e(x_1,x_2,\cdots,x_{N-1})+\frac{\sqrt{N}V}{2}[f(x_1,x_2,\cdots,x_{N-1},0^+)+f(x_1,x_2,\cdots,x_{N-1},0^-)]=0. \tag{A.4}$$

By substituting Eq. A.2 into the above Eq. A.3 and Eq. A.4, we obtain the following coefficient relations:

$$\begin{aligned}
A_N(\cdots,j,\cdots,j+1,\cdots)&=\frac{k^{(x_N)}-\Omega/v-i\Gamma/(2v)}{k^{(x_N)}-\Omega/v+i\Gamma/(2v)}A_{N+1}(\cdots,j,\cdots,j+1,\cdots)=t_{k^{(x_N)}}A_{N+1}(\cdots,j,\cdots,j+1,\cdots),\\
A_N(\cdots,j+1,\cdots,j,\cdots)&=\frac{k^{(x_N)}-\Omega/v-i\Gamma/(2v)}{k^{(x_N)}-\Omega/v+i\Gamma/(2v)}A_{N+1}(\cdots,j+1,\cdots,j,\cdots)=t_{k^{(x_N)}}A_{N+1}(\cdots,j+1,\cdots,j,\cdots),
\end{aligned} \tag{A.5}$$

where $k^{(x_N)}$ is the k that is multiplied with x_N in the exponentials. These two equations indicate that the coefficients between the two neighboring subregions only deviate by a single-photon transmission amplitude $t_{k^{(x_N)}}$ (see Eq. 4.22). Moreover, by dividing these two equations, we get

$$\frac{A_N(\cdots,j,\cdots,j+1,\cdots)}{A_N(\cdots,j+1,\cdots,j,\cdots)}=\frac{A_{N+1}(\cdots,j,\cdots,j+1,\cdots)}{A_{N+1}(\cdots,j+1,\cdots,j,\cdots)}. \tag{A.6}$$

In the following, by repeating the same procedure to other boundaries where x_{N-1}, x_{N-2}, $\cdots$, and x_{j+2} cross from 0^- to 0^+ one by one, we obtain similar relations

$$\frac{A_{j+2}(\cdots,j,\cdots,j+1,\cdots)}{A_{j+2}(\cdots,j+1,\cdots,j,\cdots)}=\cdots=\frac{A_{N-1}(\cdots,j,\cdots,j+1,\cdots)}{A_{N-1}(\cdots,j+1,\cdots,j,\cdots)}=\frac{A_N(\cdots,j,\cdots,j+1,\cdots)}{A_N(\cdots,j+1,\cdots,j,\cdots)}. \tag{A.7}$$

Such a relation is anticipated, as the k's associated with the coordinates that cross the boundaries are the same.

For the next boundary between subregion $j+2$ and subregion $j+1$ where x_{j+1} crosses from 0^- to 0^+, the coefficient relations between the neighboring subregions can also be computed:

$$A_{j+1}(\cdots,j,\cdots,j+1,\cdots)=\frac{k_n-\Omega/v-i\Gamma/(2v)}{k_n-\Omega/v+i\Gamma/(2v)}A_{j+2}(\cdots,j,\cdots,j+1,\cdots)=t_{k_n}A_{j+2}(\cdots,j,\cdots,j+1,\cdots),$$
$$A_{j+1}(\cdots,j+1,\cdots,j,\cdots)=\frac{k_m-\Omega/v-i\Gamma/(2v)}{k_m-\Omega/v+i\Gamma/(2v)}A_{j+2}(\cdots,j+1,\cdots,j,\cdots)=t_{k_m}A_{j+2}(\cdots,j+1,\cdots,j,\cdots). \tag{A.8}$$

We note that different from the previous case, this time, the k's associated with x_{j+1} are different for the two terms. Thus, Eq. A.8 does not yield the same relation that follows the rule in Eq. A.7. Moreover, the $(N-1)$-photon wavefunction with the photon labeled by $j+1$ being absorbed by the atom is also computed,

$$\begin{aligned}&e(x_1,x_2,\cdots,x_{j-1},x_j,x_{j+2},\cdots,x_N)\\&=\sqrt{N}(V/v)[\frac{e^{i(\cdots+k_mx_j+\cdots)}}{k_n-\Omega/v+i\Gamma/(2v)}A_{j+2}(\cdots,j,\cdots,j+1,\cdots)+\frac{e^{i(\cdots+k_nx_j+\cdots)}}{k_m-\Omega/v+i\Gamma/(2v)}A_{j+2}(\cdots,j+1,\cdots,j,\cdots)].\end{aligned} \tag{A.9}$$

For the next boundary between subregion $N-1$ and region $N-2$ where x_j increases from 0^- to 0^+, we obtain

$$A_j(\cdots,j,\cdots,j+1,\cdots)=\frac{k_m-\Omega/v-i\Gamma/(2v)}{k_m-\Omega/v+i\Gamma/(2v)}A_{j+1}(\cdots,j,\cdots,j+1,\cdots)=t_{k_m}A_{j+1}(\cdots,j,\cdots,j+1,\cdots),$$
$$A_j(\cdots,j+1,\cdots,j,\cdots)=\frac{k_n-\Omega/v-i\Gamma/(2v)}{k_n-\Omega/v+i\Gamma/(2v)}A_{j+1}(\cdots,j+1,\cdots,j,\cdots)=t_{k_n}A_{j+1}(\cdots,j+1,\cdots,j,\cdots), \tag{A.10}$$

and the $(N-1)$-photon wavefunction with the photon labeled by j being absorbed is

$$\begin{aligned}&e(x_1,x_2,\cdots,x_{j-1},x_{j+1},x_{j+2},\cdots,x_N)\\&=\sqrt{N}(V/v)[\frac{e^{i(\cdots+k_nx_{j+1}+\cdots)}}{k_m-\Omega/v+i\Gamma/(2v)}A_{j+1}(\cdots,j,\cdots,j+1,\cdots)+\frac{e^{i(\cdots+k_mx_{j+1}+\cdots)}}{k_n-\Omega/v+i\Gamma/(2v)}A_{j+1}(\cdots,j+1,\cdots,j,\cdots)].\end{aligned} \tag{A.11}$$

Therefore, Eq. A.9 and Eq. A.11 represent the expressions for the $(N-1)$-photon wavefunction in two neighbouring subregions. Since this wavefunction is continuous everywhere in

the entire space (see Eq. 4.6), the self-consistency of the function requirers

$$e(x_1, x_2, \cdots, x_{j-1}, 0^-, x_{j+2}, \cdots, x_N) = e(x_1, x_2, x_{j-1}, 0^+, x_{j+2}, \cdots, x_N), \tag{A.12}$$

which immediately leads to

$$A_{j+2}(\cdots, j, \cdots, j+1, \cdots)/A_{j+2}(\cdots, j+1, \cdots, j, \cdots) = (k_m - k_n - i\Gamma/v)/(k_m - k_n + i\Gamma/v). \tag{A.13}$$

By combining Eq. A.13 with all the previous obtained coefficient relations (Eq. A.6 and Eq. A.7), we finally get

$$A_{N+1}(\cdots, j, \cdots, j+1, \cdots)/A_{N+1}(\cdots, j+1, \cdots, j, \cdots) = (k_m - k_n - i\Gamma/v)/(k_m - k_n + i\Gamma/v). \tag{A.14}$$

It is worth mentioning here that the above analysis does not yield any restrictions on the wave number k's. Thus, the eigenstate wavefunction $f(x_1, x_2, \cdots, x_N)$ is uniquely determined as:

$$f(x_1, x_2, \cdots, x_N) \propto \begin{cases} \sum_{\mathcal{P}\in S_N}\{\prod_{m<n}[k_m - k_n - i\Gamma \mathrm{sgn}(\mathcal{P}_n - \mathcal{P}_m)/v]\} \exp(i\sum_{j=1}^N k_j x_{\mathcal{P}_j}), \\ \quad \text{in subregion } N+1 \quad (x_1 < x_2 < \cdots < x_N < 0), \\ \qquad\qquad \cdots \\ \qquad\qquad \cdots \\ \qquad\qquad \cdots \\ (\prod_{j=1}^N t_{k_j}) \sum_{\mathcal{P}\in S_N}\{\prod_{m<n}[k_m - k_n - i\Gamma \mathrm{sgn}(\mathcal{P}_n - \mathcal{P}_m)/v]\} \exp(i\sum_{j=1}^N k_j x_{\mathcal{P}_j}), \\ \quad \text{in subregion } 1 \quad (0 < x_1 < x_2 < \cdots < x_N), \end{cases} \tag{A.15}$$

which describes an N-photon extended state, as each exponential term represents a free plane wave without restriction. The corresponding in-state wavefunction $f_{\text{in}}(x_1, x_2, \cdots, x_N)$

is expressed by extending $f(x_1, x_2, \cdots, x_N)$ in subregion $N+1$ to the entire space ($-\infty < x_1, x_2, \cdots, x_N < +\infty$),

$$f_{\text{in}}(x_1, x_2, \cdots, x_N) = C_N \sum_{\mathcal{P}\in S_N} \{\prod_{m<n} [k_m - k_n - i\Gamma \text{sgn}(x_{\mathcal{P}_n} - x_{\mathcal{P}_m})/v]\} \exp(i \sum_{j=1}^{N} k_j x_{\mathcal{P}_j}), \quad \text{(A.16)}$$

with normalization constant C_N to be determined. The corresponding out-state wavefunction $f_{\text{out}}(x_1, x_2, \cdots, x_N)$, on the other hand, can be expressed by extending $f(x_1, x_2, \cdots, x_N)$ in subregion 1 to the entire space and is conveniently written as

$$f_{\text{out}}(x_1, x_2, \cdots, x_N) = (\prod_{j=1}^{N} t_{k_j}) f_{\text{in}}(x_1, x_2, \cdots, x_N). \quad \text{(A.17)}$$

A.2 N-photon Bound State

Till now, we have constructed the N-photon extended states, which are indeed the eigenstates of the Hamiltonian H_e. Nonetheless, it turns out that the N-photon extended states do not form a complete set in the N-photon Hilbert space $\mathcal{H}_e^{\otimes N}$. To find out those missing eigenstates, one needs to extend the wave numbers k's into complex values. As all k's sum up to be a real number, to avoid the divergence, some of the coefficients A's must be zero. The extreme case is that only one coefficient A is left to be nonzero, and all the k's are assumed to be complex numbers $\{k_j = k'_j + i\kappa_j\}, j = 1, \cdots, N$, where k'_j is the real part and

κ_j is the imaginary part.

$$f(x_1, x_2, \cdots, x_N) = \begin{cases} A_{N+1} e^{i(k'_1+i\kappa_1)x_1+i(k'_2+i\kappa_2)x_2+\cdots+i(k'_N+i\kappa_N)x_N}, \\ \quad \text{in subregion } N+1 \quad (x_1 < x_2 < \cdots < x_N < 0), \\ A_N e^{i(k'_1+i\kappa_1)x_1+i(k'_2+i\kappa_2)x_2+\cdots+i(k'_N+i\kappa_N)x_N}, \\ \quad \text{in subregion } N \quad (x_1 < x_2 < \cdots < x_{N-1} < 0 < x_N), \\ \qquad \cdots \\ \qquad \cdots \\ \qquad \cdots \\ A_1 e^{i(k'_1+i\kappa_1)x_1+i(k'_2+i\kappa_2)x_2+\cdots+i(k'_N+i\kappa_N)x_N}, \\ \quad \text{in subregion } 1 \quad (0 < x_1 < x_2 < \cdots < x_N). \end{cases} \tag{A.18}$$

With this wavefuntion, one can apply exactly the same procedures at all the boundaries to obtain all the constraints regarding to the A's and k's. At the first boundary between subregion $N+1$ and subregion N where x_N crosses from 0^- to 0^+, the equations of motion yield the following coefficient relation

$$A_N = \frac{k'_N + i\kappa_N - \Omega/v - i\Gamma/(2v)}{k'_N + i\kappa_N - \Omega/v + i\Gamma/(2v)} A_{N+1} = t_{k_N} A_{N+1}, \tag{A.19}$$

which has exactly the same form as before. Moreover, the $(N-1)$-photon wavefunction with the photon labeled by N being absorbed is obtained accordingly:

$$e(x_1, x_2, \cdots, x_{N-1}) = \sqrt{N}(V/v)[\frac{e^{i(k'_1+i\kappa_1)x_1+i(k'_2+i\kappa_2)x_2+\cdots+i(k'_{N-1}+i\kappa_{N-1})x_{N-1}}}{k'_N + i\kappa_N - \Omega/v + i\Gamma/(2v)} A_{N+1}]. \tag{A.20}$$

At the next boundary between subregion N and subregion $N-1$ where x_{N-1} crosses from 0^- to 0^+, the equations of motion also yield similar coefficient relation

$$A_{N-1} = \frac{k'_{N-1} + i\kappa_{N-1} - \Omega/v - i\Gamma/(2v)}{k'_{N-1} + i\kappa_{N-1} - \Omega/v + i\Gamma/(2v)} A_N = t_{k_{N-1}} A_N, \tag{A.21}$$

and the $(N-1)$-photon wavefunction with the photon labeled by $N-1$ being absorbed is given by

$$e(x_1, x_2, \cdots, x_{N-2}, x_N) = \sqrt{N}(V/v)[\frac{e^{i(k'_1+i\kappa_1)x_1 + i(k'_2+i\kappa_2)x_2 + \cdots + i(k'_{N-2}+i\kappa_{N-2})x_{N-2} + i(k'_N+i\kappa_N)x_N}}{k'_{N-1} + i\kappa_{N-1} - \Omega/v + i\Gamma/(2v)} A_N]. \tag{A.22}$$

Again, by applying the self-consistent condition

$$e(x_1, x_2, \cdots, x_{N-2}, 0^-) = e(x_1, x_2, \cdots, x_{N-2}, 0^+), \tag{A.23}$$

we get

$$k'_{N-1} = k'_N, \tag{A.24}$$

and

$$\kappa_N = \kappa_{N-1} + \Gamma/v. \tag{A.25}$$

This procedure can be repeated for the rest of the boundaries, and we finally get:

$$k'_N = k'_{N-1} = \cdots = k'_1 \equiv k, \tag{A.26}$$

and

$$\kappa_N = \kappa_{N-1} + \Gamma/v = \kappa_{N-2} + 2\Gamma/v = \cdots = \kappa_1 + (N-1)\Gamma/v. \tag{A.27}$$

As the summation of all the k's is a real number, $\kappa_1 = -(N-1)\Gamma/(2v)$. Thus, the N k's are given by

$$k_j = k + [2j - (N+1)]\Gamma/(2v), \tag{A.28}$$

where $j = 1, 2, \cdots, N$. With those k's, the eigenstate wavefunction is uniquely determined:

$$f(x_1, x_2, \cdots, x_N) \propto \begin{cases} e^{ik(x_1+x_2+\cdots+x_N)-(N-1)\Gamma(x_N-x_1)/(2v)-(N-3)\Gamma(x_{N-1}-x_2)/(2v)-\cdots}, \\ \quad \text{in subregion } N+1 \quad (x_1 < x_2 < \cdots < x_N < 0), \\ \qquad \cdots \\ \qquad \cdots \\ \qquad \cdots \\ (\prod_{j=1}^{N} t_{k_j}) e^{ik(x_1+x_2+\cdots+x_N)-(N-1)\Gamma(x_N-x_1)/(2v)-(N-3)\Gamma(x_{N-1}-x_2)/(2v)-\cdots}, \\ \quad \text{in subregion } 1 \quad (0 < x_1 < x_2 < \cdots < x_N), \end{cases} \tag{A.29}$$

which describes an N-photon bound state, as the wavefunction is exponentially suppressed when the relative distances between any two coordinates increase. The plane wave component $e^{ik(x_1+x_2+\cdots+x_N)}$ in the wavefunction, on the other hand, indicates that the N-photon bound state can propagate in the entire space freely as a whole. Having constructed the N-photon bound state, its corresponding in-state wavefunction $f_{\text{in}}(x_1, x_2, \cdots, x_N)$ can then be obtained by extending $f(x_1, x_2, \cdots, x_N)$ in subregion $N+1$ to the entire space

$$f_{\text{in}}(x_1, x_2, \cdots, x_N) = C_N e^{ik(x_1+x_2+\cdots+x_N)-(\sum_{m<n}|x_m-x_n|)\Gamma/(2v)}, \tag{A.30}$$

where C_N is the normalization constant to be determined. The out-state wavefunction $f_{\text{out}}(x_1, x_2, \cdots, x_N)$, on the other hand, possesses the same expression as that in Eq. A.17.

A.3 Other Hybrid States

Except for the two types of eigenstates presented above, the rest types of eigenstates can be constructed in a similar manner by postulating different number of nonzero A's in the

wavefunction. Nonetheless, most cases do not yield a solution. For those cases that do permit a valid eigenstate, the choices of the nonzero A's are unique. Thus, a unique set of k's is obtained, which in turn defines the types of eigenstates. Remarkably, it turns out that there exists an one-to-one mapping between the types of N-photon eigenstates and the partitions of the integer number N (shown in Tab. 4.4), which illustrates how many nonzero terms exist in a certain types of eigenstates. For example, for $N = 4$, $(2, 2)$ is one of the partitions, and by assuming $4!/[2!2!] = 3$ nonzero terms in the wavefunction, we can construct the type-3 eigenstate in Tab. 4.3. Also, $(3, 1)$ is another partition, and by assuming $4!/[3!1!] = 4$ nonzero terms in the wavefunction, we can construct type-4 eigenstate in Tab. 4.3. In general, to construct a certain type of eigenstates that corresponds to the partition $N = N_1 + N_2 + \cdots$, the number of nonzero terms in the eigenstate wavefunction is given by $N!/[N_1!N_2!\cdots]$.

Appendix B

The Normalization Conditions

In this Appendix, we employ the delta normalization condition to normalize the wavefunctions of the in-states in the chiral case, with definitions shown as follows:

B.1 1-photon Case

The in-state wavefunction has only one specific form,

$$f_{\text{in}}^{(k)}(x) = C_1 e^{ikx}, \tag{B.1}$$

where we add a superscript k to denote only one real parameter that characterizes this wavefunction. To normalize this wavefunction, we compute the overlap between two such kind of wavefunctions with different superscripts,

$$\int_{-\infty}^{+\infty} dx f_{\text{in}}^{(k')*}(x) f_{\text{in}}^{(k)}(x) = |C_1|^2 2\pi\delta(k-k'), \tag{B.2}$$

where the symbol $(*)$ represents the complex conjugate of the function. In the integration, the following identity is used,

$$\int_{-\infty}^{+\infty} dx\, e^{-ik'x} e^{ikx} = 2\pi\delta(k-k'). \tag{B.3}$$

Thus, the normalization constant C_1 is set to be $1/\sqrt{2\pi}$ so that $f_{\rm in}^{(k)}(x)/\sqrt{2\pi}$ is normalized to the delta function.

B.2 2-photon Case

The 2-photon extended state with wavefunction $f_{\rm in}^{(k_1,k_2)}(x_1,x_2)$ (Eq. 4.12) is characterized by two real parameters (k_1,k_2). Similarly, we compute the overlap between the wavefunctions with different superscripts,

$$\int_{-\infty}^{+\infty}\int_{-\infty}^{+\infty} dx_1 dx_2 f_{\rm in}^{(k_1',k_2')*}(x_1,x_2) f_{\rm in}^{(k_1,k_2)}(x_1,x_2) = |C_2|^2 8\pi^2[(k_1-k_2)^2+(\Gamma/v)^2]\delta(k_1-k_1')\delta(k_2-k_2'). \tag{B.4}$$

To avoid double counting, we restrict $k_1<k_2$ and $k_1'<k_2'$. Thus, the normalization constant C_2 is set to be $[(k_1-k_2)^2+(\Gamma/v)^2]^{-1/2}/(2\sqrt{2}\pi)$.

Another type of in-states to be normalized is the 2-photon bound state with wavefunction $f_{\rm in}^{(k)}(x_1,x_2)$ (Eq. 4.13), which is characterized by only one real parameter k. A direct computation reveals that,

$$\int_{-\infty}^{+\infty}\int_{-\infty}^{+\infty} dx_1 dx_2 f_{\rm in}^{(k')*}(x_1,x_2) f_{\rm in}^{(k)}(x_1,x_2) = |C_2|^2 \frac{2\pi v}{\Gamma}\delta(k-k'). \tag{B.5}$$

Thus, $C_2=\sqrt{\Gamma/(2\pi v)}$.

B.3 3-photon Case

The first type is the 3-photon extended state with wavefunction $f_{\rm in}^{(k_1,k_2,k_3)}(x_1,x_2,x_3)$ (Eq. 4.14), which is characterized by three real parameters (k_1,k_2,k_3). A direct computation reveals that,

$$\begin{aligned}&\int_{-\infty}^{+\infty}\int_{-\infty}^{+\infty}\int_{-\infty}^{+\infty}dx_1dx_2dx_3 f_{\rm in}^{(k_1',k_2',k_3')*}(x_1,x_2,x_3)f_{\rm in}^{(k_1,k_2,k_3)}(x_1,x_2,x_3)\\&=|C_3|^2 48\pi^3[(k_1-k_2)^2+(\Gamma/v)^2][(k_1-k_3)^2+(\Gamma/v)^2][(k_2-k_3)^2+(\Gamma/v)^2]\delta(k_1-k_1')\delta(k_2-k_2')\delta(k_3-k_3'),\end{aligned} \tag{B.6}$$

where we restrict $k_1<k_2<k_3$ and $k_1'<k_2'<k_3'$ to avoid double counting. Thus, C_3 is set to be $\left\{48\pi^3\left[(k_1-k_2)^2+(\Gamma/v)^2\right]\left[(k_2-k_3)^2+(\Gamma/v)^2\right]\left[(k_1-k_3)^2+(\Gamma/v)^2\right]\right\}^{-1/2}$.

The second type is the hybrid state $f_{\rm in}^{(k,k_3)}(x_1,x_2,x_3)$, characterized by two real parameters k and k_3, which is obtained by adding other 15 terms by permuting x_1,x_2, and x_3 in Eq. 4.15 . Similarly, we compute the overlap between the wavefunctions with different superscripts

$$\begin{aligned}&\int_{-\infty}^{+\infty}\int_{-\infty}^{+\infty}\int_{-\infty}^{+\infty}dx_1dx_2dx_3 f_{\rm in}^{(k',k_3')*}(x_1,x_2,x_3)f_{\rm in}^{(k,k_3)}(x_1,x_2,x_3)\\&=|C_3|^2(12\pi^2v/\Gamma)\left[(k-k_3)^2+[\Gamma/(2v)]^2\right]\left[(k-k_3)^2+[3\Gamma/(2v)]^2\right]\delta(k-k')\delta(k_3-k_3')+\cdots,\end{aligned} \tag{B.7}$$

where '$\cdots$' denotes terms that containing less than two delta functions. For the normalization purpose, only the most singular term is kept. Thus, C_3 is set to be $\sqrt{\Gamma/(12\pi^2v)}\left\{\left[(k-k_3)^2+[\Gamma/(2v)]^2\right]\left[(k-k_3)^2+[3\Gamma/(2v)]^2\right]\right\}^{-1/2}$.

The third type is the 3-photon bound state with wavefunction $f_{\rm in}^{(k)}(x_1,x_2,x_3)$ (Eq. 4.16), which is characterized by only one real parameter k. A direct computation reveals that,

$$\int_{-\infty}^{+\infty}\int_{-\infty}^{+\infty}dx_1dx_2dx_3 f_{\rm in}^{(k')*}(x_1,x_2,x_3)f_{\rm in}^{(k)}(x_1,x_2,x_3)=|C_3|^2\frac{\pi v^2}{\Gamma^2}\delta(k-k'). \tag{B.8}$$

Thus, $C_3=\Gamma/(v\sqrt{\pi})$.

B.4 N-photon Case

The wavefunction of the N-photon extended state is $f_{\rm in}^{(k_1,k_2,\cdots,k_N)}(x_1,x_2,\cdots,x_N)$ (Eq. 4.17), which is characterized by N real parameters $(k_1,k_2,\cdots,k_N)$. A direct computation reveals that ($k_1<k_2<\cdots<k_N$ and $k_1'<k_2'<\cdots<k_N'$ are restricted to avoid double counting),

$$\begin{aligned}&\int_{-\infty}^{+\infty}\cdots\int_{-\infty}^{+\infty}dx_1dx_2\cdots dx_N f_{\rm in}^{(k_1',k_2',\cdots,k_N')*}(x_1,x_2,\cdots,x_N)f_{\rm in}^{(k_1,k_2,\cdots,k_N)}(x_1,x_2,\cdots,x_N)\\&=|C_N|^2\{\prod_{m<n}[(k_m-k_n)^2+(\Gamma/v)^2]\}N!(2\pi)^N\delta(k_1-k_1')\delta(k_2-k_2')\cdots\delta(k_N-k_N').\end{aligned}\tag{B.9}$$

Thus, $C_N=\{\prod_{m<n}[(k_m-k_n)^2+(\Gamma/v)^2]\}^{-1/2}/(\sqrt{N!(2\pi)^N}$. In contrast, the wavefunction of the N-photon bound state $f_{\rm in}^{(k)}(x_1,x_2,\cdots,x_N)$ (Eq. 4.19), which is characterized by only one real parameter k. A direct computation reveals that,

$$\begin{aligned}&\int_{-\infty}^{+\infty}\cdots\int_{-\infty}^{+\infty}dx_1dx_2\cdots dx_N f_{\rm in}^{(k')*}(x_1,x_2,\cdots,x_N)f_{\rm in}^{(k)}(x_1,x_2,\cdots,x_N)\\&=|C_N|^2\frac{2\pi}{(N-1)!(\Gamma/v)^{N-1}}\delta(k-k').\end{aligned}\tag{B.10}$$

Thus, $C_N=\sqrt{(N-1)!(\Gamma/v)^{N-1}/(2\pi)}$. The normalization constants for other hybrid states can be determined through a similar procedure.

Appendix C

Completeness Check

The construction of the scattering matrix relies on the the completeness of the set of in-states $\{|\text{in}\rangle\}$ in the chiral space. In the chiral space, the completeness condition is expressed as the following identity,

$$\sum_j \sum_{\{k\}} |\text{in}_j^{\{k\}}\rangle\langle\text{in}_j^{\{k\}}| = I, \tag{C.1}$$

where the subscript $j = 1, 2, \cdots, Z(N)$ accounts for all the types of the in-states and the set $\{k\}$ is for all the possible k's in a given type. In this appendix, we provide a numerical check for the completeness for the chiral case, that is we will check if the equality in Eq. C.1 holds. This procedure can be straightforwardly generalized to the non-chiral case without further conceptual difficulties.

As all the in-states are given in real-space forms, we first project an arbitrary N-photon state $|X\rangle$ into the real space, which is also chosen to be normalized as

$$\int \cdots \int dx_1 \cdots dx_N |\langle x_1, \cdots, x_N | X\rangle|^2 = 1. \tag{C.2}$$

Then, by inserting the to-be-checked Eq. C.1 into Eq. C.2, we get

$$\sum_j P_j \stackrel{?}{=} 1, \tag{C.3}$$

where

$$P_j \equiv \sum_{\{k\}} \int \cdots \int dx_1 \cdots dx_N \left| \langle x_1, \cdots, x_N | \mathrm{in}_j^{\{k\}} \rangle \langle \mathrm{in}_j^{\{k\}} | X \rangle \right|^2, \tag{C.4}$$

describing the weight of $|X\rangle$ in the j-th type in-states. When writing down Eq. C.3 and Eq. C.4, we have used the fact that the in-states with different j and set $\{k\}$ are orthogonal with each other. The orthogonality can either be proved by standard procedures or directly be checked numerically.

As a concrete example, we numerically check the in-states in $\mathcal{H}_e^{\otimes 3}$. The incoming 3-photon Fock state $|X\rangle$ is assumed to be three identical and overlapping gaussian wave packets, characterized by standard deviation σ_x. Tab. C.1 lists all the P_j's for varying σ_x. As we can see from the table that, for all σ_x investigated, the summations of all the P_j's are very close to unity, with relative error less than 1%. Such a result numerically confirms both the completeness and orthogonality of the 3-photon in-states in $\mathcal{H}_e^{\otimes 3}$.

Table C.1: Completeness check for in-states in $\mathcal{H}_e^{\otimes 3}$. To ease the computational burden, for the purpose of checking completeness, σ_x is smaller than that used in previous section, where a much larger σ_x is required for near single frequency condition.

$\sigma_x/v\tau_r$	P_1	P_2	P_3	summation
0.5	0.008	0.052	0.941	1.001
1	0.017	0.163	0.821	1.001
2	0.033	0.566	0.393	0.992

Appendix D

Photon Correlation Functions to Arbitrary Order

In this Appendix, we give a complete derivations to the photon correlation functions to arbitrary order. We start by describing the second-order correlation function, which is commonly used in many research papers. The second-order correlation function, which is the primary quantity to describe the statistical properties of a stream of photons, is defined as [131]:

$$g^{(2)}(x_0, t, t+\tau) = \frac{\langle E^-(x_0,t)E^-(x_0,t+\tau)E^+(x_0,t+\tau)E^+(x_0,t)\rangle}{\langle E^-(x_0,t)E^+(x_0,t)\rangle\langle E^-(x_0,t+\tau)E^+(x_0,t+\tau)\rangle}, \tag{D.1}$$

where $\langle\cdot\rangle$ is the expectation value of a normalized state, and $E^-(x_0,t)$ and $E^+(x_0,t)$ are the positive and negative frequency components, respectively, of the electric field operators. t and $t+\tau$ are the two times to make the measurements and x_0 is the position of the detector. By using the real-space approach presented above, it can be shown that the second-order correlation function can be reduced to [132]:

$$g_i^{(2)}(\tau) = \frac{\langle C_i^\dagger(x_0)C_i^\dagger(x_0+v\tau)C_i(x_0+v\tau)C_i(x_0)\rangle}{\langle C_i^\dagger(x_0)C_i(x_0)\rangle\langle C_i^\dagger(x_0+v\tau)C_i(x_0+v\tau)\rangle}, \tag{D.2}$$

where $i = R$ or L represents the measurements for the right moving photons or the left moving photons, respectively. For incoming photons from the left, if $x_0 > 0$, the detector is placed on the transmitted side, which only registers the right moving photons in the transmitted scattered state; on the other hand, if $x_0 < 0$, the detector is placed on the reflected side, which register the right moving photons in the input state and the left moving photons in the reflected scattered state. In principle, the correlation function does not depend on the placement of the detector, i.e., x_0. Analytically, we found out it is indeed so; numerically, we found there exists very minute difference. For brevity, hereafter, we drop the subscript 'i' in the correlation function.

Eq. D.2 can be further expressed in terms of the wavefunction transmitted or reflected part of the scattered state. For example, the second-order correlation function for a 2-photon state, now takes the following form:

$$g^{(2)}(\tau) = \frac{1}{2}\left[\iint dx_1 dx_2 |h(x_1, x_2)|^2\right] \frac{|h(x_0, x_0 + v\tau)|^2}{\left[\int dx_2 |h(x_0, x_2)|^2\right]\left[\int dx_1 |h(x_1, x_0 + v\tau)|^2\right]}, \tag{D.3}$$

where $h(x_1, x_2)$ is the 2-photon wavefunction of the relevant state. Using a similar approach, the second-order correlation function for a 3-photon state can also be written as:

$$g^{(2)}(\tau) = \frac{2}{3}\left[\iiint dx_1 dx_2 dx_3 |h(x_1, x_2, x_3)|^2\right] \frac{\int dx_3 |h(x_0, x_0 + v\tau, x_3)|^2}{\left[\int\int dx_2 dx_3 |h(x_0, x_2, x_3)|^2\right]\left[\int\int dx_1 dx_3 |h(x_1, x_0 + v\tau, x_3)|^2\right]}, \tag{D.4}$$

where $h(x_1, x_2, x_3)$ is the 3-photon wavefunction of the relevant state. Such a procedure can be further generalized to the N-photon state, and its second-order correlation function is

$$g^{(2)}(\tau) = \frac{N-1}{N}\left[\int \cdots \int dx_1 \cdots dx_N |h(x_1, x_2, \cdots, x_N)|^2\right] \times \frac{\int \cdots \int dx_3 \cdots dx_N |h(x_0, x_0 + v\tau, x_3, \cdots, x_N)|^2}{\left[\int \cdots \int dx_2 \cdots dx_N |h(x_0, x_2, \cdots, x_N)|^2\right]\left[\int \cdots \int dx_1 dx_3 \cdots dx_N |h(x_1, x_0 + v\tau, x_3, \cdots, x_N)|^2\right]}, \tag{D.5}$$

where $h(x_1, x_2, \cdots, x_N)$ is the N-photon wavefunction of the relevant state.

Moreover, the higher-order correlation functions can also be obtained in a similar manner. For example, the third-order correlation function for a 3-photon state is

$$g^{(3)}(\tau_1,\tau_2) = \frac{2}{9}\left[\iiint dx_1dx_2dx_3|h(x_1,x_2,x_3)|^2\right]^2 \times \frac{|h(x_0,x_0+v\tau_1,x_0+v\tau_2)|^2}{\left[\iint dx_2dx_3|h(x_0,x_2,x_3)|^2\right]\left[\iint dx_1dx_3|h_i(x_1,x_0+v\tau_1,x_3)|^2\right]\left[\iint dx_1dx_2|h(x_1,x_2,x_0+v\tau_2)|^2\right]}, \tag{D.6}$$

where τ_1 and τ_2 are the differences of the three arrival times of the photons. Similarly, the m-th order correlation function for an N-photon state ($m \leq N$) is

$$g^{(m)}(\tau_1,\cdots,\tau_{m-1}) = \frac{N!}{(N-m)!N^m}\left[\int\cdots\int dx_1\cdots dx_N|h(x_1,x_2,\cdots,x_N)|^2\right]^{m-1} \times \frac{\int\cdots\int dx_{m+1}\cdots dx_N|h(x_0,x_0+v\tau_1,x_0+v\tau_2,\cdots,x_0+v\tau_{m-1},x_{m+1},\cdots,x_N)|^2}{\left[\int\cdots\int dx_2\cdots dx_N|h(x_0,x_2,\cdots,x_N)|^2\right]\cdots\left[\int\cdots\int dx_1\cdots dx_{m-1}dx_{m+1}\cdots dx_N|h(x_1,\cdots,x_{m-1},x_0+v\tau_{m-1},x_{m+1},\cdots,x_N)|^2\right]}, \tag{D.7}$$

where $\tau_1,\tau_2,\cdots,\tau_{m-1}$ are differences of the m arrival times of the photons.

Among all the correlation functions presented above, the second- and third-order correlation functions for the 3-photon state are of particular interests and discussed in section 5. To simplify the expressions, one can define

$$|\phi(x)|^2 \equiv \iint dx_2dx_3|h(x,x_2,x_3)|^2, \tag{D.8}$$

and

$$P \equiv \iiint dx_1dx_2dx_3|h(x_1,x_2,x_3)|^2 = \int dx_1|\phi(x_1)|^2. \tag{D.9}$$

The first quantity $|\phi(x)|^2$ describes the probability of finding one photon at position x regardless of the positions of the other two photons. The second quantity P is the total probability of the 3-photon state in the entire space. Thus, the correlation functions can be further simplified as

$$g^{(2)}(\tau) = \frac{2}{3}P\frac{\int dx_3|h(x_0,x_0+v\tau,x_3)|^2}{|\phi(x_0)|^2|\phi(x_0+v\tau)|^2}, \tag{D.10}$$

and

$$g^{(3)}(\tau_1,\tau_2)=\frac{2}{9}P^2\frac{|h(x_0,x_0+v\tau_1,x_0+v\tau_2)|^2}{|\phi(x_0)|^2||\phi(x_0+v\tau_1)|^2||\phi(x_0+v\tau_2)|^2|}. \tag{D.11}$$

Numerically, we found that the above exact expressions can be computational extensive when small denominators are present, which occur when $|\phi(x)|^2$ is small (e.g. at the edge of the wavepacket). To ease the computational expense, we perform the following trick by integration over x_0 for both numerators and denominators independently (note the analytic result is independent of x_0). Such a procedure numerically gets away with the small denominator problem, and results in the following expressions used in the article:

$$g^{(2)}(\tau)=\frac{2}{3}P\frac{\iint dx_0dx_3|h(x_0,x_0+v\tau,x_3)|^2}{\int dx_0|\phi(x_0)|^2|\phi(x_0+v\tau)|^2}, \tag{D.12}$$

and

$$g^{(3)}(\tau_1,\tau_2)=\frac{2}{9}P^2\frac{\int dx_0|h(x_0,x_0+v\tau_1,x_0+v\tau_2)|^2}{\int dx_0|\phi(x_0)|^2|\phi(x_0+v\tau_1)|^2|\phi(x_0+v\tau_2)|^2}. \tag{D.13}$$

Appendix E

Extended Mie Theory for the Two-layer Microsphere

In this Appendix, we provide sufficient mathematical details for an extended Mie theory for two-layer microsphere. We assume that the incident light is an x-polarized plane wave with an amplitude E_0 propagating along the z-direction, and can be written as

$$\mathbf{E}_i = E_0 e^{ikr\cos\theta}\mathbf{e}_x, \tag{E.1}$$

where

$$\mathbf{e}_x = \sin\theta\cos\phi\,\mathbf{e}_r + \cos\theta\cos\phi\,\mathbf{e}_\theta - \sin\phi\,\mathbf{e}_\phi. \tag{E.2}$$

Such a incident field can also be expanded using the vector spherical harmonics $\mathbf{M}$ and $\mathbf{N}$ (each of which is a function of the spherical coordinates r, θ, ϕ) [37] as follows:

$$\mathbf{E}_i = \sum_{n=1}^{\infty}(\mathbf{M}_{o1n}^{(1)} - i\mathbf{N}_{e1n}^{(1)})E_n. \tag{E.3}$$

where r is the radial coordinate and $E_n = i^n E_0(2n+1)/n(n+1)$. In the vector spherical harmonics, the subscripts e and o denote even and odd modes, respectively; 1 is the azimuthal

order, and n is the order of vector spherical harmonics. Each of the superscripts from $(1)-(3)$ corresponds to the appropriate choice of one of the four kinds of spherical Bessel functions.

On the other hand, the scattered electric field $\mathbf{E}_s$ in the region $r > R_s$ can also be described as linear combinations of vector spherical harmonics, as follows

$$\mathbf{E}_s = \sum_{n=1}^{\infty} (ia_n \mathbf{N}_{e1n}^{(3)} - b_n \mathbf{M}_{o1n}^{(3)}) E_n. \tag{E.4}$$

Similarly, we can write out the electric field inside the two-layer microsphere using the vector spherical harmonics accordingly. For example, the electric field for the core part ($r < R_c$) is:

$$\mathbf{E}_1 = \sum_{n=1}^{\infty} (c_n \mathbf{M}_{o1n}^{(1)} - id_n \mathbf{N}_{e1n}^{(1)}) E_n, \tag{E.5}$$

while the electric field for the shell part is:

$$\mathbf{E}_2 = \sum_{n=1}^{\infty} (f_n \mathbf{M}_{o1n}^{(1)} - ig_n \mathbf{N}_{e1n}^{(1)} + v_n \mathbf{M}_{o1n}^{(2)} - iw_n \mathbf{N}_{e1n}^{(2)}) E_n. \tag{E.6}$$

With the field expressions, the boundary conditions at $r = R_c$ and $r = R_s$ require the tangential components ($\mathbf{e}_\theta$ and $\mathbf{e}_\phi$ of both the electric field and magnetic field to be continuous. Therefore, eight equations that connects the coefficients $\{a_n, b_n, c_n, d_n, f_n, g_n, v_n, w_n\}$

are obtained as follows:

$$\begin{aligned}
f_n m_1 \psi_n(m_2 x) - v_n m_1 \chi_n(m_2 x) - c_n m_2 \psi_n(m_1 x) = 0, \\
w_n m_1 \chi_n'(m_2 x) - g_n m_1 \psi_n'(m_2 x) + d_n m_2 \psi_n'(m_1 x) = 0, \\
v_n \chi_n'(m_2 x) - f_n \psi_n'(m_2 x) + d_n m_2 \psi_n'(m_1 x) = 0, \\
g_n \psi_n(m_2 x) - w_n \chi_n(m_2 x) - d_n \psi_n(m_1 x) = 0, \\
m_2 \psi_n'(y) - a_n m_2 \xi_n'(y) - g_n \psi_n'(m_2 y) + w_n \chi_n'(m_2 y) = 0, \\
m_2 b_n \xi_n(y) - m_2 \psi_n(y) + f_n \psi_n(m_2 y) - v_n \chi_n(m_2 y) = 0, \\
\psi_n(y) - a_n \xi_n(y) - g_n \psi_n(m_2 y) + w_n \chi_n(m_2 y) = 0, \\
b_n \xi_n'(y) - \psi_n'(y) + f_n \psi_n'(m_2 y) - v_n \chi_n'(m_2 y) = 0.
\end{aligned} \tag{E.7}$$

Here, m_1 and m_2 are ratios of the refractive indices of the core and shell relative to the background medium, respectively. The dimensionless quantities x and y are set to be kR_c and kR_s, respectively. $\psi_n(x), \xi_n(x)$, and $\chi_n(x)$ are the Riccati-Bessel functions. Here, the usage is so as to keep the notations to be the same as those used in Ref. [37]. By solving these eight equations, the set of coefficients can be obtained. For example, a_n and b_n are given by

$$\begin{aligned}
a_n &= \frac{\psi_n(y)[\psi_n'(m_2 y) - A_n \chi_n'(m_2 y)] - m_2 \psi_n'(y)[\psi_n(m_2 y) - A_n \chi_n(m_2 y)]}{\xi_n(y)[\psi_n'(m_2 y) - A_n \chi_n'(m_2 y)] - m_2 \xi_n'(y)[\psi_n(m_2 y) - A_n \chi_n(m_2 y)]}, \\
b_n &= \frac{m_2 \psi_n(y)[\psi_n'(m_2 y) - B_n \chi_n'(m_2 y)] - \psi_n'(y)[\psi_n(m_2 y) - B_n \chi_n(m_2 y)]}{m_2 \xi_n(y)[\psi_n'(m_2 y) - B_n \chi_n'(m_2 y)] - \xi_n'(y)[\psi_n(m_2 y) - B_n \chi_n(m_2 y)]},
\end{aligned} \tag{E.8}$$

where A_n and B_n are

$$\begin{aligned}
A_n &= \frac{m_2 \psi_n(m_2 x) \psi_n'(m_1 x) - m_1 \psi_n'(m_2 x) \psi_n(m_1 x)}{m_2 \chi_n(m_2 x) \psi_n'(m_1 x) - m_1 \chi_n'(m_2 x) \psi_n(m_1 x)}, \\
B_n &= \frac{m_1 \psi_n(m_2 x) \psi_n'(m_1 x) - m_2 \psi_n'(m_2 x) \psi_n(m_1 x)}{m_1 \chi_n(m_2 x) \psi_n'(m_1 x) - m_2 \chi_n'(m_2 x) \psi_n(m_1 x)}.
\end{aligned} \tag{E.9}$$

Similar expressions for other coefficients are also obtained as follows:

$$c_n = m_1 m_2[\psi_n(m_2x)\chi_n'(m_2x) - \chi_n(m_2x)\psi_n'(m_2x)][\xi_n(y)\psi_n'(y) - \psi_n(y)\xi_n'(y)]/$$
$$\{[m_2\xi_n(y)\chi_n'(m_2y) - \chi_n(m_2y)\xi_n'(y)][m_1\psi_n(m_2x)\psi_n'(m_1x) - m_2\psi_n(x_1)\psi_n'(m_2x)]$$
$$+ [m_2\xi_n(y)\psi_n'(m_2y) - \psi_n(m_2y)\xi_n'(y)][m_2\psi_n(m_1x)\chi_n'(m_2x) - m_1\chi_n(m_2x)\psi_n'(m_1x)]\}, \tag{E.10}$$

$$d_n = m_1 m_2[\psi_n(m_2x)\chi_n'(m_2x) - \chi_n(m_2x)\psi_n'(m_2x)][\xi_n(y)\psi_n'(y) - \psi_n(y)\xi_n'(y)]/$$
$$\{[\xi_n(y)\chi_n'(m_2y) - m_2\chi_n(m_2y)\xi_n'(y)][m_2\psi_n(m_2x)\psi_n'(m_1x) - m_1\psi_n(x_1)\psi_n'(m_2x)]$$
$$+ [\xi_n(y)\psi_n'(m_2y) - m_2\psi_n(m_2y)\xi_n'(y)][m_1\psi_n(m_1x)\chi_n'(m_2x) - m_2\chi_n(m_2x)\psi_n'(m_1x)]\}, \tag{E.11}$$

$$f_n = m_2[m_2\psi_n(m_1x)\chi_n'(m_2x) - m_1\chi_n(m_2x)\psi_n'(m_1x)][\xi_n(y)\psi_n'(y) - \psi_n(y)\xi_n'(y)]/$$
$$\{[m_2\xi_n(y)\chi_n'(m_2y) - \chi_n(m_2y)\xi_n'(y)][m_1\psi_n(m_2x)\psi_n'(m_1x) - m_2\psi_n(x_1)\psi_n'(m_2x)]$$
$$+ [m_2\xi_n(y)\psi_n'(m_2y) - \psi_n(m_2y)\xi_n'(y)][m_2\psi_n(m_1x)\chi_n'(m_2x) - m_1\chi_n(m_2x)\psi_n'(m_1x)]\}, \tag{E.12}$$

$$g_n = m_2[m_1\psi_n(m_1x)\chi_n'(m_2x) - m_2\chi_n(m_2x)\psi_n'(m_1x)][\xi_n(y)\psi_n'(y) - \psi_n(y)\xi_n'(y)]/$$
$$\{[\xi_n(y)\chi_n'(m_2y) - m_2\chi_n(m_2y)\xi_n'(y)][m_2\psi_n(m_2x)\psi_n'(m_1x) - m_1\psi_n(x_1)\psi_n'(m_2x)]$$
$$+ [\xi_n(y)\psi_n'(m_2y) - m_2\psi_n(m_2y)\xi_n'(y)][m_1\psi_n(m_1x)\chi_n'(m_2x) - m_2\chi_n(m_2x)\psi_n'(m_1x)]\}, \tag{E.13}$$

$$v_n = m_2[m_2\psi_n(m_1x)\psi_n'(m_2x) - m_1\psi_n(m_2x)\psi_n'(m_1x)][\xi_n(y)\psi_n'(y) - \psi_n(y)\xi_n'(y)]/$$
$$\{[m_2\xi_n(y)\chi_n'(m_2y) - \chi_n(m_2y)\xi_n'(y)][m_1\psi_n(m_2x)\psi_n'(m_1x) - m_2\psi_n(x_1)\psi_n'(m_2x)]$$
$$+ [m_2\xi_n(y)\psi_n'(m_2y) - \psi_n(m_2y)\xi_n'(y)][m_2\psi_n(m_1x)\chi_n'(m_2x) - m_1\chi_n(m_2x)\psi_n'(m_1x)]\}, \tag{E.14}$$

$$w_n = m_2[m_2\psi_n(m_2x)\psi_n'(m_1x) - m_1\psi_n(m_1x)\psi_n'(m_2x)][\xi_n(y)\psi_n'(y) - \psi_n(y)\xi_n'(y)]/$$
$$\{[\xi_n(y)\chi_n'(m_2y) - m_2\chi_n(m_2y)\xi_n'(y)][m_1\psi_n(m_1x)\psi_n'(m_2x) - m_2\psi_n(x_2)\psi_n'(m_1x)]$$
$$+ [\xi_n(y)\psi_n'(m_2y) - m_2\psi_n(m_2y)\xi_n'(y)][m_2\chi_n(m_2x)\psi_n'(m_1x) - m_1\psi_n(m_1x)\chi_n'(m_2x)]\}. \tag{E.15}$$